Diagnostics in VUV laser spectroscopy

by

Ping Huang

Thesis presented in partial fulfillment of the requirements
for the degree of

Master of Science

at the University of Stellenbosch

Supervisors:

Dr. E.G. Rohwer

Prof. H.M.von Bergmann

Dr. G.J. Arendse

April 2005

Declaration

I, the undersigned, hereby declare that the work contained in this thesis is my own original work and that I have not previously in its entirety or in part submitted it at any university for a degree.

_____

Signature

_____

Date

Abstract

A tunable vacuum ultra-violet (VUV) laser source was recently developed for VUV spectroscopy using state selective excitation and total fluorescence detection. The VUV laser source makes use of a four-wave mixing process to provide tunable VUV radiation for the electronic excitation of the molecules. The theory of four-wave mixing, with the emphasis on parameters that are important for our experimental set-up to generate efficient tunable VUV radiation is discussed. The experimental setup, and in particular the metal vapor heat-pipe, which provides Mg vapor as the non-linear medium, is described. New diagnostic equipment described in this work was added to the experimental setup. This equipment was characterized and utilized together with the existing setup. The additional diagnostic equipment introduced enabled us to measure the tunable VUV output of the source (using a VUV monochromator), making it possible to significantly improve the efficiency of the existing tunable VUV laser source.

The technique of Laser Induced Fluorescence (LIF) was used to study electronic excitations of the $^{12}C^{16}O$ molecule. The addition of the new diagnostics made it possible for the first time to simultaneously record the absorption spectra of the flow-cooled CO molecules, introduced into a vacuum chamber through a pulsed valve. This added facility may enable us to detect excitation to non-fluorescent states. This may prove invaluable in the search for electronic excitations of CO-Ar or CO-CO van der Waals molecules in future experiments that are planned, since these theoretically predicted states may be pre-dissociating.

Opsomming

’n Afstembare vakuum ultraviolet (VUV) laser bron is onlangs ontwikkel vir VUV spektroskopie deur middel van toestand-selektiewe opwekking en fluoressensie waarneming. Die VUV laser bron maak gebruik van ’n vier-golf vermengingsproses om afstembare VUV straling te voorsien vir die elektroniese opwekking van molekules. Die teorie van vier-golf vermenging word bespreek, met die klem op die eksperimentele parameters wat belangrik is vir die generering van afstembare VUV straling. Die eksperimentele opstelling, in die besonder die metaal damp hittepyp, wat die nie-liniêre medium voorsien, word beskryf. Nuwe diagnostiese toerusting is tot die bestaande eksperimentele opstelling gevoeg. Hierdie toerusting wat beskryf word in hierdie werk, is gekarakteriseer en is gebruik tesame met die bestaande opstelling. Hierdie nuwe diagnostiese toerusting het dit moontlik gemaak om die afstembare VUV uitset van die bron te meet. Daar is van ’n VUV monochromator gebruik gemaak, en sodoende kon die effektiwiteit van die bestaande afstembare VUV laser bron beduidend verbeter word.

Die Laser Geïnduseerde Fluoressensie (LGF) tegniek is gebruik om elektroniese opwekkings van die $^{12}C^{16}O$ molekule te bestudeer. Die toevoeging van die nuwe diagnostiek het dit vir die eerste keer moontlik gemaak om gelyktydig die absorpsiespektrum van die vloei-verkoelde CO molekules, wat deur in gepulseerde klep in die vakuumkamer ingelaat is, waar te neem. Hierdie addisionele fasiliteit sou dit kon moontlik maak om nie-fluoresserende toestande waar te neem. Dit mag baie waardevol wees in die soektog na elektroniese opwekkings van CO-Ar of CO-CO van der Waals molekules in toekomstige eksperimente wat beplan word, want hierdie teoreties voorspelde toestande kan pre-dissosiëer.

Contents

Chapter 1

Introduction

1.1 Overview

Tunable lasers have been successfully used in spectroscopy of atoms and molecules in the visible and infrared regions. In the ultra-violet (UV) and vacuum ultra-violet (VUV) no tunable lasers that are useful for high resolution spectroscopy exit. A coherent beam of light can be generated by sum and difference frequency generation by passing laser beams through a suitable non-linear medium. Non-linear processes occur in media in which the electric field of the electromagnetic wave is large enough to drive the dipole oscillation into the non-linear regime. In the infrared and visible regions, this technology has been used successfully. Second order non-linear processes in non-linear crystals are usually used to extend the tuning region of lasers into infrared and visible regions. However, gaseous media have to be used to produce VUV radiation by four-wave frequency mixing because crystals generally strongly absorb the generated wavelengths of interest in the VUV. Four-wave mixing is a third order non-linear process. As a third order non-linear optical process, four-wave mixing means four electromagnetic waves interact with a non-linear optical medium to transfer energy among the electromagnetic fields of different frequencies. Sum-frequency generation mentioned in this thesis refers to the process where two laser beams with frequencies ω_1 and ω_2 interact with a gaseous non-linear medium, generating a coherent beam at the sum-frequency $\omega_s = \omega_1 + \omega_1 + \omega_2$. In the degenerate case of $\omega_1 = \omega_2 = \omega$

it is called third-harmonic generation and $\omega_s = 3\omega$.

The theory of four-wave mixing, and in particular in a gaseous medium, is discussed in chapter 2, with the emphasis on parameters that are important for our experimental setup to efficiently generate tunable VUV radiation. It has been reported that the conversion efficiency of harmonic generation in a two component gaseous medium could be increased by several orders of magnitude [8] by using a metal vapor produced in a heat-pipe oven [9] for its high non-linear susceptibility, and adding a noble gas to provide the appropriate overall refractive index for phase-matching. The principle of phase-matching is also discussed in detail, with reference to our specific setup. In the literature [12], [22], and [15] it has been reported that the conversion efficiency can be raised by making use of two-photon resonant enhancement of the non-linear susceptibility.

The non-linear medium used in our experimental setup is a metal vapor in a heat-pipe. The heat-pipe is discussed in chapter 3, and the output of the VUV source is presented in chapter 4. For the experiments done in the VUV it is firstly important to be able to measure the VUV output of the source. The detection of VUV radiation is not trivial, and separation of VUV wavelengths can only be achieved using a VUV monochromator. Therefore in chapter 2 the theory of the monochromators and the gratings used are discussed, and in chapter 3 the design of the optical setup for connecting the monochromator to our irradiation chamber is discussed. In chapter 4 the monochromators used are characterized.

The main application of our VUV source is laser spectroscopy of molecules, and in particular electronic excitations of molecules. In chapter 2 the theory of electronic excitations in molecules will be briefly presented. In chapter 3 the layout of the irradiation chamber, where the super-cooled molecules are introduced into a vacuum chamber through a pulsed valve, is discussed. In this thesis the technique of Laser Induced Fluorescence (LIF) was used to study the $^{12}C^{16}O$ molecule. LIF is essentially the detection of total fluorescence upon excitation with the tunable VUV generated by four-wave mixing. In addition absorption spectra could be recorded with the monochromator added to the existing setup. In chapter 5 the results of the experiments in VUV laser spectroscopy of CO molecule are discussed.

1.2 Aim

A tunable vacuum ultra-violet (VUV) laser source was recently developed for VUV spectroscopy. Initial experiments done at the Laser Research Institute (LRI) have concentrated on state selective VUV excitation of molecules followed by recording of the total laser induced fluorescence (LIF). The VUV laser source makes use of a four-wave mixing process to provide tunable VUV radiation for the excitation of the molecules. The total fluorescence is collected using a solar blind photo-multiplier at right angles to the VUV laser beam.

The aim of this project was to expand the capability of this existing LIF detection system. The aim was twofold: to improve the yield and quality of the tunable VUV laser source; and to improve the methods of detecting selective excitation. The vacuum ultra-violet monochromator was characterized and then utilized for the following investigations. Firstly VUV laser output generated by a four-wave frequency mixing process in a magnesium vapor heat-pipe was characterized, and in doing so it was possible to improve the quality of the output of the source. Secondly the VUV absorption spectrum of the molecules in a supersonic expansion was recorded simultaneously with the total fluorescence measurement, in order to detect excitation to non-fluorescent states. Thirdly the setup was used to evaluate the possibility of detecting wavelength dependent fluorescence.

Chapter 2

Theory

In this chapter the theory relevant to the experimental work is discussed. This focuses on the generation of the VUV through a non-linear process, basic theory of molecular levels and transitions required to understand the spectra generated, and some basic theory on diffraction gratings and monochromators.

2.1 Four-wave mixing

2.1.1 Introduction

Four-wave mixing in gaseous media is a preferred method to generate narrow bandwidth coherent VUV radiation because most non-linear crystals are opaque at wavelength below 200 nm.

The basic principle of third-harmonic generation as an example of a frequency upconversion process in a gaseous non-linear medium will been described here. Non-linear susceptibilities $\chi^{(i)}$ are used to describe all the properties of a given non-linear medium. Non-linear susceptibilities indicate the effect of resonance enhancement and angular momentum selection rules. In the small signal limit, the dominant $\chi^{(3)}$ gives rise to the generation of the third-harmonic wave. The derived expression for conversion efficiency shows medium parameters and beam parameters.

2.1.2 Polarization

An electromagnetic wave, traveling through a medium generally gives rise to non-linear polarization of the medium. The total polarization of the medium due to monochromatic light, plane polarized in the x direction, is given by:

$$\overrightarrow{P_x} = \left(\chi^{(1)}E_x + \chi^{(2)}E_x^2 + \chi^{(3)}E_x^3 + \cdots + \chi^{(n)}E_x^n\right)\widehat{\varepsilon}_x \tag{2.1}$$

- $\chi^{(i)}$ is the electrical susceptibility of the $i-th$ order
- E_x is the local electric field
- $\widehat{\varepsilon}_x$ is the unit vector in the x direction.

This equation indicates that the contributions to polarization can be divided into two parts: linear polarization $\overrightarrow{P}^L$ and non-linear polarization $\overrightarrow{P}^{NL}$. Equation 2.1 can therefore be written as:

$$\overrightarrow{P} = \overrightarrow{P}^L + \overrightarrow{P}^{NL} \tag{2.2}$$

where

$$\overrightarrow{P}^L = \chi^{(1)}E_x\widehat{\varepsilon}_x \tag{2.3}$$

and

$$\overrightarrow{P}^{NL} = \sum_{n=2}^{\infty} \overrightarrow{P}^{(n)} \tag{2.4}$$

with

$$\overrightarrow{P}^{(n)} = \chi^{(n)}E_x^n\widehat{\varepsilon}_x. \tag{2.5}$$

The electric field propagating through the medium can be expanded as a Fourier series:

$$\overrightarrow{E}(r,t) = \frac{1}{2}\sum_j \left[\widehat{\varepsilon}_j\widehat{E}(r,\omega_j)\,e^{-i(\omega_j t - k_j z)} + cc\right] = \frac{1}{2}\sum_j \left[\widehat{\varepsilon}_j E(r,\omega_j)\,e^{-i\omega_j t} + cc\right] \tag{2.6}$$

where $E(r,\omega_j) = \widehat{E}(r,\omega_j)\, e^{ik_j z}$ and $\widehat{\varepsilon}_j$ is the unit vector in the direction of the polarization of the field component at frequency ω_j. Here the "hat" on $\widehat{E}$ does not indicate a vector, it only serves to distinguish E from $\widehat{E}$.

A Fourier series expansion can also be made for each part of the polarization:

$$\overrightarrow{P}^{(n)}(r,t) = \frac{1}{2}\sum_{q} \widehat{\varepsilon}_q P^{(n)}(r,\omega_q)\, e^{-i\omega_q t} + cc \tag{2.7}$$

where $\overrightarrow{P}^{(n)}(r,\omega_q)$ is the $n-th$ order polarization density at the frequency ω_q. The expansion is valid for $n = 1$, (first order, linear polarization) and $n = 2, 3, \cdots$ (higher order non-linear polarization). Each of the Fourier coefficients $\overrightarrow{P}^{(n)}(r,\omega_q)$ of the polarization density can be expressed in terms of susceptibilities and Fourier coefficients of the electric fields as will be discussed and applied in the next two sections 2.1.2.1 and 2.1.2.2.

2.1.2.1 Linear polarization

The complete quantum mechanical expression for the linear polarization is given by [4]:

$$\overrightarrow{P}^{(1)}_{\alpha_1}(r,\omega_q) = \overrightarrow{P}^{L}_{\alpha_1}(r,\omega_q) = N\sum_{\alpha_1} \chi^{(1)}_{\alpha_s\alpha_1}(-\omega_q;\omega_q)\, \overrightarrow{E}_{\alpha_1}(r,\omega_q) \tag{2.8}$$

where N is the number density of atoms or molecules in the medium. $\overrightarrow{P}_{\alpha_1}$ and $\overrightarrow{E}_{\alpha_1}$ are the α_1 components of the Fourier coefficients of the polarization density and the electric field, α_1 characterizes the polarization direction of the component of the incident wave.

Cartesian coordinates can be chosen to specify the polarization direction for linear susceptibility. It can be shown [4] that $\chi^{(1)}_{\alpha_s\alpha_1}(-\omega;\omega)$ has elements: $\chi^{(1)}_{xx}(-\omega;\omega)$, $\chi^{(1)}_{xy}(-\omega;\omega)$, $\cdots$, $\chi^{(1)}_{zy}(-\omega;\omega)$, $\chi^{(1)}_{zz}(-\omega;\omega)$. For example, the x-component of the polarization density is given by:

$$\overrightarrow{P}^{(1)}_{x}(r,\omega) = N\chi^{(1)}_{xx}(-\omega;\omega)\, \overrightarrow{E}_{x}(r,\omega) + N\chi^{(1)}_{xy}(-\omega;\omega)\, \overrightarrow{E}_{y}(r,\omega) + N\chi^{(1)}_{xz}(-\omega;\omega)\, \overrightarrow{E}_{z}(r,\omega) \tag{2.9}$$

with $\overrightarrow{E}_{z}(r,\omega) = 0$ if z is the direction of propagation. Similar expressions can be written for $\overrightarrow{P}^{(1)}_{y}(r,\omega)$ and $\overrightarrow{P}^{(1)}_{z}(r,\omega)$.

Gaseous media, that are relevant in this discussion, are isotropic. In an isotropic medium, the linear susceptibility $\chi^{(1)}_{\alpha_s\alpha_1}$only has the $\chi^{(1)}_{xx}$, $\chi^{(1)}_{yy}$, $\chi^{(1)}_{zz}$components and the expression for a component of the polarization $\overrightarrow{P}^{(1)}_{\alpha}(r,\omega)$ as given by equation 2.9, reduces to only one term, depending only on the α component of the electrical field, namely

$$\overrightarrow{P}^{(1)}_{\alpha}(r,\omega) = N\chi^{(1)}_{\alpha\alpha}(-\omega;\omega)\,\overrightarrow{E}_{\alpha}(r,\omega) \tag{2.10}$$

or simply:

$$\overrightarrow{P}^{(1)} = \overrightarrow{P}^{L} = N\chi^{(1)}\overrightarrow{E} \tag{2.11}$$

where N is the number density of atoms or molecules, and the proportionality constant $\chi^{(1)}$ is the complex linear susceptibility [33]:

$$\chi^{(1)} = \overline{\chi}^{(1)} + i\widetilde{\chi}^{(1)} = \frac{1}{\hbar}\sum_{a}\frac{\left|\mu_{ag}\right|^2}{(\Omega_{ag}-\omega)} \tag{2.12}$$

- μ_{ag} is the dipole matrix element for the transition between state $\mid g\rangle$ and state $\mid a\rangle$
- $\Omega_{ag} = \omega_{ag} - i\Gamma_{ag}$

  where ω_{ag} is the transition frequency and Γ_{ag} is the damping constant.
- $\overline{\chi}^{(1)}$ defines the refractive index, n, and is given by [33]:

$$1 + 4\pi N\overline{\chi}^{(1)} = \varepsilon_r = n^2 \tag{2.13}$$

- $\widetilde{\chi}^{(1)}$ defines the absorption coefficient, κ, according to

$$4\pi N\widetilde{\chi}^{(1)} = \varepsilon_i = \frac{cn\kappa}{\omega} = \frac{cnN\sigma}{\omega} \tag{2.14}$$

with absorption cross section σ. These are the well known relations for the absorption coefficient and the refractive index in linear optics.

2.1.2.2 Non-linear polarization

For larger electric fields the non-linear polarization can not be ignored. The non-linear polarization is responsible for non-linear optical processes.

The quantum mechanical definition of the $n-th$ order terms of $\overrightarrow{P}^{(n)}$ is given by [25]:

$$\overrightarrow{P}_{\alpha_s}^{(n)}(r,\omega_s) = \frac{n!N}{2^{n-1}} \sum_{\alpha_1 \cdots \alpha_n} \chi^{(n)}_{\alpha_s \alpha_1 \cdots \alpha_n}(-\omega_s;\omega_1 \cdots \omega_n) \times \overrightarrow{E}_{\alpha_1}(r,\omega_1) \cdots \overrightarrow{E}_{\alpha_n}(r,\omega_n). \quad (2.15)$$

Where N is the number density of atoms or molecules in the medium. 2^{n-1} originates from the factor $\frac{1}{2}$ in equation 2.6 and equation 2.7. $n!$ accounts for the intrinsic permutation symmetry of the non-linear susceptibilities if all frequencies $\omega_1 \cdots \omega_n$ are nonzero and different. $\chi^{(n)}_{\alpha_s \alpha_1 \cdots \alpha_n}$ is the electrical susceptibility matching the total polarization density $\overrightarrow{P}^{(n)}_{\alpha_s}$ at frequency $\omega_s = \omega_1 + \omega_2 + \cdots + \omega_n$ to n electric fields of frequencies $\omega_1 \cdots \omega_n$. $\overrightarrow{P}_{\alpha_p}$ and $\overrightarrow{E}_{\alpha_p}$ are the Fourier coefficients of the α_p component of the polarization density and electrical field, respectively. The α_p presents the "polarization direction" of the $p-$th wave. The indices $\alpha_{1\ldots}\alpha_n$ are, for plane polarized waves, Cartesian subscripts (x, y, and z) all of which are responsible for the full polarization density in the Cartesian direction α_s.

For the third order, for example, the non-linear susceptibility $\overrightarrow{P}^{(3)}_{\alpha_s}$ can be expressed as:

$$\overrightarrow{P}^{(3)}_{\alpha_s}(r,\omega_s) = \frac{3N}{2} \sum_{\alpha_1=x,y,z} \sum_{\alpha_2=x,y,z} \sum_{\alpha_3=x,y,z} \chi^{(3)}_{\alpha_s \alpha_1 \alpha_2 \alpha_3}(-\omega_s;\omega_1,\omega_2,\omega_3)\, \overrightarrow{E}_{\alpha_1}(r,\omega_1)\, \overrightarrow{E}_{\alpha_2}(r,\omega_2)\, \overrightarrow{E}_{\alpha_3}(r,\omega_3) \quad (2.16)$$

with $\omega_s = \omega_1 + \omega_2 + \omega_3$.

When the general expression is applied to the third-harmonic generation in an isotropic atomic vapor, the same simplifications can be made as above in equation 2.11. Assuming that the incident wave is plane polarized in the y-direction; $\overrightarrow{E}_y(r,\omega)$ is the only non-zero component of the electric field. The expression for the third order non-linear polarization density is then reduced to only one component:

$$\overrightarrow{P}_y^{(3)}(r,\omega_s) = \frac{3N}{2}\chi_{yyy}^{(3)}(-\omega_s;\omega_1,\omega_2,\omega_3)\,\overrightarrow{E}_y(r,\omega_1)\,\overrightarrow{E}_y(r,\omega_2)\,\overrightarrow{E}_y(r,\omega_3). \tag{2.17}$$

(with $\omega_1 = \omega_2 = \omega_3 = \omega$ and $\omega_s = 3\omega$ for third-harmonic).

2.1.3 The fundamental equation of non-linear optics

In a charge-free, current-free, nonmagnetic gaseous medium, the Maxwell equations can be reduced to the Maxwell wave equation [17] (page 65 equation 3.23):

$$\Delta\overrightarrow{E} - \frac{1}{c^2}\frac{\partial^2\overrightarrow{E}}{\partial t^2} = \frac{4\pi}{c^2}\frac{\partial^2\overrightarrow{P}}{\partial t^2} \tag{2.18}$$

where

$$\overrightarrow{P} = \overrightarrow{P}^{(L)} + \overrightarrow{P}^{(NL)} = \overrightarrow{P}^{(L)} + \sum_{n=2}^{\infty}\overrightarrow{P}^{(n)}. \tag{2.19}$$

For a general discussion, it can be assumed, that the electric field propagating through the medium is a continuous plane wave. The results of this plane wave approximation are useful to describe laser beams that are not tightly focused. In this approximation the electric field and polarization density can be written as Fourier expansions:

$$\overrightarrow{E}(z,t) = \frac{1}{2}\sum_q \widehat{\varepsilon}_q\widehat{E}(z,\omega_q)\,e^{(ik_qr - i\omega_q t)} + cc = \frac{1}{2}\sum_q \widehat{\varepsilon}_q E(z,\omega_q)\,e^{(-i\omega_q t)} + cc \tag{2.20}$$

with

$$E(z,\omega_q) = \widehat{E}(z,\omega_q)\,e^{ik_qr} \tag{2.21}$$

and

$$\overrightarrow{P}^{(n)}(z,t) = \frac{1}{2}\sum_q \left[\widehat{\varepsilon}_j P_j^{(n)}(z,\omega_q)\,e^{-i\omega_q t} + cc\right]. \tag{2.22}$$

We assume that the amplitudes of the electric field, $\overrightarrow{E}_q$, and of the polarization, $\overrightarrow{P}_q^{(n)}$, vary slowly in space and time. Under these conditions the Maxwell equations reduce to the

fundamental equation of non-linear optics [27].

$$\frac{d\widehat{E}_q}{dz} = i\frac{2\pi\omega_q^2}{c^2 k_q}\overrightarrow{P}_q^{NL}\exp\left(-ik_q z\right) - \frac{\sigma^{(1)}\left(\omega_q\right)}{2}N\widehat{E}_q = i\frac{2\pi\omega_q^2}{c^2 k_q}\sum_{n=2}^{\infty}\overrightarrow{P}_q^{(n)}\exp\left(-ik_q z\right) - \frac{\sigma^{(1)}\left(\omega_q\right)}{2}N\widehat{E}_q. \tag{2.23}$$

Here $\widehat{E}_q$ and $\overrightarrow{P}_q^{(n)}$ are the Fourier components of the electrical field and polarization at the frequency ω_q as defined in equation 2.20, and k_q is the wave vector of the wave with frequency ω_q, and it is related to the refractive index n_q by the relation:

$$k_q = \frac{\omega_q n_q}{c}. \tag{2.24}$$

Equation 2.23 includes also one-photon absorption processes as defined by the absorption cross section: $\sigma^{(1)}\left(\omega_q\right) = \frac{k_q}{N}$ at the frequency ω_q.

In an isotropic medium, only the uneven order (1, 3, 5 $\cdots$) susceptibilities are non-zero in equation 2.23, because the non-linear polarization has to be unaffected upon a reflection of the coordinate system at its origin ([32], page 296). If the uneven order terms are kept up to the 3^{rd} order in the expansion of equation 2.23 [36], [24], a four-wave mixing process can be described where the frequency of the resulting waves ω_q are given by all possible non-negative combinations of the form $\omega_s = \pm\omega_1 \pm \omega_2 \pm \omega_3$. As a typical case, figure 2-1 illustrates the frequency mixing with $\omega_s = 2\omega_1 + \omega_2$. For simplicity third-harmonic generation is chosen for the further discussion, where $\omega_1 = \omega_2 = \omega_3 = \omega$ and $\omega_s = 3\omega$. In this case equation 2.23 represents a set of two coupled equations with $\omega_q = \omega$ and $\omega_q = 3\omega$, respectively. The solutions of these two equations will be discussed and will be given in the equation 2.45, 2.47 later. In this case the non-linear polarization at frequencies ω_1 and ω_3 can be written as [28]:

$$\overrightarrow{P}_1^{NL}\left(\omega\right) = \frac{N}{4}\left[3\chi_T^{(3)}\left(\omega\right)\overrightarrow{E}_3\overrightarrow{E}_1^{*}\overrightarrow{E}_1^{*} + \chi_S^{(3)}\left(\omega\right)\overrightarrow{E}_1\left|\overrightarrow{E}_1\right|^2 + \chi_S^{(3)}\left(\omega, 3\omega\right)\overrightarrow{E}_1\left|\overrightarrow{E}_3\right|^2\right] \tag{2.25}$$

$$\overrightarrow{P}_3^{NL}\left(\omega\right) = \frac{N}{4}\left[\chi_T^{(3)}\left(3\omega\right)\overrightarrow{E}_1^3 + \chi_S^{(3)}\left(3\omega\right)\overrightarrow{E}_3\left|\overrightarrow{E}_3\right|^2 + \chi_S^{(3)}\left(3\omega, \omega\right)\overrightarrow{E}_3\left|\overrightarrow{E}_1\right|^2\right]. \tag{2.26}$$

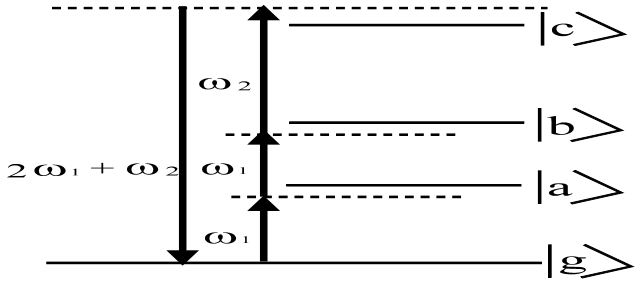

Figure 2-1: Schematic diagram of sum frequency mixing in a nonresonant nonlinear medium. Solid line and dashed line present real and imaginary energy levels respectively. Real energy levels are labelled $\mid a\rangle$, $\mid b\rangle$, $\mid c\rangle$, and $\mid g\rangle$.

Alternative shorter labels for the susceptibilities ([33], [4]) have been used above:

$\chi_T^{(3)}(3\omega) = \chi_T^{(3)}(-3\omega;\omega,\omega,\omega)$; $\chi_T^{(3)}(\omega) = \chi_T^{(3)}(-\omega;-\omega,-\omega,3\omega)$

$\chi_S^{(3)}(\omega) = \chi_S^{(3)}(-\omega;-\omega,\omega,\omega)$; $\chi_S^{(3)}(3\omega) = \chi_S^{(3)}(-3\omega;-3\omega,3\omega,3\omega)$

$\chi_S^{(3)}(\omega,3\omega) = \chi_S^{(3)}(-\omega;\omega,-3\omega,3\omega)$; $\chi_S^{(3)}(3\omega,\omega) = \chi_S^{(3)}(-3\omega;\omega,-\omega,3\omega)$.

It is clear that these listed susceptibilities include all possible four-wave frequencies mixing processes that can take place in the case of a single incident beam, generating radiation fields at frequencies ω and 3ω.

The physical interpretation of the different terms in equations 2.25 and 2.26 according to references [33], [27] is:

- The term $\chi_T^{(3)}(3\omega)$ in equation 2.26 represents the process of third-harmonic generation, as illustrated in figure 2-2 (a). The term $\chi_T^{(3)}(\omega)$ in equation 2.25 describes the inverse process by which some of third-harmonic radiation is transferred back to the fundamental wave.

- The term $\chi_S^{(3)}(\omega)$ in equation 2.25 and the term $\chi_S^{(3)}(3\omega)$ in equation 2.26 represent an intensity-dependent change of the linear susceptibility at the frequency ω and 3ω,

respectively. The real parts represent intensity dependent changes of the refractive index; and the imaginary parts are responsible for the two-photon absorption of the fundamental and the harmonic wave, as illustrated in figure 2-2 (b).

- The real parts of the term $\chi_S^{(3)}(\omega, 3\omega)$ and $\chi_S^{(3)}(3\omega, \omega)$ describe the change of the refractive index at the fundamental (harmonic) frequency due to the harmonic (fundamental) intensity; and the imaginary parts give rise to Raman-type gain or losses [27], as illustrated in figure 2-2 (c).

In order to explain the relevant material parameter ($\chi^{(3)}$) of four-wave mixing, it suffices to present only the result for the simplest possible case of the third-harmonic generation where the three incident waves are identical (degenerate four-wave mixing). The non-linear susceptibilities appearing in equations 2.26 and 2.25 have to be discussed. For the limiting case of third-harmonic generation, the dominant contributions to the third-order non-linear susceptibilities in equations 2.25 and 2.26 are given by the following expressions [27]:

$$\chi_T^{(3)}(3\omega) = \hbar^{-3} \sum_{a,b,c} \frac{\mu_{ga}\mu_{ab}\mu_{bc}\mu_{cg}}{(\omega_{ga} - \omega)(\omega_{gb} - 2\omega)(\omega_{gc} - 3\omega)} \tag{2.27}$$

$$\chi_S^{(3)}(\omega) = \chi_{SA}^{(3)}(\omega) = \hbar^{-3} \sum_{a,b,c} \frac{\mu_{ga}\mu_{ab}\mu_{bc}\mu_{cg}}{(\omega_{ga} - \omega)(\omega_{gb} - 2\omega)(\omega_{gc} - \omega)} \tag{2.28}$$

$$\chi_S^{(3)}(3\omega, \omega) = \chi_{SB}^{(3)}(3\omega, \omega) = \hbar^{-3} \sum_{a,b,c} \frac{\mu_{ga}\mu_{ab}\mu_{bc}\mu_{cg}}{(\omega_{ga} - 3\omega)(\omega_{gb} - 2\omega)(\omega_{gc} - 3\omega)} \tag{2.29}$$

and illustrated (for the two-photon resonant case) in figure 2-2. μ_{ab} is the dipole matrix element for the transition between two states $\mid a\rangle \rightarrow \mid b\rangle$. ω_{ab} is the complex transition frequency given by the equation $\omega_{ab} = \Omega_{ab} + i\Gamma_{ab}$ where Γ_{ab} is the damping constant (absorption linewidth) and Ω_{ab} is the frequency difference between the unperturbed states.

All third-order non-linear susceptibilities in equations 2.27, 2.28, and 2.29 are given by a sum over intermediate states $\mid a\rangle$, $\mid b\rangle$, and $\mid c\rangle$. The sum over the ground state $\mid g\rangle$ is neglected in an atomic gas medium because in the unperturbed atomic gas the excited atomic states have very small populations compared to the lowest energy ground state.

These three equations have the following significance:

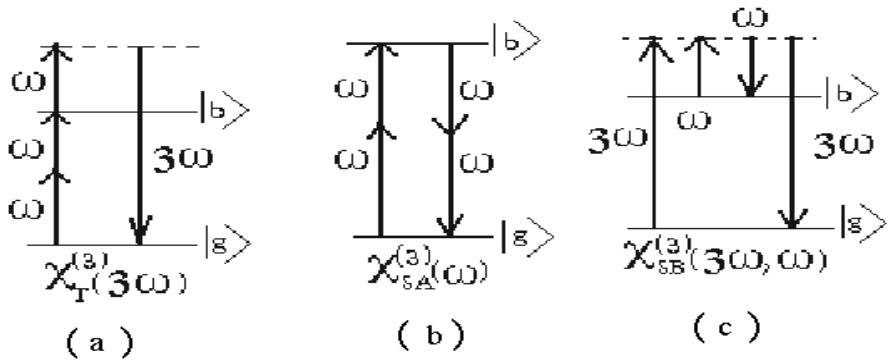

Figure 2-2: Schematic representation of the three dominant nonlinear susceptibilities as associated with third harmonic generation, illustrated for the two-photon resonant case: (a) the susceptibility responsible for third harmonic generation, (b) the susceptibility responsible for two-photon absorption and contributing significantly to intensity dependent changes of the indices of refraction, and (c) the susceptibility responsible for Raman-type losses.

- Three resonant terms in the denominator help us to understand resonance enhancement: If either $\omega = \omega_{ag}$ (one-photon resonance), or $2\omega = \omega_{bg}$ (two-photon resonance), or $3\omega = \omega_{cg}$ (three-photon resonance) the imaginary energy level is very close to the real energy level as shown in the figure 2-1. The denominators of the equations 2.27, 2.28, and 2.29 then become infinitely small, and the value of the susceptibility is thus enhanced.

- The four dipole matrix elements μ in the numerator illustrate the way that angular momentum selection rules govern the behavior of the susceptibility. This is discussed further in section 2.1.4.

2.1.4 Resonance enhancement of the non-linear susceptibility

The susceptibility $\chi_T^{(3)}(3\omega)$ can clearly be optimized by choosing an appropriate fundamental frequency that minimizes one of the difference factors in the denominator of equation 2.27. The three possibilities for resonance are illustrated in figure 2-3. According to the electric dipole selection rules, $\chi_T^{(3)}(3\omega)$ will only be non-zero if the states $\mid g\rangle$ and $\mid b\rangle$ have the same parity

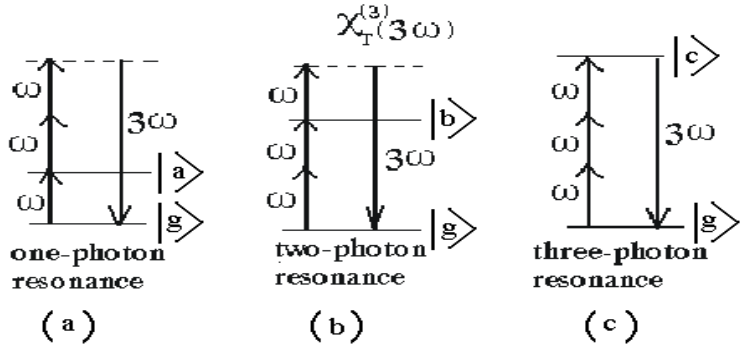

Figure 2-3: Schematic representation of the three possibilities for resonant enhancement of the third order susceptibilities responsible for the third harmonic generation (a) one-photon resonance, associated with one-photon absorption of the fundamental wave by the allowed dipole transition from the ground state $\mid g\rangle$ to $\mid a\rangle$, (b) two-photon resonance, and (c) three-photon resonance, associated with three-photon absorption of the third-harmonic wave by the allowed dipole transition from the ground state $\mid g\rangle$ to $\mid c\rangle$.

and the states $\mid a\rangle$ and $\mid c\rangle$ have opposite parity to $\mid g\rangle$. This means that the atoms can make a dipole transition from state $\mid g\rangle$ to state $\mid a\rangle$, and from state $\mid g\rangle$ to state $\mid c\rangle$, but they are forbidden to make a transition from state $\mid g\rangle$ to state $\mid b\rangle$.

As a result, a one-photon resonance, with $\omega = \omega_{ga}$, can lead to a strong absorption of the fundamental wave. Three-photon resonance, with $3\omega = \omega_{gc}$, where $\mid g\rangle \rightarrow \mid c\rangle$ is a suitable auto-ionizing transition [22], can lead to strong absorption of the third-harmonic wave. Both cases lead to a result where the achievable harmonic wave will be reduced considerably. However the two-photon resonance, with $2\omega = \omega_{gb}$, does not open up the possibility for one-photon absorption by an allowed transition and can be used to enhance the susceptibility for third-harmonic generation if the two-photon absorption due to $\chi^{(3)}_{SA}(\omega)$ is sufficiently small.

In the case of two-photon resonant conditions equation 2.27, 2.28, and 2.29 become

$$\chi^{(3)}_{TR}(3\omega) = \frac{\hbar^{-3}}{(\omega_{gb} - 2\omega)} \left[\sum_a \frac{\mu_{ga}\mu_{ab}}{(\omega_{ga} - \omega)}\right] \left[\sum_a \frac{\mu_{ga}\mu_{ab}}{(\omega_{gc} - 3\omega)}\right] \tag{2.30}$$

$$\chi_{SR}^{(3)}(3\omega) = \frac{\hbar^{-3}}{(\omega_{gb} - 2\omega)} \left[\sum_a \frac{\mu_{ga}\mu_{\alpha b}}{(\omega_{ga} - \omega)} \right]^2 \tag{2.31}$$

$$\chi_{SR}^{(3)}(3\omega, \omega) = \frac{\hbar^{-3}}{(\omega_{gb} - 2\omega)} \left[\sum_a \frac{\mu_{ga}\mu_{ab}}{(\omega_{ga} - 3\omega)} \right]^2 \tag{2.32}$$

where the two-photon resonant factor determines the real and imaginary parts according to [27]:

$$\frac{1}{\omega_{bg} - 2\omega} = \frac{(\Omega_{bg} - 2\omega) + i\Gamma_{bg}}{(\Omega_{bg} - 2\omega)^2 + \Gamma_{bg}^2}. \tag{2.33}$$

From these equations we can conclude that the two-photon resonant condition enhances both $\chi_T^{(3)}$responsible for third-harmonic generation and $\chi_S^{(3)}$responsible for the destruction of phase-matching (it will be discussed in section 2.1.6) in the same way because any change in either frequencies or the non-linear medium will always affect all other non-linear susceptibilities in equation 2.27, 2.28, and 2.29.

2.1.5 Selection rules

In this section it is discussed how angular momentum selection rules govern the behavior of the four dipole matrix elements μ in the numerator of expressions 2.27, 2.28 and 2.29, and therefore the behavior of the non-linear susceptibilities. By means of the Wigner Eckart theorem the individual matrix elements may be written as [31]:

$$\langle \alpha J_a m_a \mid \overrightarrow{\mu} \mid \beta J_b m_b \rangle = (-1)^{J_a - m_a} \begin{pmatrix} J_a & 1 & J_b \\ -m_a & \Delta m_j & m_b \end{pmatrix} \langle \alpha J_a \mid \overrightarrow{\mu} \mid \beta J_b \rangle \tag{2.34}$$

where J is the angular momentum, m is the magnetic quantum number, a and b represent different states, and $\langle \alpha\ J_a \mid \overrightarrow{\mu} \mid \beta\ J_b \rangle$ is the reduced matrix element characterizing the overall transition moment between all the m-degenerate states $\mid \alpha\ J_a \rangle$ and $\mid \beta\ J_b \rangle$. According to the conservation of angular momentum it implies different selection rules [31]. Firstly the triangle relation is implied, which means that three vectors $\overrightarrow{J}_a$, $\overrightarrow{J}_b$ and $\overrightarrow{1}$ must form a closed triangle

because they depend only on the geometry and orientation of the system to the z-axis. Secondly the m-selection rule, $-m_a + \Delta m_j + m_b = 0$, immediately yields the following four conditions for the different non-linear susceptibilities in equation 2.27, 2.28 and 2.29:

$$-m_g + \Delta m_s + m_a = 0 \tag{2.35}$$

$$-m_a + \Delta m_1 + m_b = 0 \tag{2.36}$$

$$-m_b + \Delta m_2 + m_c = 0 \tag{2.37}$$

$$-m_c + \Delta m_3 + m_g = 0. \tag{2.38}$$

When these equations are summed they yield the important result

$$\Delta m_s + \Delta m_1 + \Delta m_2 + \Delta m_3 = 0. \tag{2.39}$$

This result gives the explanation that using two circular polarized incident beams can generate optimized sum-frequency with suppressed third-harmonic generation[1]. The change in the magnetic quantum number induced by the radiation, Δm_j, is equal to $+1$ (-1) for right (left) circularly polarized radiation and equal to 0 for linearly polarized radiation. When the incident beam at frequency ω_1 is right-hand circularly polarized each photon carries an angular momentum $\Delta m_1 = +1$ and the incident beam at frequency ω_2 is left-hand circularly polarized having angular momentum $\Delta m_2 = -1$, then the sum-frequency $\omega_s = 2\omega_1 + \omega_2$ is allowed and will have an angular moment $\Delta m_s = -1$ (left-hand circularly polarized) to satisfy the selection rule. The third-harmonics of either of the incident waves however are not allowed by the selection rule because

$$\Delta m_s + \Delta m_j + \Delta m_j + \Delta m_j = \Delta m_s + (\pm 1 \pm 1 \pm 1) = \Delta m_s \pm 3 = 0 \tag{2.40}$$

[1]Under moderate incident intensities the conversion efficiency for third-harmonic generation relies on the two-photon resonance of the fundamental frequency which makes the effective tuning range small. Sum-freqency generation by partly degenerate four-wave frequency mixing using two incident beams with different frequencies overcomes this restriction. However, the generation of the third harmonics of the fundamental frequencies ω_1 and ω_2 competes strongly with the sum-frequency generation.

can not be satisfied. The single sum-frequency photon can not carry an angular momentum of magnitude 3.

2.1.6 Small signal limit

The number of non-linear polarizations that are required for a quantitative description of four-wave mixing in gases increases with growing electric field amplitudes. In this section the small signal limit is discussed.

In the small signal limit, the electric field amplitude of the third-harmonic wave is much smaller than the electric field amplitude of the fundamental wave, $\left|\overrightarrow{E}_3\right| \ll \left|\overrightarrow{E}_1\right|$. For an atomic medium, it can also be assumed that all atoms are and remain in the ground state and that the contributions of atoms in excited states are negligible. Therefore expression for the non-linear polarization intensity at the third-harmonic frequency 3ω, reduces to only one term:

$$\overrightarrow{P}_3^{NL} = \frac{N}{4}\chi_T^{(3)}\left(-3\omega;\omega,\omega,\omega\right)\overrightarrow{E}_1\overrightarrow{E}_1\overrightarrow{E}_1. \tag{2.41}$$

Substituting this result into the fundamental equation of non-linear optics equation 2.23, a differential equation describing the growth of the electric field $\widehat{E}_3(z)$ at frequency 3ω in terms of $\widehat{E}_1(z)$ is obtained:

$$\frac{d\widehat{E}_3(z)}{dz} = i\frac{2\pi(3\omega)^2}{c^2 k_{3\omega}}\frac{N}{4}\chi_T^{(3)}\widehat{E}_1^3 e^{-i\triangle kz} - \frac{\sigma^{(1)}(3\omega)}{2}N\widehat{E}_3 \tag{2.42}$$

with the k-vector mismatch

$$\triangle k = k_{3\omega} - 3k_{\omega}. \tag{2.43}$$

The differential equation 2.42 (for the change of $\overrightarrow{E}_1(\omega)$ with z) is simplified by assuming that the fundamental pump wave intensity is not reduced significantly by the third-harmonic generation or by two-photon absorption (small signal limit). This assumption reduces equation 2.4 to $\overrightarrow{P}_1^{NL} = 0$. Substituting this result into equation 2.23 a differential equation for $\widehat{E}_1(z)$ that takes only one-photon absorption of the fundamental wave into account is obtained

$$\frac{d\widehat{E}_1}{dz} = -\frac{N\sigma^{(1)}(\omega)}{2}\widehat{E}_1(z) \tag{2.44}$$

and has a very familiar solution

$$\widehat{E}_1(z) = \widehat{E}_1(0)\exp\left(-\frac{N\sigma^{(1)}(\omega)}{2}z\right). \tag{2.45}$$

The following uncoupled differential equation for the third-harmonic wavelength is obtained by substituting 2.45 into equation 2.42

$$\frac{d\widehat{E}_3(z)}{dz} = i\frac{\pi(3\omega)}{cn_3}\frac{N}{2}\chi_T^{(3)}(-3\omega;\omega,\omega,\omega)\left(\widehat{E}_1(0)\right)^3\exp\left[-\left(\frac{3N\sigma^{(1)}(\omega)}{2}+i\triangle k\right)z\right]-\frac{N\sigma^{(1)}(3\omega)}{2}\widehat{E}_3(z) \tag{2.46}$$

with $n_3 = \frac{k_3}{3\omega}c$ and $\triangle k = k_{3\omega} - 3k_\omega$.

We integrate the equation over the medium length L to get the expression for $\widehat{E}_3(L)$:

$$\widehat{E}_3(L) = i\frac{\pi 3\omega}{2cn_3}NL\chi_T^{(3)}(-3\omega;\omega,\omega,\omega)\left(\widehat{E}_1(0)\right)^3\frac{\exp(-\tau_s/2)}{\frac{\tau_s-\tau_i}{2}-i\triangle kL}\left(\exp\left(\frac{\tau_s-\tau_i}{2}-i\triangle kL\right)-1\right). \tag{2.47}$$

Here, we simplified the integration by assuming that the density of the medium has a rectangular density profile. A rectangular density profile, as illustrated in figure 2-4, can be expressed as the following function of the position z along the optical path

$$N(z) = N \text{ for } 0 < z < L, \tag{2.48}$$

$$N(z) = 0 \text{ for } L < z, z < 0 \tag{2.49}$$

where L is the medium length, and $N(z)$ the number density at position z. We also introduce the optical depth $\tau_s = \tau_3 = \kappa_3 L = \sigma^{(1)}(3\omega)NL$, for the third-harmonic wave. The total optical depth for the fundamental wave is

$$\tau_s = 3\tau_1 = 3\kappa_1 L = 3\sigma^{(1)}(3\omega)NL. \tag{2.50}$$

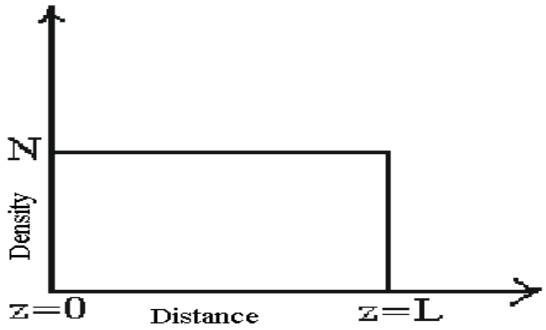

Figure 2-4: Diagram illustrating a rectangular density profile.

Since the electric field amplitude $\overrightarrow{E}_q$ is related to the intensity Φ_q according to [34]: $\Phi_q = \frac{n_q c}{8\pi}\left|\overrightarrow{E}_q\right|^2$, the following equation is obtained for the intensity conversion efficiency ([26], equation 13.65):

$$\frac{\Phi_3(L)}{\Phi_1(0)} = \frac{16\pi^4(3\omega)^2}{c^4 n_3 (n_1)^3}\left[NL\left|\chi_T^{(3)}(-3\omega;\omega,\omega,\omega)\right|\right]^2[\Phi_1(0)]^2 F(\triangle kL,\tau_i,\tau_s) \tag{2.51}$$

where

$$F(\triangle kL,\tau_i,\tau_s) = \frac{\exp(-\tau_i)+\exp(-\tau_s)-2\exp[-(\tau_i+\tau_s)/2]\cos(\triangle kL)}{[(\tau_i+\tau_s)/2]^2+(\triangle kL)^2} \tag{2.52}$$

which is called the phase-matching factor [30], [29]. Phase-matching is a critical macroscopic requirement which means the third-harmonic contributions generated in different volume elements of the active medium must interfere constructively. To discuss phase-matching further, some limiting cases regarding the phase-matching factor are illustrated here. For an optically thin medium (little absorption), where $\tau_s \to 0$, $\tau_i \to 0$ the phase-matching factor 2.52 reduces to

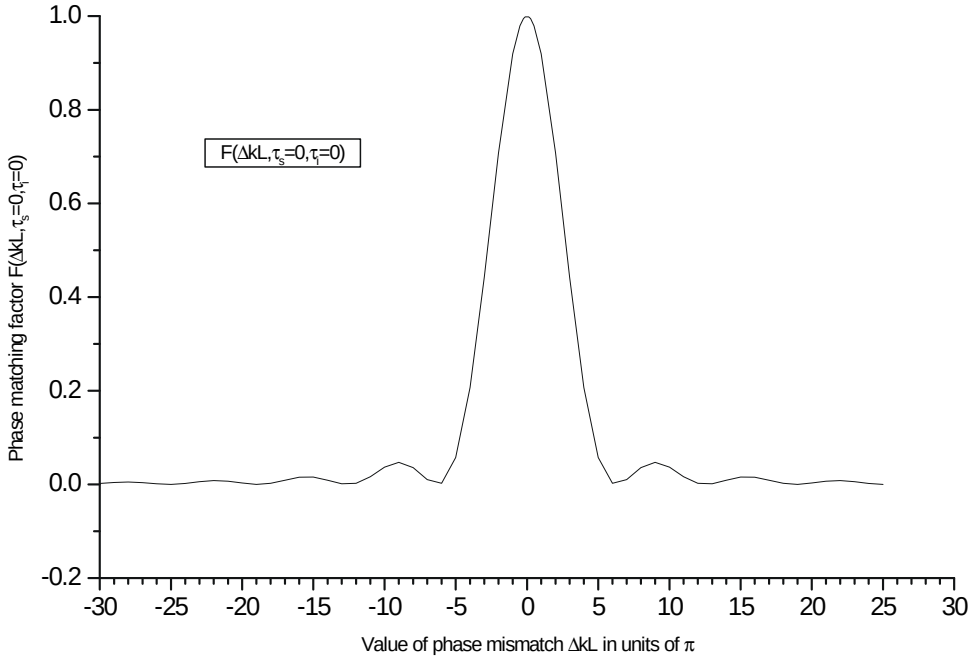

Figure 2-5: Theoretical phase-matching curve for an optically thin medium (linear scale on both axes).

$$F\left(\triangle kL, \tau_s \to 0, \tau_i \to 0\right) \approx \left(\frac{\sin\left(\triangle kL\right)}{\triangle kL}\right)^2. \tag{2.53}$$

This is the well-known $\left(\frac{\sin x}{x}\right)^2$ distribution of the third-harmonic intensity as a function of the phase mismatch $\triangle kL$ (see figure 2-5). Substituting equation 2.53 in equation 2.51, the intensity conversion efficiency for third-harmonic generation in the small signal limit e_{THG} is obtained:

$$e_{THG} = \frac{\Phi_3\left(L\right)}{\Phi_1\left(0\right)} = \frac{16\pi^4\left(3\omega\right)^2}{c^4 n_3\left(n_1\right)^3}\left[NL\left|\chi_T^{(3)}\left(-3\omega;\omega,\omega,\omega\right)\right|\right]^2\left[\Phi_1\left(0\right)\right]^2\left(\frac{\sin\left(\triangle kL\right)}{\triangle kL}\right)^2. \tag{2.54}$$

Equation 2.54 shows that the intensity of the fundamental wave is important for efficient third-harmonic generation because $\Phi_3\left(L\right)$ is proportional to $\left(\Phi_1\left(0\right)\right)^3$. Equation 2.54 also indicates that the efficiency depends on the phase-matching factor. From figure 2-5 it can be seen that the phase-matching factor is nonzero in only a small region for which proper phase-matching occurs. This clearly suggests that the output depends on phase-matching.

In practice we minimize τ_i, because it is relatively easy to choose a medium and fundamental frequency so that the fundamental frequency does not correspond to an electric dipole allowed transition. The absorption of the third-harmonic wave is often associated with auto-ionization and photon-ionization of the medium that can not be minimized. In this condition, τ_s might be large, but $\tau_i \ll 1$, giving

$$F\left(\triangle kL, \tau_i \ll 1, \tau_s\right) = \frac{1 + \exp\left(-\tau_s\right) - 2\exp\left[-\frac{\tau_s}{2}\right]\cos\left(\triangle kL\right)}{\left(\tau_s/2\right)^2 + \left(\triangle kL\right)^2}. \tag{2.55}$$

As the optical depth τ_s increases, the minima of the phase-matching curve fill up, as seen in figure 2-6. In the limit of an optically thick system with $\tau_i \gg 1$, the minima of the proceeding distribution fill up and we obtain a Lorentzian type profile for the phase-matching factor:

$$F\left(\triangle kL, \tau_i \ll 1, \tau_s \gg 1\right) = \frac{1}{\left(\tau_i/2\right)^2 + \left(\triangle kL\right)^2}. \tag{2.56}$$

When the phase-matching condition $\triangle k = 0$ is satisfied, the magnitude of the phase-matching factor in a medium will affect the optimal conversion efficiency of the medium. In the general case the phase-matching factor (2.52) with $\triangle k = 0$ reduces to

$$F\left(\triangle kL = 0, \tau_i, \tau_s\right) = \left[\frac{\exp\left(-\tau_s/2\right) - \exp\left(-\frac{\tau_s}{2}\right)}{\left(\tau_s/2\right) - \left(\tau_i/2\right)}\right]^2. \tag{2.57}$$

For the optically thin system the phase-matching factor (2.53) with $\triangle k = 0$ is approximated by $F\left(\triangle kL = 0, \tau_i \ll 1, \tau_{s\ll 1}\right) \approx 1 - \frac{\tau_s + \tau_i}{2}$ as a result of the expression $e^x = 1 + x + \frac{x^2}{2!} + \cdots$. For larger values of the optical depth τ_s, but with $\tau_i \ll \tau_s$ as in many media the phase-matching factor (2.55) with $\triangle k = 0$ is given by

$$F\left(\triangle kL = 0, \tau_i \ll \tau_s\right) \approx \left(\frac{2}{\tau_s}\right)^2. \tag{2.58}$$

Substituting this result into equation 2.47, we obtain the conversion efficiency expression:

$$\frac{\Phi_3\left(L\right)}{\Phi_1\left(0\right)} = \frac{64\pi^4\left(3\omega\right)^2}{c^4 n_3 \left(n_1\right)^3}\left[\frac{\left|\chi_T^{(3)}\left(-3\omega;\omega,\omega,\omega\right)\right|}{\sigma^{(1)}\left(3\omega\right)}\right]^2 \left[\Phi_1\left(0\right)\right]^2. \tag{2.59}$$

This equation illustrates that the conversion efficiency for third-harmonic generation is inde-

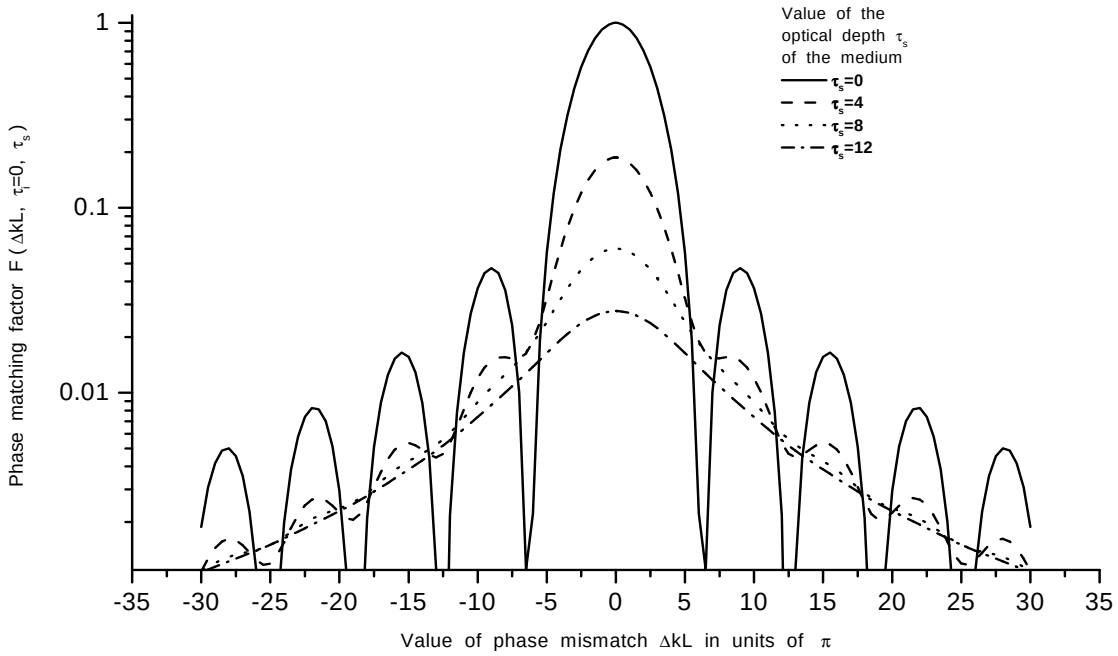

Figure 2-6: Theoretical phase-matching curves for different values of the optical depth (vertical axis is not linear scale).

pendent of the density N and medium length L (N and L must be within reasonable limits, allowing the assumptions that have been made above), and only depends on the ratio of the non-linear susceptibility $\chi_T^{(3)}$to the one-photon absorption cross section for the third-harmonic wave. This stresses the advantage of a small one-photon absorption cross section $\sigma^{(1)}(3\omega)$ for the third-harmonic.

2.1.7 Third-harmonic generation with focused beams

In experimental setups the incident laser beams are often focused to increase its intensity, because of the need to achieve large conversion efficiencies in a given non-linear medium. In this case, the plane-wave approximation is no longer valid and the incident beams should be described by Gaussian intensity distributions where the electric field for a single-mode beam is given by [2], [26]:

$$E_q(r,z) = \widehat{E}_q(r,z)\frac{b}{b+2iz}\exp\left[\frac{-k_q r^2}{b+2iz}\right]\exp(ik_q z) \tag{2.60}$$

where $b = 2k_q R_q^2$ is the confocal parameter and R_q^2 is the $\frac{1}{e}$ radius of the intensity distribution in the focal plane.

For an optically thin system the phase-matching factor is given by the following integral:

$$F(\triangle kL, b/L) = \frac{1}{L^2}\left(\int_{-L/2}^{L/2}\frac{e^{-i\triangle kz}}{(1+2iz/b)^2}dz\right)^2. \tag{2.61}$$

This phase-matching integral was first calculated by Ward and New [2] and has been reanalyzed by Bjorklund [35] and Puell et al. [28]. For the case of plane waves with $b \to \infty$, equation 2.61 reduces to equation 2.53.

Another very useful analytical result can be obtained for $L \geqslant b$. In this case of tight focusing the limits of the integral can be extended to infinity, and one obtains

$$F(\triangle kL, b/L \ll 1) = 0 \text{ for } \triangle kb \geq 0, \tag{2.62}$$

$$F(\triangle kL, b/L \ll 1) = \frac{\pi^2}{4}\left(\frac{b}{L}\right)^2(\triangle kb)^2 e^{\triangle kb} \text{ for } \triangle kb < 0. \tag{2.63}$$

The latter function goes through a maximum of $F(\triangle kb = -2, b/L \ll 1) = \left(\frac{\pi}{e}\frac{b}{L}\right)^2$ at $\Delta k = -2/b$. As a result, a single-mode Gaussian beam leads to a shift of the phase-matching maximum to $\triangle k = -2/b$, with the definition $b = 2k_q R_q^2$. The conversion efficiency becomes independent of length L and confocal parameter b and is proportional to the power of the fundamental wave $\pi R_1^2 \Phi_1$. As a rule of thumb, the optimum power conversion efficiency in phase-matched system is given typically for $b \approx L$.

2.1.8 Phase-matching

The discussion of the phase-matching factor in the previous two sections showed that it is critical to optimize the phase-matching factor for high conversion efficiencies. The phase-matching factor is influenced by

- the k-vector mismatch $\triangle k$
- the absorption losses τ_q
- the mode structure of the incident beams

the focusing condition b/L

The phase-matching factor is optimized by minimizing the k-vector mismatch Δk. The medium is phase matched for a non-linear process, such as third-harmonic generation, when the phase-matching condition $\Delta k = 0$ is satisfied. Physically, this means that the fundamental and third-harmonic waves must have the same phase velocity ($v_{\text{phase}} = \frac{c}{n}$) for the third-harmonic waves generated in different volume elements of the medium to interfere constructively.

The phase-matching condition is equivalent to the requirement for conservation of linear momentum $\overrightarrow{p}$

$$\overrightarrow{p}_s = \overrightarrow{p}_1 + \overrightarrow{p}_2 + \overrightarrow{p}_3 \tag{2.64}$$

using $\overrightarrow{p} = \hbar \overrightarrow{k}$ equation 2.64 can be rewritten:

$$\overrightarrow{k}_s = \overrightarrow{k}_1 + \overrightarrow{k}_2 + \overrightarrow{k}_3 \tag{2.65}$$

$$\triangle \overrightarrow{k} = \overrightarrow{k_1} + \overrightarrow{k_2} + \overrightarrow{k_3} - \overrightarrow{k_s} = 0 \tag{2.66}$$

where k is the wave vector. In the case of third-harmonic generation, where the fundamental and third-harmonic beams are collinear (they have the same direction and on one line), we can write

$$k_s = k_{3\omega} = \frac{3\omega n_3}{c} \tag{2.67}$$

and

$$k_1 = k_2 = k_3 = k_\omega = \frac{\omega n_1}{c}. \tag{2.68}$$

We can then write the phase-matching condition as

$$\triangle k = k_{3\omega} - 3k_\omega = 0. \tag{2.69}$$

By making use of $\frac{c}{v} = n$ we obtain $n(3\omega) - n(\omega) = 0$ which means that for phase-matching the medium has to have the same linear index of refraction for the fundamental wave and the third-harmonic wave.

2.1.9 Two-component gas medium for phase-matching for VUV generation

Harris and co-workers [10], [8] and [9] showed theoretically that the conversion efficiency of VUV generation in a gaseous system can be increased by several orders of magnitude using a two-component system. In our experiment krypton gas was chosen to provide the appropriate overall refractive index for phase-matching of the gas mixture, whereas magnesium vapor has been selected for its non-linear susceptibility. Figure 2-7 depicts the refractive index of magnesium in the region ω_0 to $3\omega_0$, where ω_0 is the angular frequency at 430 nm (and hence $3\omega_0$ the angular frequency at 140 nm). Due to resonances between ω_0 and $3\omega_0$, magnesium vapor exhibits negative dispersion between the resonance ω_0 and $3\omega_0$, which implies that the index of refraction at 140 nm is smaller than that at 430 nm ($n(\omega_0) > n(3\omega_0)$). Krypton gas is positive dispersive in the spectral region from 430 nm to 140 nm ($n(\omega_0) < n(3\omega_0)$), hence a pressure ratio can be found for which $n(\omega_0)_{mixture} = n(3\omega_0)_{mixture}$. In such an event it is said that the magnesium vapor medium has been phase matched for third-harmonic generation by the addition of an inert gas.

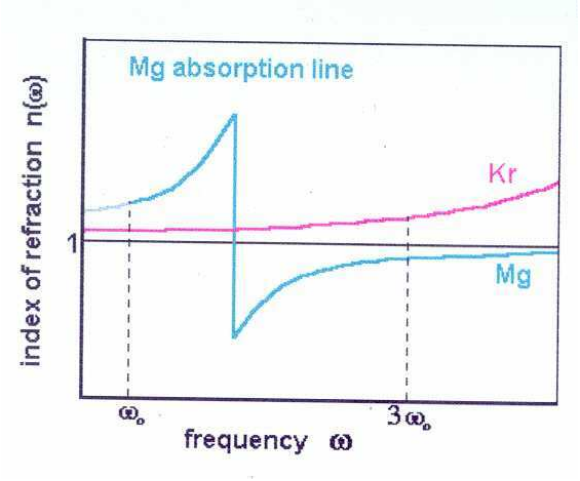

Figure 2-7: The refractive index of Mg in the region from ω_0 to $3\omega_0$ is shown schematically [4].

The correct density (pressure) ratio for phase-matching for third-harmonic generation in a two component gaseous system can be calculated if the real parts for the linear susceptibilities of both components at both the fundamental and the third-harmonic frequencies are known. The well-known Lorentz model for linear optics gives the relation between the linear susceptibility $\overline{\chi}_{\alpha}^{(1)}$, the density N_α and the refractive index $n(\omega)$ [4] (page 18,equation 2.21):

$$n(\omega) = 1 + 2\pi \sum_{\alpha} N_\alpha \overline{\chi}_{\alpha}^{(1)}(\omega) \tag{2.70}$$

the indices of refraction of the two-component system with specifies Kr and Mg at ω and 3ω are given by

$$n(\omega) = 1 + 2\pi \left[N_{Kr} \overline{\chi}_{Kr}^{(1)}(\omega) + N_{Mg} \overline{\chi}_{Mg}^{(1)}(\omega) \right] \tag{2.71}$$

$$n(3\omega) = 1 + 2\pi \left[N_{Kr} \overline{\chi}_{Kr}^{(1)}(3\omega) + N_{Mg} \overline{\chi}_{Mg}^{(1)}(3\omega) \right] \tag{2.72}$$

where N_{Mg} and N_{Kr} are the number densities of magnesium and krypton respectively. Phase-matching is achieved when

$$n(\omega) = n(3\omega) \tag{2.73}$$

$$N_{Kr}\overline{\chi}^{(1)}_{Kr}(\omega) + N_{Mg}\overline{\chi}^{(1)}_{Mg}(\omega) = N_{Kr}\overline{\chi}^{(1)}_{Kr}(3\omega) + N_{Mg}\overline{\chi}^{(1)}_{Mg}(3\omega) \tag{2.74}$$

giving

$$\frac{N_{Kr}}{N_{Mg}} = \frac{P_{Kr}}{P_{Mg}} = \frac{\overline{\chi}^{(1)}_{Mg}(3\omega) - \overline{\chi}^{(1)}_{Mg}(\omega)}{\overline{\chi}^{(1)}_{Kr}(\omega) - \overline{\chi}^{(1)}_{Kr}(3\omega)} \tag{2.75}$$

using $P = \frac{kTN}{V}$ with $\frac{kT}{V}$ a constant for the region of interest in the experiment.

Two factors are implied by equation 2.75:

1. This method of phase-matching requires the two-component medium to be very homogeneous and the partial pressures of the magnesium vapor and krypton gas to be well defined and stable.

2. It must be possible to adjust the number densities of each component of the gaseous medium in order to achieve the pressure ratio for phase-matching.

These stringent requirements are the reason why the cross concentric heat-pipe oven was chosen as our apparatus for our experiment.

2.1.10 Conclusion

In this chapter the basic principles of non-linear optics were reviewed. Non-linear susceptibilities $\chi^{(2)}$, $\chi^{(3)}, \cdots$, used to describe non-linear medium were discussed. All these non-linear susceptibilities give rise to non-linear polarization $P^{(NL)}$ at sum or different frequencies. All electromagnetic waves generated in non-linear medium at these frequencies can be derived through fundamental equations with non-linear polarization.

For gaseous medium, the lowest non-zero order susceptibility for non-linear process is the third order (discussed as third-harmonic generation in this section) because of the symmetry. For the application in mind in this work, it is therefore a challenge to find a suitable gaseous medium to avoid both a one-photon resonance (absorbing fundamental wave) and three-photon

resonance (absorbing generated third-harmonic wave), while a two-photon resonance is required to resonantly enhance their third order non-linear susceptibility.

In this work the aim is to optimize the tunable VUV generated by four-wave mixing. Angular momentum selection rules explain how the incident laser beams should be polarized to promote the generation of four-wave mixing. In order to discriminate against unwanted competing third-harmonic generation, two incident beams with left- and right circular polarization will be used.

In the small signal limit, the dominant non-linear susceptibility $\chi_T^{(3)}$ gives rise to third-harmonic generation. Derived expressions for conversion efficiency shows that the conversion efficiency is not only proportional to the square of the non-linear medium length (L) (as given in equation 2.54), of non-linear medium density number (N) and of fundamental intensity (Φ) but also depends on phase-matching condition based on $k - vector$ mismatch Δk, optical thickness and beam focusing condition. The phase-matching required can be obtained by regulating the partial pressure of Kr in the Mg vapor region.

To achieve large conversion efficiency in a given non-linear medium, incident laser beam was focused.

2.2 Molecular levels and transitions

In this section a general theoretical description of molecular levels and transitions will be outlined. Molecular levels and corresponding transitions are discussed. Two specific transitions relevant to experimental investigations in this project will be discussed in more detail (see section 2.2.3.1 and 2.2.3.3).

2.2.1 Molecular transitions

Molecular transitions occur between specific electronic, vibrational and rotational states, and hence the transition energies are determined by the difference in energies of the various states. The energy of a molecular state E can be expressed by the equation:

$$E = E_e + E_r + E_v \tag{2.76a}$$

with the electronic, rotational and vibrational energies E_e, E_r, E_v, respectively.

Using the relation $\upsilon = \frac{E}{hc}$ equation 2.76a can be written in terms of wave-number units:

$$\upsilon = \upsilon_e + \upsilon_r + \upsilon_v \tag{2.77}$$

- υ_e is the wave-number of the electronic state.
- υ_v is the wave-number of the vibration, expressed as

$$\upsilon_v = \omega_e \left(n + \frac{1}{2}\right) - \omega_e x_e \left(n + \frac{1}{2}\right)^2 + \omega_e y_e \left(n + \frac{1}{2}\right)^3 + \cdots \tag{2.78}$$

- υ_r is the rotational wave-number, expressed as

$$\upsilon_r = B_v J\left(J+1\right) - D_v J^2 \left(J+1\right)^2 + \cdots. \tag{2.79}$$

Equations 2.78, 2.79 come from reference [1]. The vibrational constants ω_e, $\omega_e x_e$, $\omega_e y_e$ depend on electronic states, whereas rotational constants B_v, D_v depend on both the electronic- and vibrational state. n and J are the vibrational and rotational quantum numbers. Generally, compared with υ_e and υ_v, rotational wave-number υ_r is small. In calculating the rotational wave-number, the second term in equation 2.79 is usually small compared to the first term, and can therefore be neglected in most cases.

Two different electronic states with their vibrational and rotational levels are presented graphically in figure 2-8. The single-primed letters refer to the upper states and the double-primed letters refer to the lower states.

2.2.1.1 Electronic transition

In an electronic molecular transition, the molecule can change from one electronic state to another electronic state by excitation of an electron to a higher orbital or electronic state. In this process the vibrational and rotational states can also change, or remain unchanged. For a given electronic transition where the vibrational and rotational states remain unchanged, the transition wave-number can be expressed by $\upsilon_e = \upsilon'_e - \upsilon''_e$.

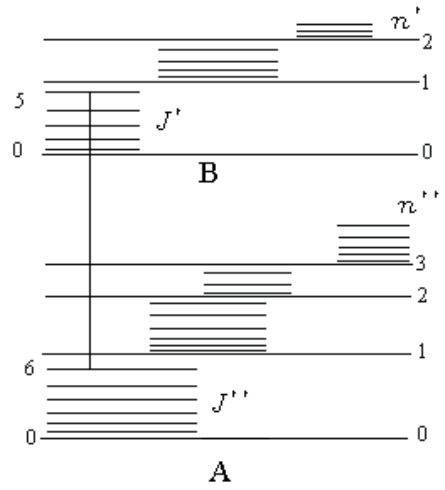

Figure 2-8: Schematic of vibrational and rotational levels of two electronic states A and B of a molecule. (only the first few vibration and rotation levels are drawn in each case). The transition between upper vibration-rotation state $n^{'}$=0, $J^{'}$=5 and lower vibration-rotation state n''=0, J''=6 is indicated by a vertical line.

2.2.1.2 Vibrational transition

For a given electronic transition, where there also is a change in vibrational energy but not in rotational energy, the transition wave-number can be expressed by equation 2.77, by neglecting the rotational transition, which then yields:

$$\upsilon_0 = \upsilon_e + \upsilon'_v - \upsilon''_v \tag{2.80}$$

with

$$\upsilon'_v = \omega'_e\left(n' + \frac{1}{2}\right) - \omega'_e x'_e\left(n' + \frac{1}{2}\right)^2 + \omega'_e y'_e\left(n' + \frac{1}{2}\right)^3 + \cdots \tag{2.81}$$

and

$$\upsilon''_v = \omega''_e\left(n'' + \frac{1}{2}\right) - \omega''_e x''_e\left(n'' + \frac{1}{2}\right)^2 + \omega''_e y''_e\left(n'' + \frac{1}{2}\right)^3 + \cdots . \tag{2.82}$$

Equation 2.80 represents all possible transitions between the different vibration levels of the two participating electronic states. There is no strict selection rule for the change in vibration quantum number n. The relative strength of the transition is determined by the Franck-Condon principle, which can be understood as follows[16]: *The electron jump in a molecule takes place*

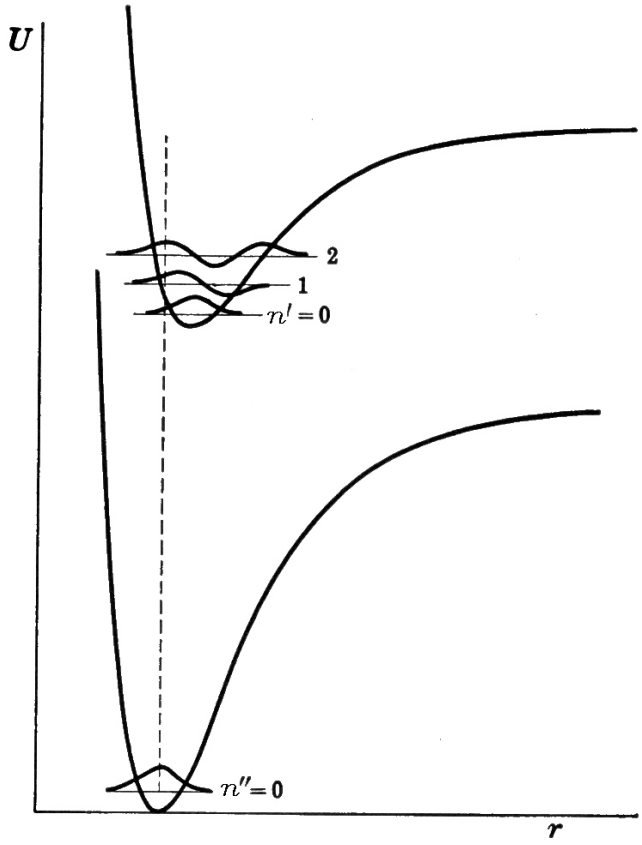

Figure 2-9: To illustrate the Franck-Condon Principle ([1] page 199), the eigenfunctions are shown, and the transition $n'\,(=2) - \; n''\,(=0)$ with the best overlap of the eigenfunctions is shown as broken vertical line in the figure.

so rapidly in comparison to the vibrational motion that immediately afterwards the nuclei still have very nearly the same relative position and velocity as before the "jump". In the wave-mechanical treatment [16] this means that for *transitions vertically upward or downward* in the potential energy diagram, the eigenfunctions that have the best overlap, give the largest dipole matrix elements and are responsible for the most intense bands (see the eigenfunctions in figure 2-9).

2.2.1.3 Rotational transition

For any given electronic transition including a vibrational transition and a rotational energy change is given by:

$$\upsilon = \upsilon_r + \upsilon_0 \tag{2.83}$$

where the quantity υ_0 given by equation 2.80 is independent of the rotational quantum numbers, while υ_r depends on the different values of the rotational quantum number in the upper and lower states according to equation 2.79. Therefore equation 2.83 can be written as

$$\upsilon = \upsilon_r\left(J'\right) - \upsilon_r\left(J''\right) + \upsilon_0 \tag{2.84}$$

where the rotational terms of the upper and lower state are

$$\upsilon_r\left(J'\right) = B'_v J'\left(J'+1\right) - D'_v J'^2\left(J'+1\right)^2 + \cdots \tag{2.85}$$

and

$$\upsilon_r\left(J''\right) = B''_v J''\left(J''+1\right) - D''_v J''^2\left(J''+1\right)^2 + \cdots \tag{2.86}$$

respectively, by using equation 2.79.

In order to apply selection rules for the rotational transition, the electronic angular momentum Λ should be considered. Selection rules for diatomic molecules are applicable to our case: if at least one of the two state has $\Lambda \neq 0$, the selection rule for J is, $\triangle J = J' - J'' = 0, \pm 1$ if both states have $\Lambda = 0$, then $\triangle J = 0$ is forbidden. To summarize three (or two) series of rational branches are:

$$R\left(J\right) : \upsilon = \upsilon_r\left(J'\right) - \upsilon_r\left(J''\right) + \upsilon_0 \ \ (\Delta J = 1) \tag{2.87}$$

$$Q\left(J\right) : \upsilon = \upsilon_r\left(J'\right) - \upsilon_r\left(J''\right) + \upsilon_0 \ \ (\Delta J = 0) \tag{2.88}$$

$$P(J) : \upsilon = \upsilon_r\left(J'\right) - \upsilon_r\left(J''\right) + \upsilon_0 \ \ (\Delta J = -1)\,. \tag{2.89}$$

2.2.2 Interaction of levels and coupling of motion

Here follows a brief review on the interaction of levels and the coupling of motion [1].

2.2.2.1 Obital angular momentum

In the symmetry of the electrostatic field of the two nuclei for a diatomic molecule, the electrons move in axial symmetry about the internuclear axis (which for the present is considered as fixed). As a result only the component of the orbital angular momentum L of the electrons parallel to the internuclear axis is a constant of the motion. A procession of L takes place about the field direction (internuclear axis) with constant component $M_L\,(h/2\pi)$, where M_L can take only the values

$$M_L = L, L-1, \cdots, -L. \tag{2.90}$$

This equation implies:

- States differing only in the sign of M_L have the same energy for that reversing the directions of motion of all electrons does not change the energy of the system but does change the sign of M_L in an electric field.
- States with different $|M_L|$ have in general widely different energies since the electric field which causes this energy splitting is very strong.

With the field stronger, L precesses faster about the axis of the field and consequently loses its meaning as angular momentum meaning while its component M_L remains well defined. It is thus more appropriate to classify the electronic states of diatomic molecules according to the value of $|M_L|$ than according to the value of L. Therefore,

$$\Lambda = |M_L| \tag{2.91}$$

where Λ, the component of the electronic orbital angular momentum along the internuclear axis, has values:

$$\Lambda = 0, 1, 2, \cdots, L. \tag{2.92}$$

For $\Lambda = 0, 1, 2, \cdots$ the corresponding molecular state are designated as $\Sigma, \Pi, \Delta, \Phi, \cdots$ states.

2.2.2.2 Spin

In atoms the fine structure of electronic bands is due to the electron spin. The spins of the individual electrons form a resultant S, the corresponding quantum number S being integral or half integral depending on whether the total number of electrons in the molecule is even or odd. In molecular states $\Pi, \Delta, \Phi, \cdots$, there is an internal magnetic field in the direction of the internuclear axis resulting from the orbital motion of the electrons. This magnetic field causes a precession of S about the field direction with a constant component $M_S\,(h/2\pi)$. For molecules, M_S is denoted by Σ, and has quantum values:

$$\Sigma = S, S-1, \cdots -S. \tag{2.93}$$

2.2.2.3 Total angular momentum of the electrons: Multiplets

The total electronic angular momentum about the internuclear axis, denoted by Ω, has the value

$$\Omega = |\Lambda + \Sigma|\,. \tag{2.94}$$

For molecules an algebraic addition is sufficient, since the vectors Λ and Σ lie along the line joining the nuclei.

According to international nomenclature, any term symbol $\square$, is denoted ${}^{2S+1}\square_{\Lambda+\Sigma}$. For example the ${}^3\Phi$ term has components ${}^3\Phi_4$, ${}^3\Phi_3$, and ${}^3\Phi_2$.

2.2.2.4 Coupling of rotation and electronic motion

In the sections mentioned above, the electronic motions caused by the field of two fixed nuclei has been taken into account. However in the actual molecule rotation and vibration take place simultaneously with the electronic motions. It is necessary to consider in which way these different motions influence one another.

Hund's coupling cases

In a molecule, electron spin, electronic orbital angular momentum, as well as angular momentum of nuclear rotation form a resultant **J**. The only exception is the $^1\Sigma$ state, because in the $^1\Sigma$ state both S and Λ are zero, the angular momentum of nuclear rotation thus it is identical to the total angular momentum **J**. In all other cases different modes of coupling of the angular momenta must be distinguished.

- **Hund's case (a)**

In this case the electronic motion is coupled very strongly to the line joining the nuclei by assuming that the interaction of the nuclear rotation with the electronic motion (spin as well as orbital) is very weak. In this case Ω and N (the angular momentum of nuclear rotation) couple to form **J**, given by

$$\mathbf{J} = \Omega, \Omega + 1, \Omega + 2, \cdots . \tag{2.95}$$

Figure 2-10 gives the vector diagram for this case. The vector **J** is constant in magnitude and direction. Ω and N rotate about **J** (nutation). At the same time, the procession of L and S takes place about the internuclear axis, which is assumed to be very much faster than the nutation of the figure axis in Hund's Case (a).

- **Hund's case (b)**

It is clear in figure 2-10, Ω is not defined when $\Lambda = 0$, and $S \neq 0$, because that the spin vector S is not coupled to the internuclear axis at all. Therefore Hund's case (a) cannot apply here. Sometimes, particularly for light molecules, even if $\Lambda \neq 0$, S may be only very weakly

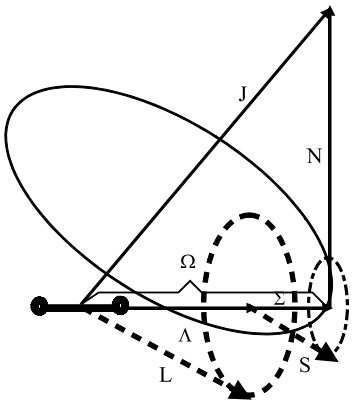

Figure 2-10: Vector diagram used to illustate Hund's case (a). The nutation of the figure axis is indicated by the solied-line ellipse; the much more rapid precessions of L and S about the line joining the nuclei are indicated by the dashed-line ellipses. Figure is drawn according to the literature [1] (page 219 figure 97).

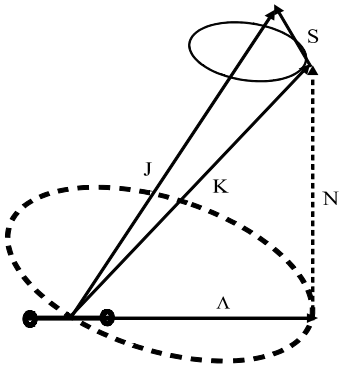

Figure 2-11: Vector diagram for Hund's case (b). The nutation of the figure axis, represented by the broken-line ellipse, is much faster than the precessions of K and S about J, represented by the solid-line ellipse. For $\Lambda = 0$, K is prependicular to the internuclear axis. Figure is drawn according to the literature [1] (page 221 figure 100).

coupled to the internuclear axis. This weak (or zero) coupling of S to the internuclear axis is the characteristics of Hund's case (b). In this case Λ and N couple to form K, given by

$$K = \Lambda, \Lambda + 1, \Lambda + 2, \cdots, \tag{2.96}$$

K is the total angular momentum excluding spin. K and S couples to form the total angular momentum $\mathbf{J}$, as shown in figure 2-11.

$\Lambda - type$ doubling

In Hund's case (a) and (b) the interaction between the rotation of the nuclei and L has been neglected. For larger speeds of rotation this interaction, however, produces a splitting into two components for each J value in the states with $\Lambda \neq 0$. In general, this splitting increases with increasing J. It is possible for all states with $\Lambda = 1, 2, 3, \cdots$ and is called $\Lambda - type$ doubling.

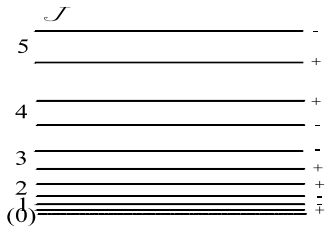

Figure 2-12: Diagram used to illustrate energy level splitting[4]. For the symmetric top, $\Lambda = 1$ is assumed, so there is no dotted level with $J = 0$.

Figure 2-12 shows such a splitting of a $^1\Pi$ state. As shown in the figure, J value consists of one positive (denoted by sign "+") and one negative (denoted by sign "−") component[2].

2.2.2.5 Selection rules

The selection rules mentioned in section 2.2.1 are applicable independent of the coupling case to which the electronic state under consideration belongs. Now another case holding only for a definite coupling case must be taken into account.

1. General selection rules: For any atomic system the selection rule for the quantum number **J** of the total angular momentum is $\Delta\mathbf{J} = 0, \pm 1$, with the restriction $\mathbf{J} = 0 \nrightarrow \mathbf{J} = 0$. This selection rule was mentioned in section 2.2.1. If considering $\Lambda - type$ doubling: for each J value there are one positive and one negative component, then the selection rules

[2]The sign of the rotational levels is decided by the total eigenfunction not of the rotational eigenfunction. The total eigenfunction remains unchanged upon a reflection at the origin, then the rotation level is positive; otherwise, the rotation level is negative.

[4]Total eigenfunction consists of electronic, vibrational and rotational eigenfunctions, in which vibrational eigenfunction depending on the magnitude of the internuclear distance doesn't change by reflection at the origin. When $\Lambda = 0$, and electronic eigenfunction remains unchanged by a reflection at the origin, the rotaional levels are positive for even J or negative for odd J. If $\Lambda \neq 0$, double degenerate energy levels have linearly independent eigenfunctions, which can be chosen so that one remains unchanged while the other changes sign for a reflection at the origin. This is the reason that in the figure + and − appears inversely.

employed here is that positive terms combine only with negative, and vice versa $+ \leftrightarrow -$, $+ \nleftrightarrow +, - \nleftrightarrow -$

2. Selection rules holding for Hund's case (a) as well as Hund's case (b): In both cases two quantum numbers Λ and S are defined. The selection rules for Λ are $\Delta\Lambda = 0, \pm 1$ which means that $\Sigma - \Sigma$, $\Sigma - \Pi$, $\Pi - \Pi, \cdots$ transitions but not $\Sigma - \Delta, \Sigma - \Phi, \cdots$ transitions can occur. Furthermore, $\Sigma^+ \leftrightarrow \Sigma^+$, $\Sigma^- \leftrightarrow \Sigma^-$, $\Sigma^- \nleftrightarrow \Sigma^+$. But, both Σ^- and Σ^+ states combine with Π states. And the selection rule for S is $\Delta S = 0$. This limits that only states of the same multiplicity combine with one another by the selection rule.

3. Selection rules holding only in case (a): If both states belong to case (a), the following rule holds for this quantum number:

$$\Delta\Sigma = 0 \tag{2.97}$$

which implies in an electronic transition the component of the spin along the internuclear axis does not alter. Therefore, transitions such as ${}^2\Pi_{1/2} - {}^2\Pi_{1/2}$, ${}^2\Pi_{3/2} - {}^2\Pi_{3/2}$, ${}^2\Pi_{1/2} - {}^2\Delta_{3/2}, \cdots$, but not ${}^2\Pi_{1/2} - {}^2\Pi_{3/2}$, ${}^2\Pi_{1/2} - {}^2\Delta_{5/2} \cdots$ take place.

4. Selection rules holding only in case (b): If both states belong to case (b), the following rule holds for this quantum number:

$$\Delta K = 0, \pm 1 \tag{2.98}$$

with the added restriction $\Delta K = 0$ is forbidden for $\Sigma - \Sigma$ transitions.

2.2.3 Application to three specific transitions

In order to be able to discuss the spectra (CO excitation fluorescence spectrum and nitrogen corona spectrum obtained in a nitrogen corona discharge) obtained in our experiment, it is necessarily to employ these selection rules in transitions: ${}^1\Pi - {}^1\Sigma$; ${}^1\Pi - {}^1\Pi$ as well as ${}^2\Pi - {}^2\Pi$. Among these transitions, the transition ${}^1\Pi - {}^1\Sigma$ is relevant CO excitation fluorescence spectroscopy, while the transition ${}^2\Pi - {}^2\Pi$ is relevant nitrogen corona spectrum.

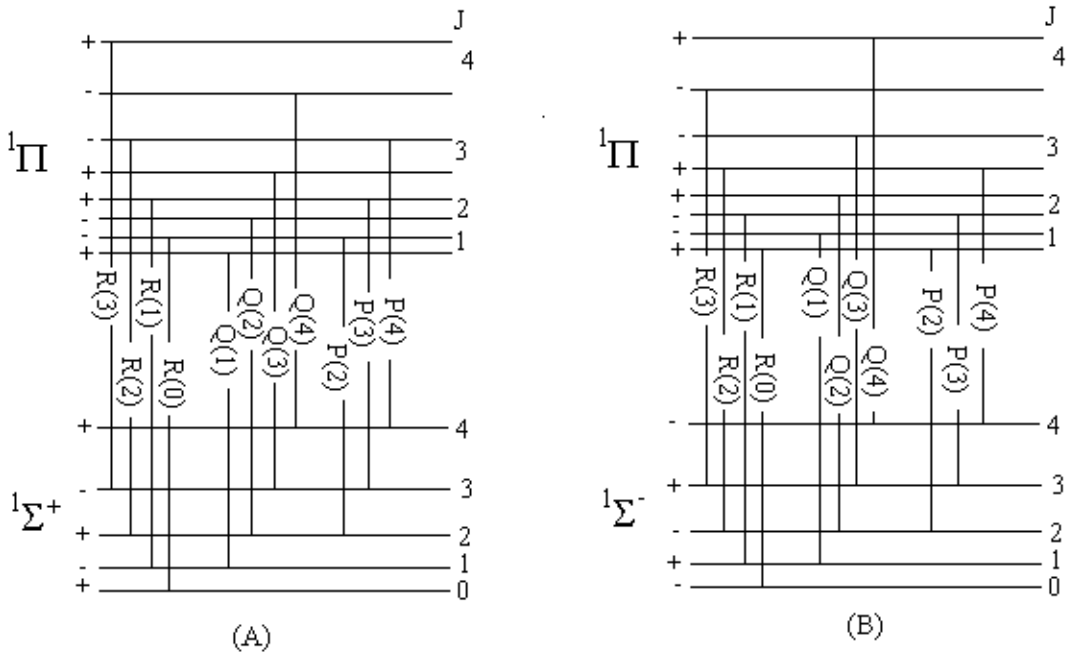

Figure 2-13: Energy diagram for the first lines of (A) a $^1\Pi - ^1\Sigma^+$ Transition; (B) a $^1\Pi - ^1\Sigma^-$ Transition (according to literature [1]).

2.2.3.1 $^1\Pi - ^1\Sigma$ transition

There is no difference between Hund's case (a) and (b) for the transition $^1\Pi - ^1\Sigma$, because the spin S and the orbital angular momentum Λ of the electrons are zero. According to selection rules $\Delta J = 0, \pm 1$, there are one P, one Q and one R branch in the transition $^1\Pi - ^1\Sigma$. While there is no $P(1)$ or $Q(0)$, because the smallest J value is $J = 1$ according to equation 2.95.

In the case of $\Lambda - type$ doubling, there will be one P, one Q and one R branch in the transition $^1\Pi - ^1\Sigma$. The reason for this is: (1) there is no splitting in rotational level J in $^1\Sigma$ state because of $\Lambda = 0$, while the splitting rotation level lies in state $^1\Pi$; and (2) according to selection rule $+ \leftrightarrow -$, the transition only happens between one of the two components of a $\Lambda - type$ doublet, $+$ or $-$, in the upper state and the lower state according to $-$ or $+$, as illustrated in figure 2-13.

In figure 2-13 it is shown that the upper state of a Q line is different from that of the P and R lines with the same upper rotation level J. Excitation of a Q line can only fluoresce as Q line (singlet resonance series); excitation of P or R line can fluoresce as both P and R lines; but no Q line (doublet resonance series). The relative transition intensities depends on molecular rotation temperature according to Boltzmann distribution.

2.2.3.2 $^1\Pi - ^1\Pi$ transitions

It is clear from the selection rules $\Delta J = 0, \pm 1$ that a $^1\Pi - ^1\Pi$ has a P, Q and R branch, ignoring $\Lambda - type$ doubling. When considering $\Lambda - type$ doubling, each energy level splits into two components, as figure 2-12 shows. For a given $J' - J''$ transition only two transition lines result due to the selection rule $+ \leftrightarrow -$, as illustrated in figure 2-14. A $^1\Pi - ^1\Pi$ band thus has six branches, double P, double Q, and double R branches, of which the two Q branches are very weak because $\Delta\Lambda = 0$.

2.2.3.3 $^2\Pi - ^2\Pi$ transitions

To analyze the nitrogen spectra obtained in the corona discharge, the $^2\Pi - ^2\Pi$ transition is relevant.

- If both $^2\Pi$ states of a $^2\Pi - ^2\Pi$ transition belong to Hund's case (a), the selection rule $\Delta\Sigma = 0$ holds. As a result, a $^2\Pi - ^2\Pi$ band splits into two sub-bands: $^2\Pi_{1/2} - ^2\Pi_{1/2}$ and $^2\Pi_{3/2} - ^2\Pi_{3/2}$. Each of them has a structure similar to that of a $^1\Pi - ^1\Pi$ transition: two P, two very weak Q, and two R branches, which form three closely spaced pairs. Thus a $^2\Pi(a) - ^2\Pi(a)$ band has twelve branches in total. Each sub-band has only one head and thus each band has two heads because of small $\Lambda - type$ doubling and very weak Q branches. The separation of the two heads is approximately constant for all the bands of a system.

- If both $^2\Pi$ states are approximated by Hund's case (b), the selection rule 2.98 holds. On the basis of these rules there are again twelve main branches corresponding to those of Hund's case (a), except that there are no two separate sub-bands.

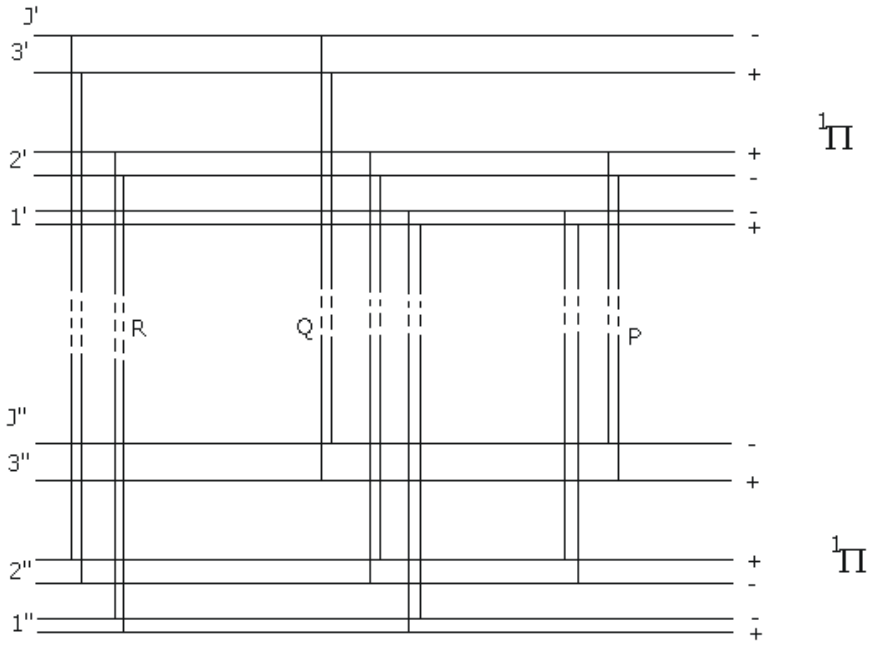

Figure 2-14: Diagram used to illustrate energy level for the first lines of a $^1\Pi - ^1\Pi$ transition. The $\Lambda - type$ doubling of the levels and of the lines are much exaggerated. The constants B of the rotation transition in both levels are assumed to be equal. Consequently the spacing of the lines in the Q branch could not be drawn to scale.

- For both $^2\Pi$ states Hund's case (a) holds for small J and Hund's case (b) holds for large J. The twelve branches for small J in Hund's case (a), go over into the twelve main branches of Hund's case (b) for large J.

2.3 Basic grating theory

Diffraction gratings are successfully used in spectroscopic instruments as dispersive elements. This is achieved by utilizing the grating's ability of diffract incident light into different angles according to the wavelength. The relationship between the incident angle, diffracted angle, and diffracted wavelength is given by the well known grating equation 2.99. Many of the most important spectroscopic quantities, such as dispersion, resolution and resolving power can be derived from the grating equation, from fairly straight forward algebraic manipulations.

2.3.1 Grating equation

Consider the geometrical path of two rays originating from the same point and converging to a common point as illustrated in figure 2-15. The geometrical path difference between rays coming from the source, and diffracted at two neighboring grooves towards the detector, can be seen to be $d(\sin\alpha - \sin\beta)$. If the path difference is an integral multiple of the wavelength, the two rays will again be in phase, and constructive interference occurs. For constructive interference the path difference should be $m\lambda$, and this principle leads to the relationship called the grating equation:

$$m\lambda = d(\sin\alpha \pm \sin\beta) \tag{2.99}$$

- m, the diffraction order
- λ, the diffracted wavelength
- d, the groove spacing of a grating
- α, the incident angle
- β, the diffracted angle

  For a particular wavelength λ incident on the grating surface (with groove spacing d) at

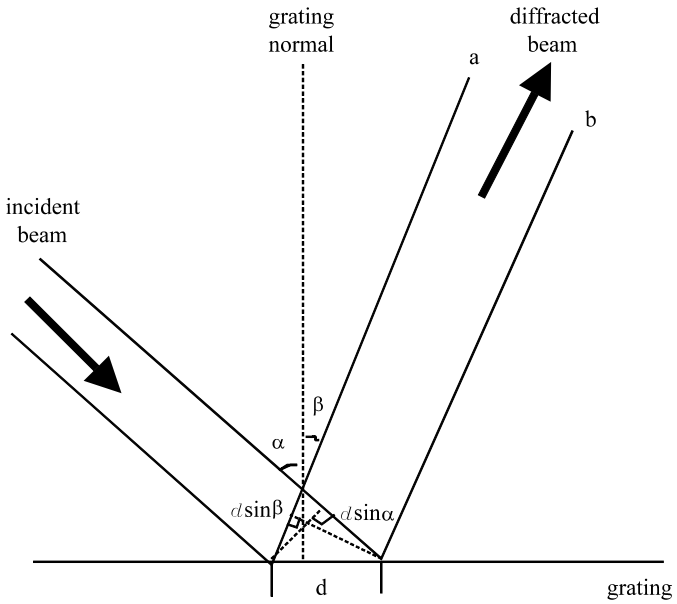

Figure 2-15: Geometry of diffraction. The ray is incident on the grating surface at an angle α, and is diffracted along an angle β, both angles are measured from the grating normal. The grating groove spacing is d. The difference in the geometrical paths for the incident and diffracted rays are shown to be $d\sin\alpha$ and $d\sin\beta$ respectively.

an angle α and diffracted from the surface, constructive interference for the $m-th$ order is obtained at angle β_m. The angles α and β_m are measured from the grating normal, which is the dashed line perpendicular to the grating centre as indicted in figure 2-16. m is the diffraction order, it can be positive, zero or negative, for instance $m = 0$, zero order; $m = \pm 1$, the first order; $m = \pm 2$, the second order, and so on. The sign of the diffracted angle (or the sign of m) is determined as follows: if the incident and diffracted rays are on the same side of the grating normal, the diffracted angle has positive sign (assuming that the incident angle is always positive), in other words, the diffraction order is positive; but if the incident and diffracted rays are on opposite sides of the grating normal, the diffracted angle has negative sign. This is depicted in figure 2-16.

The grooves of a grating can be shaped in such a way that from geometrical optics the incident ray is redirected in the direction of a chosen diffracted order. Such gratings are called blazed gratings, and this increases the reflection (or transmission) efficiency of the grating. The grating blaze wavelength refers to the wavelength for which the blaze condition holds, when the angle of incidence with respect to the facet normal is equal to the angle of reflection from the facet (see figure 2-17), expressed the by equation $\alpha - \varphi = \beta + \varphi$, while $m\lambda = d(\sin\alpha \pm \sin\beta)$ also holds. The choice of a facet angle depends on the choice of mount angle of the grating relative to the incident ray. The case where the light of the desired wavelength is diffracted back along the incident beam ($\alpha = -\beta$), is called Littrow mount. As mentioned, to obtain the best diffracted output intensity from a blazed grating, the wavelength region to be investigated is usually limited in the region close to the grating blaze wavelength.

2.3.2 Dispersion

2.3.2.1 Angular dispersion

The angular spread $d\beta$ of a spectrum of diffracted order m between the wavelength λ and $\lambda + d\lambda$ can be obtained by differentiating grating equation 2.99, assuming the incident angle α to be a constant.

Therefore the angular dispersion $D = \frac{\partial\beta}{\partial\lambda}$ is given by:

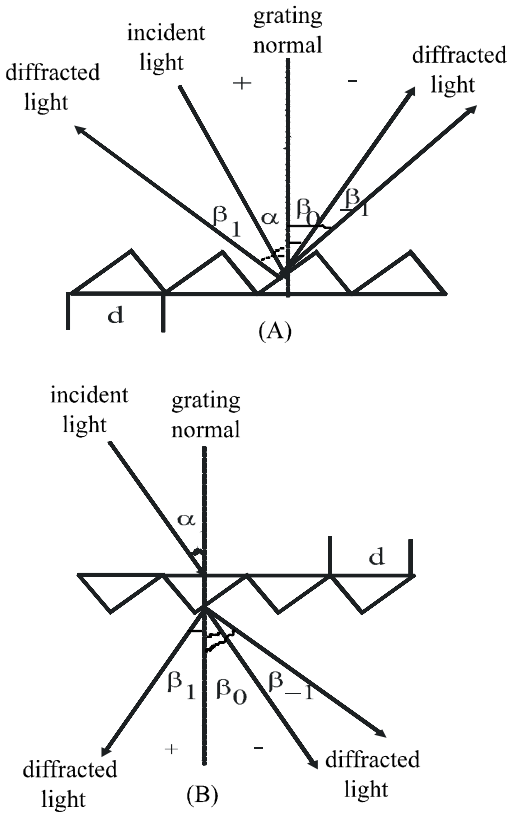

Figure 2-16: Diffraction by a plane grating. A wavelength is incident on a grating and diffracted along several directions. The signs for the angles are positive if they are on the same side of the grating normal as the incident ray, otherwise they are negative. (A) A reflection grating; (B) A transmission grating.

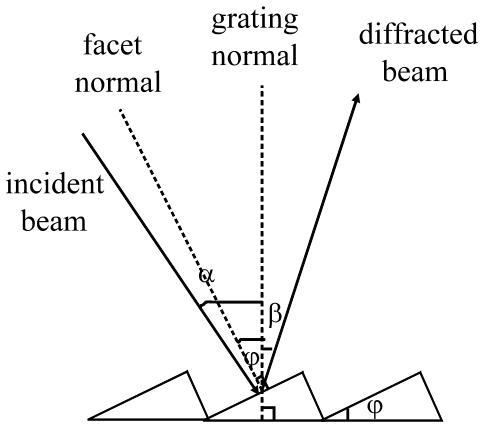

Figure 2-17: Diagram used to illustrate blaze configuration, the ray is incident at angle α and is diffracted from the grating surface at an angle β, both of them are measured from the grating normal. φ is the facet angle with respect to the grating surface.

$$D = \frac{\partial \beta}{\partial \lambda} = \frac{m}{d \cos \beta} \tag{2.100}$$

where β is the angle of diffraction as used in equation 2.99. According to equation 2.100, the angular dispersion will increase with higher diffracted order and larger grating frequency, which is the reciprocal grating groove spacing.

2.3.2.2 Linear dispersion

In practice, it is preferred to use linear dispersion which shows what change of wavelength corresponds to a given distance in the plane of the focused spectrum. The linear dispersion is simply the product of the angular dispersion and the focal length of the focusing element (the focusing mirror in the plane grating system or concave grating itself in the concave grating system), i.e:

$$\frac{\partial x}{\partial \lambda} = f \frac{\partial \beta}{\partial \lambda} \tag{2.101}$$

provided that the focal plane of the instrument is perpendicular to the diffracted beam. In real instruments, however, the angle ζ between the focal plane and the diffracted ray is not always 90°. In such cases the linear dispersion must be written as:

$$\frac{\partial x}{\partial \lambda} = F f \frac{\partial \beta}{\partial \lambda} \tag{2.102}$$

with plate factor $F = \frac{1}{\cos \zeta}$.

Two important facts should be noted: (1) the dispersion is not a constant at all points along the focal plane or as the grating is rotated and (2) high dispersion can be obtained by choosing high diffracted order, large number of grooves per mm, and long focal lengths.

2.3.3 Resolving power and resolution

Resolving power and resolution are used to describe the ability to distinguish between adjacent spectral lines in a spectrum. As a property of the grating, resolving power $\Re$ is the ratio between the wavelength λ at which it is operating and the smallest difference $\Delta\lambda$ in wavelength that the grating can resolve, $\Re = \frac{\lambda}{\Delta\lambda}$. The resolution of an instrument is the smallest difference in

center wavelengths between two peaks of equal intensity that can be resolved. Experimental resolution is a function of both the grating design and layout of the rest of the instrument, because it is limited by many other factors such as the quality of the grating surface, the optics, and the detectors.

In order to quantify the concept of resolution, the resolving power of the grating should be discussed. For this purpose, it is necessary to take into account the diffraction pattern in the focal plane of a monochromator as shown in figure 2-19.

The diffraction pattern of the aperture at the focal plane is represented by

$$I_x = I_0 \left(\frac{\sin \gamma}{\gamma} \right)^2 \tag{2.103}$$

where $\gamma = \frac{\pi w}{\lambda} \sin \beta$ is the difference in phase between contributions from the centre and the edge of the aperture, w is the width of the grating; β is the diffraction angle, and λ is the wavelength as illustrated in figure 2-18. Figure 2-19 is a plot of the flux density, as expressed by equation 2.103.

The first minimum for equation 2.103 occurs when $\gamma = \pi$ (see figure 2-19), i.e.

$$\frac{w'}{2} \sin d\beta \frac{2\pi}{\lambda} = \frac{w'}{2} \frac{x}{f\lambda} 2\pi = \pi \tag{2.104}$$

by assuming $\sin d\beta \approx \frac{x}{f}$ so $x = \frac{f\lambda}{w'}$.

If there are two wavelengths present and they differ by $\Delta\lambda$, then each will produce a diffraction pattern at the focal plane of the instrument, but according to equation 2.101 they will be displaced by an amount

$$\triangle x = \frac{\triangle \lambda f m}{d \cos \beta}. \tag{2.105}$$

Rayleigh's criterion is used to quantify the resolving power: two peaks will be resolved if the maximum of one peak coincides with the minimum of the other (adjacent) peak (see figure 2-20), i.e. $\triangle x = x$. The relationship is obtained:

$$\frac{\triangle \lambda f m}{d \cos \beta} = \frac{f\lambda}{w'}. \tag{2.106}$$

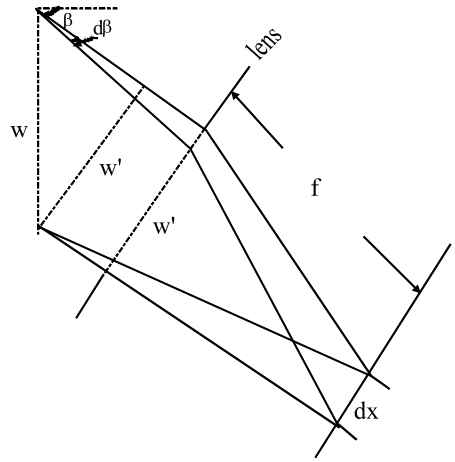

Figure 2-18: The resolution of different wavelengths with a grating. w is the grating width (representing grating surface), w′ is the width on the grating that is illuminated at the diffracted angle β, f is the focal length, dx is the minimum distance between two peaks with same intensity.

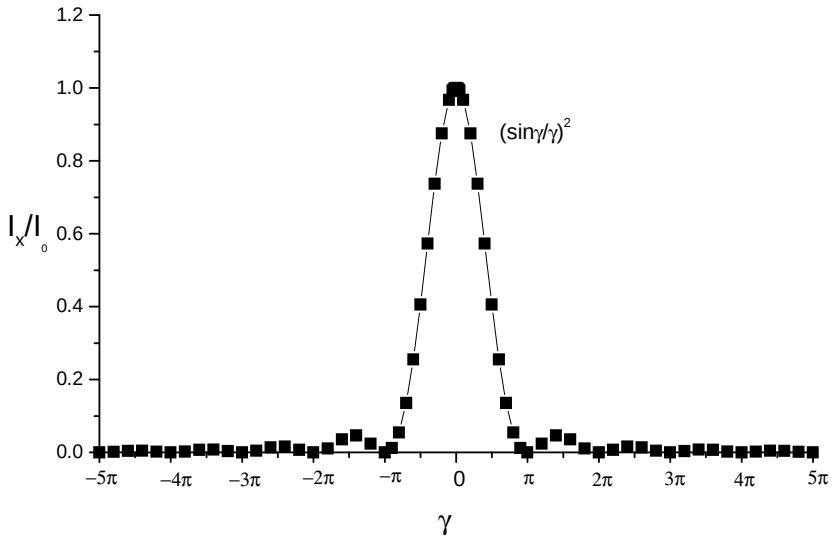

Figure 2-19: A plot of the flux density due to diffraction.

Using $w' = w\cos\beta$, $N = \frac{w}{d}$, and equation 2.99, another useful relation is obtained:

$$\Re = \frac{\lambda}{\triangle\lambda} = \frac{w\,|m|}{d} = |m|\,N = \frac{w}{\lambda}\left(\sin\alpha + \sin\beta\right) \tag{2.107}$$

where N is the total number of grooves, and m is the diffracted order. Equation 2.107 is the expression of the resolving power.

The physical significance of the expression 2.107 is:

- It illustrates the reason why large gratings illuminated is needed for high-resolution work. For a given groove spacing d used in a given grating order m, the resolving power only relies on the width illuminated of the grating according to the expression $\frac{\lambda}{\triangle\lambda} = \frac{w|m|}{d}$.
- The third expression $\left(\frac{\lambda}{\triangle\lambda} = |m|\,N\right)$shows the resolving power is the product of the diffracted order number and the total illuminated number of grooves on the grating (provided that the chosen order exists).
- The fourth expression $\left(\frac{\lambda}{\triangle\lambda} = \frac{w}{\lambda}\left(\sin\alpha + \sin\beta\right)\right)$ expresses the resolving power in terms of the angles of incidence and diffraction. It tells us that the resolving power is equal to

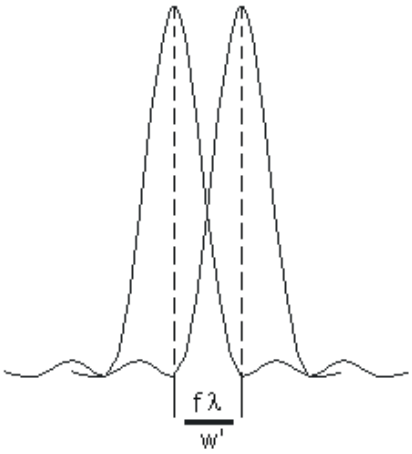

Figure 2-20: Diagram used to illustrate Rayleigh's criterion. (Two peaks with same intensities, the minimum of one is exactly at the maximum of the other.)

the total number of wavelengths contained in the path difference between light from the edges of the grating. Since $|\sin\alpha + \sin\beta| < 2$, the maximum attainable resolving power is $\left(\frac{\lambda}{\triangle\lambda}\right)_{\max} = 2\frac{w}{\lambda}$ regardless of the order m or number of grooves N.

2.3.4 Bandpass

The bandpass B of a spectroscopic system is the spectral interval that may be isolated. Bandpass B is defined as the Full Width at Half Maximum (FWHM) of the isolated peak, and it can be calculated by the equation:

$$B = W \times RCL \tag{2.108}$$

where W spectroscopic instrument output slit width, and RCL reciprocal linear dispersion of the grating (linear dispersion of a grating was given in equation 2.101). This equation can be re-written in terms of equation 2.101 and 2.100 by choosing an absolute value for diffracted order:

$$B = W \times \frac{d\cos\beta}{f\,|m|} \tag{2.109}$$

where W is the output slit width in equation 2.108; d is the grating groove spacing; β is the diffracted angle; f is the focal length of the focusing element and m the order of diffraction. From this equation, it can clearly be seen that for a given grating used in given order of diffraction, the smaller the exit slit width is, the smaller the bandpass is. However it is impossible to reduce the exit slit width infinitely because with it getting smaller, the intensity of the diffracted light also reduces. Also diffraction of the slit comes into play since small slit widths lead to diffraction broadening of the spectral line's image in the focal plane.

2.4 Monochromators

In this section we will discuss monochromator principle and illustrate what limits the scanned wavelength region in the monochromator..

2.4.1 The principle of monochromator

A monochromator has five principal components:

1. An entrance slit. It is the gate for rays to enter the monochromator.
2. A collimating element which makes the input light parallel.
3. A dispersing element. Generally a grating (plane grating) is used to disperse light intensity in space as a function of wavelength (see equation 2.99).
4. A focusing element. Through which the diffracted light can be focused at the exit slit of the monochromator or at the detector focal plane of a spectrometer.
5. An exit slit. It is on the focal plane to transmit light from the image formed by the focusing element.

In the case of a concave grating monochromator no collimating and focussing mirrors are necessary.

Usually, the output signal of a monochromator is a series of monochromatic images corresponding to wavelengths present in the light imaged on the entrance slit. The following two questions are addressed in the discussion about the monochromator:

1. How does it separate wavelengths?

2. What determines the measured wavelength limit?

Here only the constant deviation monochromator principle will be discussed since this kind of monochromator is used in the present experiment. For any constant deviation monochromator, which is a monochromator with two fixed slits-entrance slit and exit slit, the relationship between the incident angle and the diffracted angle is:

$$D_v = \beta - \alpha = constant \tag{2.110}$$

where D_v is called the deviation angle. Because the angle sustained by two fixed slits is a constant, the deviation angle from the incident ray to the diffracted ray is also constant and equal to the angle between two slits.

Substituting equation 2.110 in equation 2.99, gives an useful equation:

$$m\lambda = 2d\cos(\frac{D_v}{2})\sin(\alpha + \frac{D_v}{2}) \tag{2.111}$$

by using the equation:

$$\sin\alpha + \sin\beta = 2\sin\frac{1}{2}(\alpha+\beta)\cos\frac{1}{2}(\alpha-\beta). \tag{2.112}$$

Re-writing this equation in terms of λ, yields

$$\lambda = 2\frac{d}{m}\cos(\frac{D_v}{2})\sin(\alpha + \frac{D_v}{2}). \tag{2.113}$$

For any given grating used and a specific diffraction order observed with a standard deviation monochromator, d, m, and D_v will be constants. Then the diffracted wavelength, λ, appearing on the exit slit only depends on the incident angle α. Equation 2.113 is basic equation that governs a monochromator.

Generally, monochromators are equipped with a mechanism by which the incident angle α changes continuously, according to equation 2.113, and the diffracted wavelength λ at a selected diffracted order appears on the focal plane one by one.

2.4.2 Limiting wavelength region and monochromator resolving power

According to the information given in section 3.4.1, total number grating grooves for monochromator McPherson 218 is obtained by the calculation: $2400\,(lines/mm) \times 52.8$ mm $= 126720$ lines. Using equation 2.107 $\frac{\lambda}{\triangle\lambda} = mN$, the grating's theoretical resolving power for the first order ($|m| = 1$) is 126720. It is convenient to calibrate the monochromator system resolution for any arbitrary wavelength due to equation 2.107.

To calculate the theoretical diffraction wavelength range, two measurements should be performed:

1. Measure the deviation angle. For this monochromator the value obtained was $D_v = 44°$.
2. Measure the incident angle α at the mechanical stop for the rotation of the grating. The result is: $\alpha = -22°$ to $\alpha = 21°$.

Using equation 2.110, with the results obtained in the two measurements, the theoretical wavelength range is calculated to be: 0 nm $\rightarrow$ 537 nm, and 0 nm$\rightarrow$ 268.5 nm for first-order and second-order diffracted, respectively. In the experimental setup first-, and second-order wavelength is limited to the range from 105 nm to 500 nm and 52.5 nm to 250 nm, respectively, due to the geometry of the optical layout.

In the present work the monochromator McPherson 218 is used in the wavelength range from 144 nm to 147 nm. This wavelength region could be observed in the first-order or second-order. Our spectra were recorded in the first order. The second order diffraction wavelength, which could overlap with the first order (see equation 2.99), is not registered by the VUV photomultiplier that is only sensitive to wavelengths from 105 nm to 220 nm.

Chapter 3

Experimental setup

An experimental facility was set up for high resolution spectroscopy of supercooled molecules in the vacuum ultraviolet (VUV). For high resolution spectroscopy tunable lasers are required, but no tunable lasers are commercially available in this wavelength region. A VUV source was developed that is produced by four-wave frequency mixing in a gaseous medium. The VUV laser source consists of a Mg filled heat-pipe pumped by two dye lasers to produce narrow band tunable VUV radiation. The gas sample is injected through a pulsed valve as a supersonic jet into the irradiation chamber, to cool the molecules to simplify the spectra. A detection system for the VUV makes it possible to optimize the VUV source. The fluorescence detection system consists of a monochromator and photomultiplier to detect fluorescence after excitation. A fast data acquisition system is used to record the spectra.

3.1 VUV laser setup

The tunable VUV laser source used in the present research has been set up in the laser laboratory of the Physics Department, University of Stellenbosch, by Christine M. Steinmann during her MSc project. In this section, we only give a brief overview of the layout. A comprehensive description can be found in her thesis [4].

VUV laser source setup is shown in figure 3-1. Two Lambda Physik FL 3001X dye lasers (LC 4400, with Coumarine 120 dye dissolved in methanol) are pumped by a Lambda Physik EMG 203 MSC XeCl excimer laser. VUV photons are produced by four-wave mixing in the crossed

concentric heat-pipe oven through the interaction of the incident beams with magnesium vapor as non-linear medium, while Kr inside the heat-pipe is used for phase-matching. Dye laser I is tuned to a two-photon resonance in the magnesium-vapor krypton gas medium at wavelength 430.88 nm. Using only this laser to pump the Mg vapor, gives VUV output at 143.6 nm (third-harmonic generation). Dye laser II is tunable from 436 nm to 460 nm using Coumarine 120 as dye dissolved in methanol. Using both lasers, with the beams collinearly focused in the Mg vapor, a VUV output that is continuously tunable from 144.2 nm to 146.7 nm can be produced by sum-frequency generation. If both dye lasers are plane polarized (vertical) the third-harmonic of the dye laser wavelength tuned to the two-photon resonance is generated, because it is the dominant process. To obtain tunable VUV, the two laser beams must be right and left circularly polarized respectively. This is because opposite circular polarization of the incident laser beams ensure that the generation of the third-harmonics of either of the incident frequencies is forbidden by angular momentum selection rules, while the generation of the sum-frequencies is allowed (see chapter 2 section 2.1.5). The linear polarization of the dye laser I beam is changed by 90 degrees by inserting a double Fresnel rhombus[1]. The polarization of the two perpendicularly plane polarized beams are converted to right and left circular polarization in a single Fresnel rhombus after they are combined collinearly using a Glan prism. To increase incident beams intensity, the collinear beams are focused (see equation 2.54 in section 2.1.6) with a lens to have the beam waist approximately in the centre of the gaseous medium [2]. In the heat-pipe oven, two incident beams interact with magnesium gas to produce VUV, whereas phase-matching is achieved by adding krypton gas. Three laser mirrors are used to adjust the laser beam height to align it through the heat-pipe oven because the instruments are fixed on an optical table and cannot easily to be aligned to the laser beam.

[1]The basic principle of a Fresnel rhombus is given here. A relative phase change between the polarization directions ($E^{\shortparallel}$ or $E^{\perp}$) on total internal reflection can be effected by choosing the correct angle of incidence. The phase change can be deduced the Fresnel equations. The phase difference between the reflected components $E^{\shortparallel}$ and $E^{\perp}$ is 45° under the conditions $n \approx 1.5$ and $i \approx 50°$. Therefore after two such total internal reflections the phase difference between the two polarizations becomes 90°; and if the two components have equal amplitude, the result is circularly polarized light.

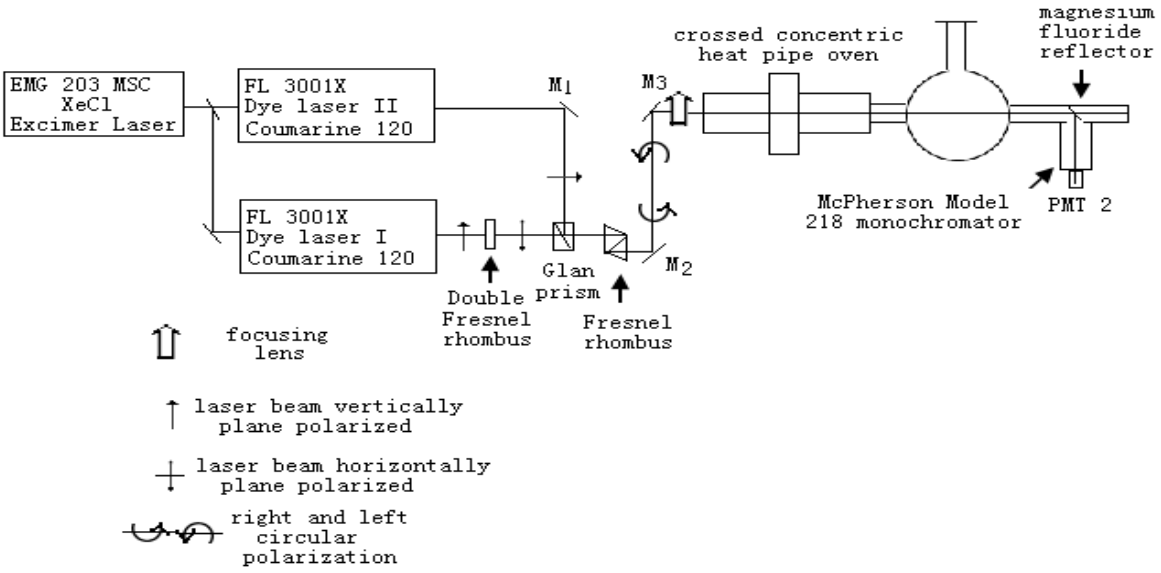

Figure 3-1: Experiment setup for VUV.

3.2 Heat-pipe setup

In section 2.1.9, we discussed that phase-matching can be achieved if the partial pressures of the Mg vapor and the Kr can be independently adjusted. To meet the very stringent phase-matching condition, a crossed concentric heat-pipe oven was used, because the total column density of Mg inside the heat-pipe oven is very stable, and partial pressure of Kr can be added without affecting the Mg vapor column. In this section the crossed concentric heat-pipe oven will be described, with emphasis on the principle of operation and its construction.

The crossed concentric heat-pipe oven used in our experiment is illustrated in figure 3-2, and its photo is shown in figure 3-3 (figure just illustrates the construction in the heat-pipe not the whole system). It consists of two separate heat-pipes: a horizontal heat-pipe inserted into a vertical one with only thermal contact between them. The vertical heat-pipe has been filled with 100 cm^3 sodium as working material, and argon gas to provide an external argon pressure P_1 which determines the temperature of the oven according to the vapor pressure curve of the working material, in this case sodium. The horizontal heat-pipe uses 13 cm^3 magnesium as working material and krypton as buffer gas at an external krypton pressure P_2. The reason

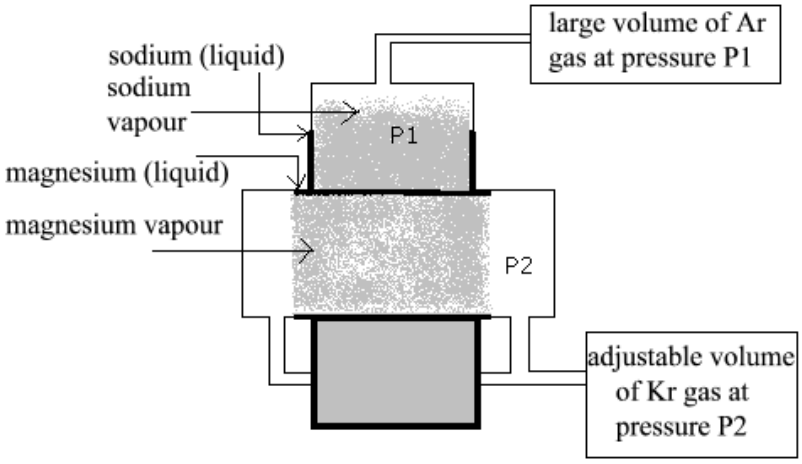

Figure 3-2: Schematic illustration of a crossed concentric heat pipe oven.

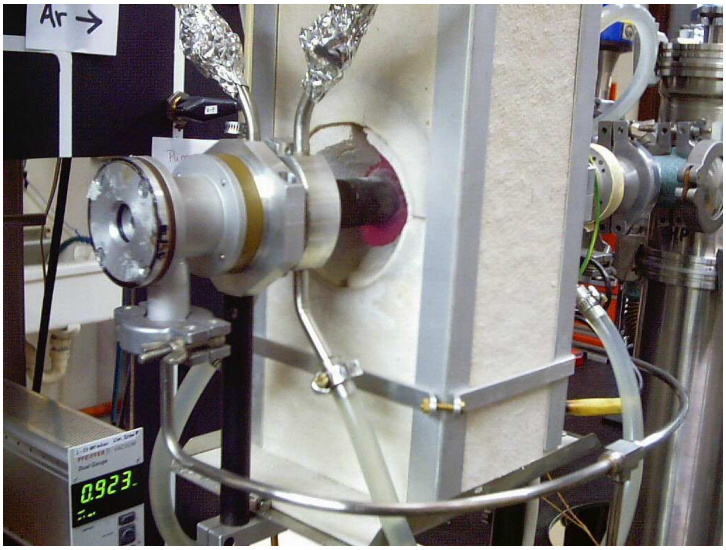

Figure 3-3: A photo shows the crossed concentric heat pipe oven used in our experiment.

why sodium and argon were chosen to fill the vertical heat-pipe is that the vapor pressure of sodium for a particular desired temperature is higher than that of the magnesium vapor, which keeps stable equilibrium and avoids start-up problems [32], and argon is readily available and is an inexpensive noble gas.

The vertical heat-pipe filled with sodium is heated at the bottom by a heating element providing a constant heating power. The sodium vapor and the Ar does not mix, hence the external argon pressure P_1 determines the sodium vapor pressure: $P_{Na} = P_1$ which through the vapor pressure curve determines the temperature T_{Na} of the sodium (as the boiling temperature of sodium at pressure P_{Na}). Since the temperature is regulated according to the sodium vapor pressure curve, the temperature $T = T_{Na}$ can be kept stable by keeping the external Ar pressure stable. In this way the vertical heat-pipe imposes an extremely homogeneous temperature distribution on the middle section of the horizontal heat-pipe.

The horizontal heat-pipe thus has a constant temperature $T = T_{Na}$, which determines, according to the magnesium vapor pressure curve, the partial vapor pressure of magnesium $P_{Mg}(T)$ in the middle section of the pipe which is thermally connected to the vertical pipe. The external krypton pressure P_2 higher than expected value of the vapor pressure $P_{Mg}(T)$ can be chosen, hence the middle section contains a homogeneous mixture of magnesium vapor and krypton gas with partial krypton pressure P_{Kr} equal to the difference between the external krypton pressure P_2 and the partial pressure of the magnesium vapor $P_{Mg}(T)$.

$$P_{Kr} = P_2 - P_{Mg}(T) \tag{3.1}$$

Adjusting external argon pressure P_1 and krypton pressure P_2, both the magnesium vapor pressure $P_{Mg}(T)$ and the partial krypton pressure in the two-component medium P_{Kr} can be adjusted independently. In practice phase-matching as determined by equation 2.75 is achieved by choosing a suitable value for the partial magnesium vapor pressure by choosing the correct external argon pressure and then adjusting the krypton pressure. In the two-component gas medium, the ratio of the two gas pressures calculated by equation 2.75 is satisfied in our experiment.

From the known vapor pressure curves, both the temperature and magnesium vapor pressure

can be estimated[2] and for the use of the heat-pipe oven for vacuum ultra-violet generation this is sufficient. By means of the bellow and taps in the system the external krypton pressure can be lowered or raised in a slow and controlled way, even beyond the adjusting range of the bellow volume (see manual [11]).

3.3 Pulsed valve for supersonic jet

The pulsed free supersonic jet apparatus consists of a gas reservoir (adjustable volume, 2.2 to 2.9 liter) connected to a vacuum chamber through a pulsed valve. A solenoid valve (General Valves series 9, Part nr, $9-181-900$) is driven by a home-built pulsed voltage source. The valve has an opening time of about 1 ms and could provide gas pulses with average duration of about 0.8 ms.

The CO and Ar gas mixtures used in this experiment are stored in the gas reservoir, in which the gas pressure (maximum pressure 7 bar) is much higher than the pressure in the vacuum chamber. The gas is allowed to escape from the reservoir into the vacuum chamber through a nozzle (as shown in figure 3-4). This process is called supersonic expansion. In this process the energy associated with the random thermal motion of the gas particles decreases and the width of the velocity distribution of the gas particles (a measure of the translational temperature) narrows, resulting in an extremely low gas temperature after expansion. As a result of the supersonic expansion most CO molecules are in the lower vibrational and rotational levels. Temperatures of a few Kelvin are achieved in this way, hence laser excitation of the molecules will be predominantly from the lower rotational levels of the ground state.

3.4 Detection systems

The photon detection systems used in this work can be divided into three categories: i) Conventional emission and absorption spectrometer, ii) Detection system for the VUV laser output, either to optimize the VUV output or to measure the transmitted VUV after absorption, and iii) Detection system to measure the fluorescence subsequent to the excitation by the laser.

[2] In this setup no provision is made to measure them independently.

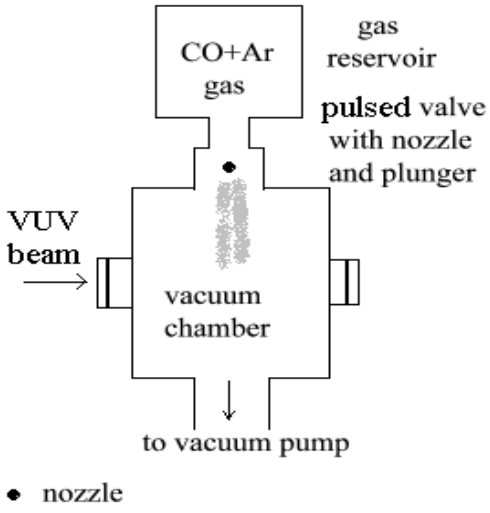

Figure 3-4: Diagram illustrating the irradiation chamber with the pulsed gas jet crossing the VUV beam.

3.4.1 Monochromator systems

Two monochromator systems were used in this project: McPherson Model 225 monochromator was used to measure the emission spectrum of nitrogen in both a corona discharge and a microwave discharge in the UV. In separate experiments a conventional vacuum monochromator (McPherson Model 218) was connected with the setup for high-resolution vacuum ultra-violet laser spectroscopy. This monochromator also facilitated the measurements for the optimization of the two-photon resonance four-wave frequency mixing process generating VUV in the gaseous medium and the recording absorption spectra.

3.4.1.1 McPherson Model 225 monochromator setup

McPherson Model 225 monochromator optical system consists of two slits (entrance and exit slit) and a concave grating (one-meter radius of curvature). The specifications supplied for the monochromator are: concave grating focal length 995.4 mm, ruled width 96 mm, grating grooves 1200 lines/mm, giving a reciprocal linear dispersion of 0.83 nm/mm. The grating is

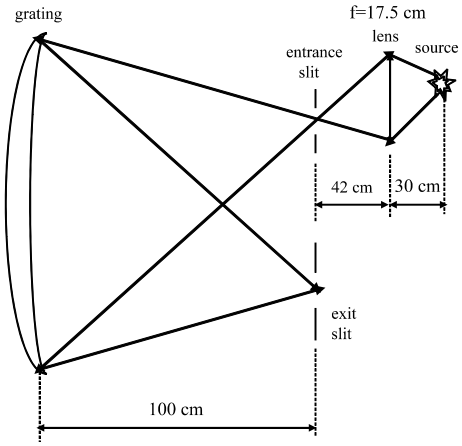

Figure 3-5: McPherson 225 monochromator optical design.

blazed for wavelength 120 nm, deviation angle 15°, with both slits on the concave grating focus. Monochromator selects wavelengths from about 30 nm up to 300 nm, with resolution of 0.015 nm. A concave grating in this monochromator combines in one component several functions: collimating, dispersion and focusing.

The optical setup for using the McPherson Model 225 monochromator to analyze the emission of a gas discharge is shown in figure 3-5. A quartz lens $f = 175$ mm is used to focus the light onto the monochromator entrance slit, which is the focus of the concave grating. Placing it 42 cm from the entrance slit, the whole grating is illuminated, and the resolution of the system is optimized.

A Sputter-ion pump (IZ pump) was supplied with the monochromator. The operating principle is that the gas molecules are trapped and retained by sorption inside the pump. The

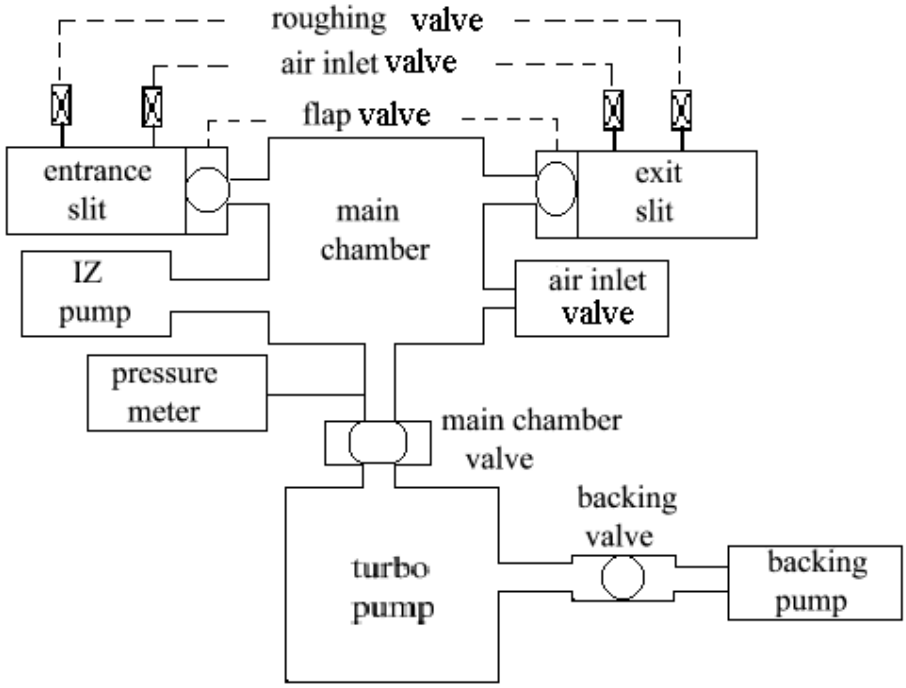

Figure 3-6: Schematic illustration of the McPherson 225 spectrometer vacuum system.

number of free gas particles in the connected chamber is thus reduced, in other words the gas pressure is reduced and produces a vacuum. The sorption of the gas particles takes place at the surface of reactive metal layers, so-called getter films, which are continually renewed therefore the sorption effect is not reduced due to saturation, hence this pump can keep on working over weeks or even months. A turbo-molecular pump (Pfeiffer Balzers, TPU 240, 230 l/s) was chosen as our fore pump. This is because we can (i) obtain high-vacuum pressure in short time, (ii) extend the life time of the IZ pump, and (iii) get good ultimate pressure of the pressure 10^{-7} torr.

3.4.1.2 McPherson 218 monochromator setup

McPherson 218 monochromator is a plane grating spectrometer. Typical monochromator optical system used in the experiments consists of five elements: entrance slit, collimating mirror, plane grating, focusing mirror and exit slit and is shown in figure 3-7. The collimating mirror

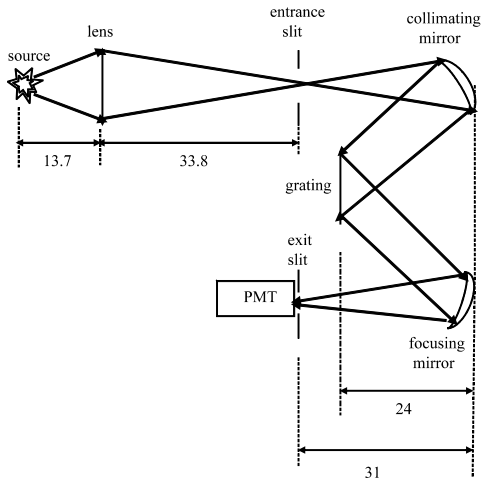

Figure 3-7: Typical monochromator system setup for measuring LIF spectra. Unit in the figure is cm.

is 31 cm from the entrance slit, and the focusing mirror is 31 cm from the exit slit. Both spherical mirrors are fixed and have the same focal length 0.3 m; they are both 24 cm from the plane grating. The grating has 2400 lines/mm, the rule width of 52.8 mm, and coated with Al and MgF_2. Blaze angle is 21.1°, corresponding blaze wavelength is 300 nm, reciprocal linear dispersion is 1.33 nm/mm.

The point source (excited molecules) was placed 13.7 cm from a plano-convex magnesium fluoride lens, with focal length $f_{157\mathrm{nm}} = 10.46$ cm. For any lens the focal length f is given by the lens maker equation:

$$\frac{1}{f} = (n-1)\,\frac{1}{R} \tag{3.2}$$

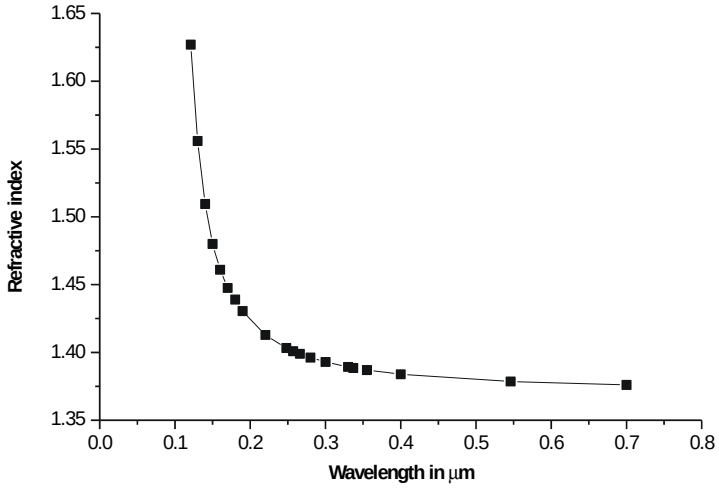

Figure 3-8: The graph illustrating the magnesium fluoride refractive index as a funcion of the wavelength. Manufacturer data sheet comes from Crystran Ltd: www.crystran.co.uk/mgf2data.htm.

with n the refractive index and R radius curvature of the plano-convex lens. The relationship between f and n for magnesium fluoride is shown in figure 3-8.

The wavelength region of interest in this experiment was around 144.7 nm (CO molecules transition $(A^1\Pi\,(3) - X^1\Sigma^+\,(0))$ which differs from the design wavelength of the lens focal length of 157 nm. This required re-calculation of the lens focal length for the experiment. Using the information from the figure 3-8 and using equation 3.2 the focal length of this magnesium fluoride lens was calculated: $f_{144.7\mathrm{nm}} = 9.83$ cm. Using the lens equation $\frac{1}{f} = \frac{1}{v} + \frac{1}{u}$ with $f = 9.83$ cm, $u = 13.7$cm, the image of the point source is calculated to be 34.8 cm from the lens. This ensures the light from the point source gets on the focus of the collimating mirror after the magnesium fluoride lens. So the light is incident parallel on the plane grating (see figure 3-7) and illuminates the whole grating therefore the resolution is optimized (see section 2.3.3).

In order to use the monochromator in the VUV it has to be evacuated. A vacuum system was built up for this purpose, and a schematic is shown in figure 3-9. In order to evacuate the system, a mechanical pump (CIT-ALCATEL 370 C55, r.p.m: 1450) was used as backing pump for an oil diffusion pump (Edwards Diffstak 63). To protect monochromator from being

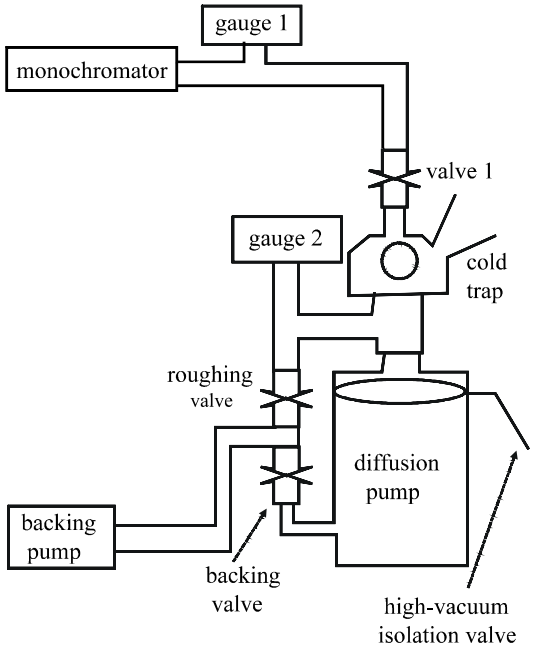

Figure 3-9: McPherson 218 spectrometer vacuum system.

polluted by oil a cold trap was installed, and filled with liquid nitrogen during the experiments. Two gauges (gauge 1: LEYBOLD-HERAEUS 162 92 4420; and gauge 2: BALZRS, type NV 3) were used to measure the vacuum pressure. A pressure of 10^{-4} torr was achieved.

3.4.2 VUV laser output detection system

To characterize VUV output in figure 3-1, a part of the beam that comes from the heat-pipe oven is split off by a reflector (MgF_2 mirror) towards the monochromator entrance slit center, passes the monochromator optical system and is detected by a solarblind photomultiplier PMT 2 (EMR Photoelectric, model 542G-08-18, Cs-I cathode) placed at the exit slit. The typical monochromator optical system used to record the VUV is shown in figure 3-7.

3.4.3 Fluorescence detection system

The fluorescence detection systems refers to the experimental setup for fluorescence spectroscopy. Laser-induced fluorescence (LIF) spectra can be obtained when supercooled CO molecules are excited to higher energy levels through the absorption of VUV laser photons. Two types of LIF spectra are relevant in this work: fluorescence excitation spectra; and dispersed fluorescence spectra. These two setups are described in the next sections.

3.4.2.1 Fluorescence excitation spectroscopy setup

In fluorescence excitation spectroscopy, the laser wavelength is tuned while measuring the total fluorescence, using for example a photomultiplier tube. The fluorescence excitation spectroscopy setup is shown in figure 3-10. PMT 2 (a solarblind photomultiplier, EMR Photoelectric, model 542G-08-18, Cs-I cathode) records the total fluorescence at right angles to the excitation beam. With the monochromator also connected as indicated in figure 3-1 to record the transmitted VUV, the absorption spectrum can be recorded simultaneously. By setting up the monochromator to cover a wider spectral region, sufficient to separate the tunable VUV laser radiation from the third-harmonic, absorption spectra of high resolution could be recorded.

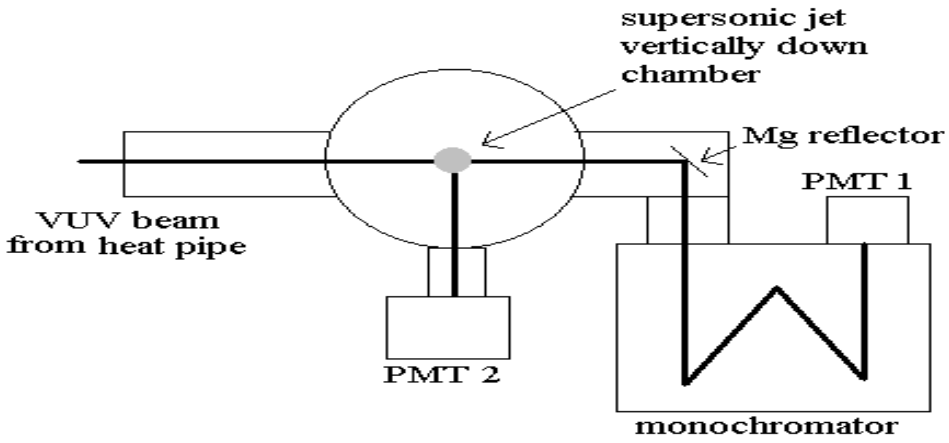

Figure 3-10: Experimental setup used in laser induced fluorescence spectroscopy of CO molecules. (Setup for generated tunable VUV laser beams including heat pipe oven is already given in figure 3-1, monochromator optical system setup is given in figure 3-7.)

3.4.2.2 Fluorescence spectroscopy setup

An experimental setup was also designed to be able to record the fluorescence spectrum. The method entails the excitation of a molecule, and measuring the subsequent fluorescence spectrum. Compared to the high-resolution VUV excitation spectroscopy, the monochromator setup has low resolution, but may be sufficient to distinguish between different rotational transitions sufficiently to be able to identify the transitions. In our case the laser wavelength was set at a specific absorption wavelength of the sample ($^{12}C^{16}O$ molecule in our case) and the emitted fluorescence spectrum could be recorded using a monochromator. As indicated in figure 3-11, the monochromator was connected to the fluorescence chamber, at right angles to the CO supersonic jet, and at right angles to the VUV laser beam. A solarblind photomultiplier (PMT 2) was used as detector in the monochromator.

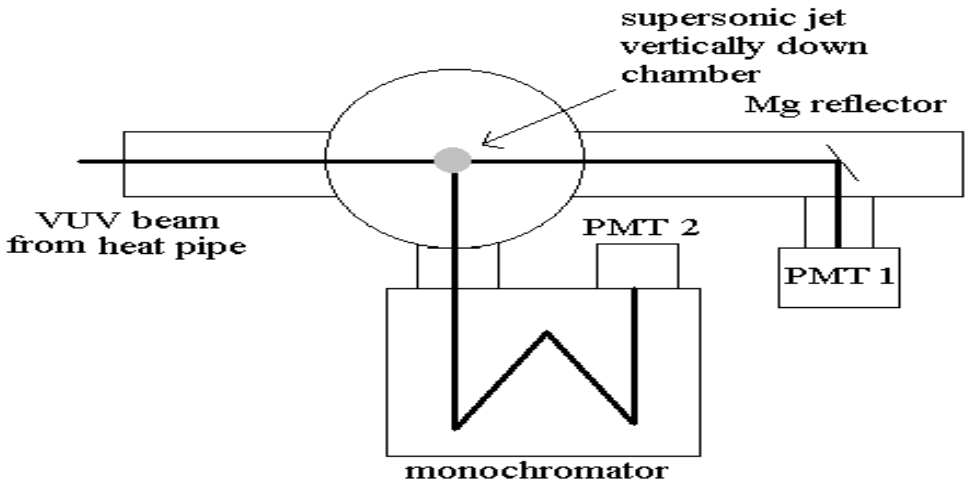

Figure 3-11: Experimental setup for obtaining the absorption spectrum of CO molecules by using McPherson 218 monochromator. (Setup for generated tunable VUV laser beams including heat pipe oven is already given in figure 3-1, monochromator optical system setup is given in figure 3-7.)

3.5 Nitrogen discharge setup

3.5.1 Corona discharge setup

A corona discharge develops between two high-voltage electrodes in a neutral fluid, in our case gas, by ionizing that fluid so as to create a plasma around one electrode, and by using the ions generated in the plasma-processes as the charge carriers to the other electrode.

The corona discharge setup used in this experiment as illustrated in figure 3-12 has two electrodes: a hollow metal pipe was coated with a ceramic, and a filament was wound around the ceramic, hence electrically isolated from the inner electrode. The curved filament is shown as 1 in the figure 3-12 and the ceramic rod is shown as 2 in the figure 3-12. The filament was connected to high voltage (AC). The high potential gradient between the filament and the inner electrode is responsible for the generation of the plasma. With nitrogen gas flowing over the filament, and high voltage (about 3000 V AC) between filament and inner electrode applied, the corona discharge visibly gives out violet light. During the experiment, cold water flowing in the steel pipe (shown 3 in the figure 3-12) was used to stabilize the temperature. The steel

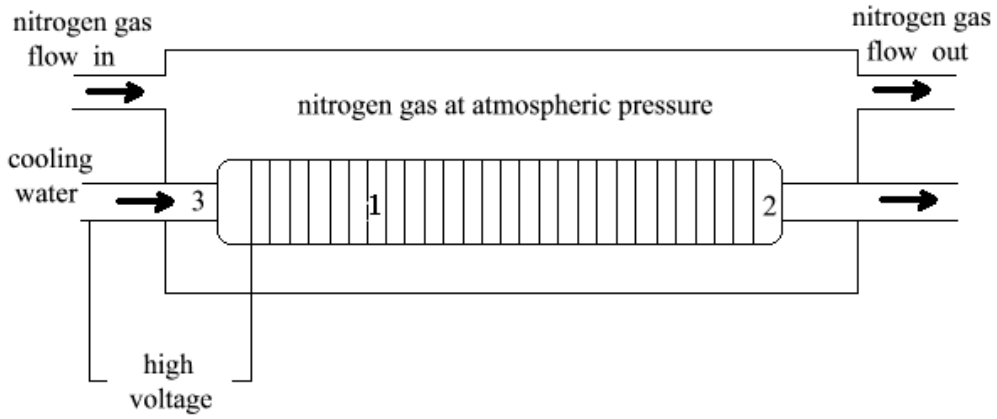

Figure 3-12: The corona discharge setup. The numbers indicate the filament (1), the ceramic rod (2), and the water cooled steel pipe (3).

pipe was the inner electrode and was connected to earth. In figure 3-13 a photo of the corona discharge setup is displayed.

A Bovan & TTP (c) 2002 power supply was used to supply high voltage to this corona discharge. This power supply is a resonant half-bridge design. The resonant elements consist pre-dominantly of the primary inductance L_1 and the load capacitance C_{L}. This HV (high voltage)-transformer supplies an output voltage of 3000 V at output frequency about 55 kHz without load. With the corona discharge as load, the output voltage drops to about 2500 V. The output voltage profiles are shown in figure 3-14, the open square profile and the solid profile indicate the voltage with and without load, respectively.

3.5.2 Microwave excited nitrogen plasma

Figure 3-15 shows the experimental setup of the microwave excitation of N_2 plasma. The glass tube of the electrodeless lamp (EDL) is evacuated by a mechanical pump (Balzers, 1390 u/min, ADEB 71 N 4 R3) to maintain a low pressure in the tube. By means of an A-antenna, the microwave power generator (Microtron 200) supplies 50 Watt incident power to EDL, the latter

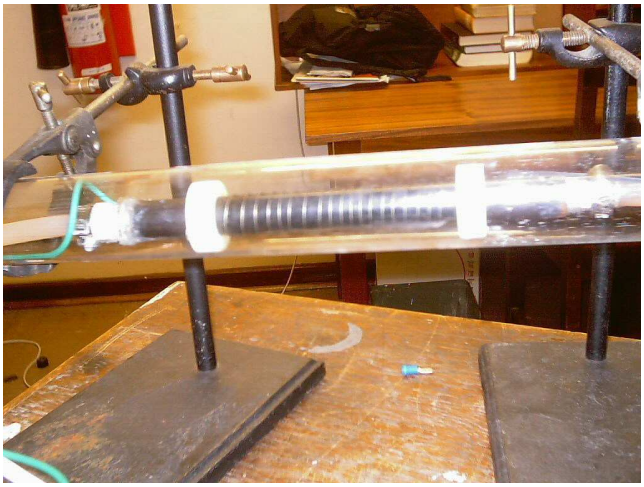

Figure 3-13: Photograph of corona discharge set-up.

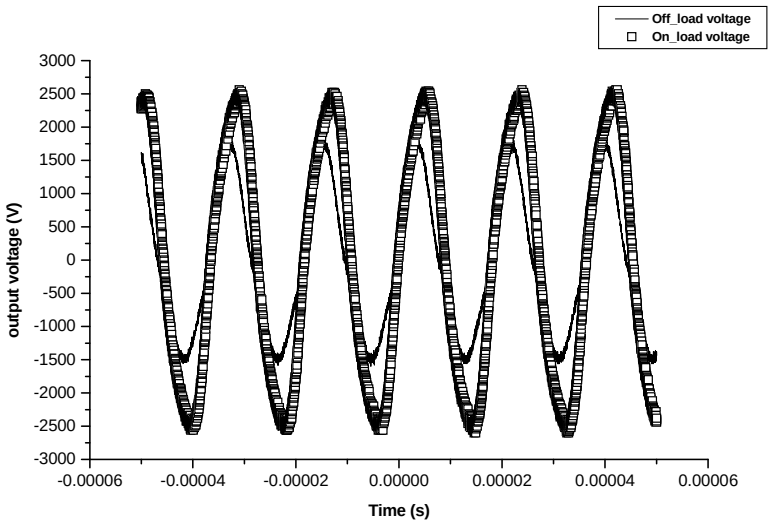

Figure 3-14: The Bovan & TTP (c) 2002 power supply output voltage profile. The solid profile shows the output voltage profile without load, and the open square profile shows the output voltage profile under the condition that the discharge is on.

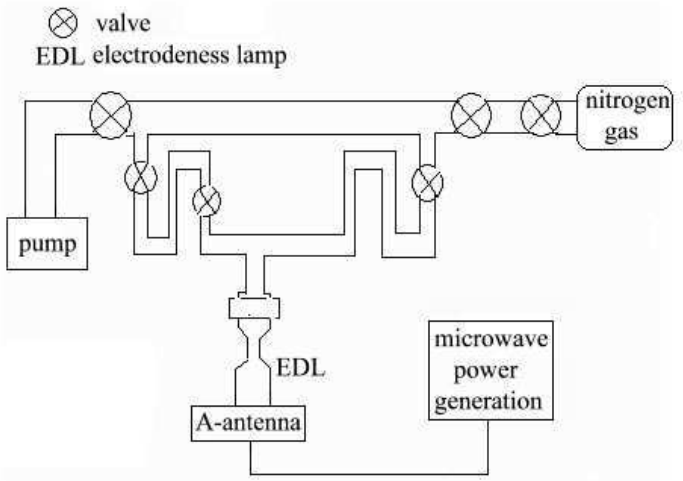

Figure 3-15: Experimental layout for the microwave excitation of the nitrogen plasma.

establishes the nitrogen plasma in its enclosed region.

3.6 Data acquisition

The diffracted light coming from the monochromator exit slit enters the photocathode inside the photomultiplier tube which converts energy of the incident light into photoelectrons. This conversion efficiency varies with the wavelength of the incident light. As the photon cathode is irradiated, photoelectrons are emitted into the vacuum where there is an electron multiplier and an electron collector (anode). These photoelectrons are collected by the anode as an output signal.

A personal computer is used to record these output signals during the experiment. Figure 3-16 shows the computerised system used for data acquisition in the experiment setup. The signal from a photodiade, onto which light pulses from dye laser I falls, triggers the SR 250 boxcar and the SR 245 analog-to-digital (A/D) converter (A/D). The position of the boxcar gate is very important for measuring short pulses, and in order to accurately set it up, an oscilloscope (Hewlett Packard 54616B) was used. The optimal boxcar position was determined

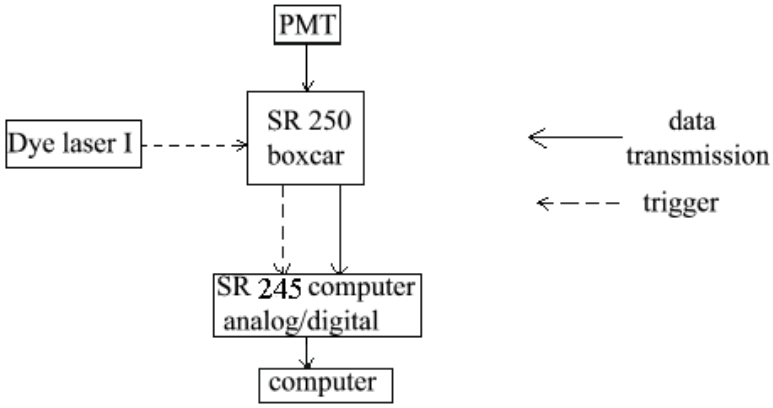

Figure 3-16: Schematic illustration of the computerised system used for instrument data acquisition in the experiment setup.

by adjusting the delay while observing measured signal. In the experiment, the signals recorded in the scan (monochromator grating scan or dye laser wavelength scan) were fed into the input ports of the SR 245 A/D converter, via a boxcar integrator. The value of the signals obtained in each scan were transferred as a matrix to the computer. The trace shown on the computer screen was stored as an ASCII file in the computer.

Chapter 4

Characterization of instrumentation

4.1 Monochromator characterization

In order to effectively use the monochromators, it is necessary to characterize them and ensure that they are properly set up. A mercury lamp and a nitrogen discharge were used for initial wavelength calibration of the monochromators. Monochromatic light supplied by a dye laser, was used in the experiments to ensure that the monochromators were set up for optimal resolution.

4.1.1 Wavelength calibration of the McPherson 225 monochromator

4.1.1.1 Determining wavelength calibration and resolution using a mercury lamp

UV light emitted by a mercury lamp enters the monochromator through entrance slit and is diffracted by the concave grating, and was recorded by a photomultiplier tube (PMT) (Hamamatsu R761, 1500 V high voltage) at the exit slit (in the experiment entrance slit was 0.03 mm, exit slit was 0.01 mm). This signal was amplified by a current amplifier and recorded with an AD card. This PMT detects wavelength in the range from 185 nm to 850 nm. A typical experimental spectrum of a mercury lamp is shown in figure 4-1 (wavelength region is from 200 nm to 300 nm).

The peaks in the recorded mercury spectrum were identified by comparing them to standard mercury wavelength from literature [[3], page 520]. The data is summarized in table 4.1. Four

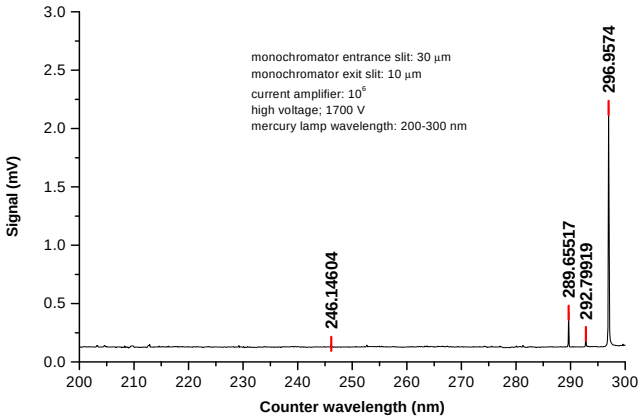

Figure 4-1: The spectrum obtained by using mercury lamp as source.

Standard wavelength (nm)	Counter wavelength (nm)
246.41	246.15
289.36	289.66
292.54	292.80
296.76	296.96

Table 4.1: Table of the standard wavelength and the measured (counter) wavelength obtained in the experiment.

peak wavelengths of the mercury lamp in this experiment were used to do wavelength calibration of the monochromator in the UV region. The calibration function is shown in figure 4-2.

Figure 4-3 shows the measured linewidth of the transition is 0.087 nm at wavelength 296.95 nm. Compared to the specified resolution of 0.015 nm, the experimental measured linewidth of 0.087 nm is 5.8 times the resolution.

4.1.1.2 Wavelength calibration using nitrogen emission spectra

(a) **Emission spectrum of Nitrogen corona discharge**

The spectrum shown in figure 4-4 emitted by nitrogen in a corona discharge was obtained with the monochromator entrance slit 0.1 mm, exit slit 0.07 mm, and PMT high voltage 1500 V. This distinctive spectrum (peaks are distinguished by i and ii in table 4.2), was used to calibrate the wavelength and determine transition constants.

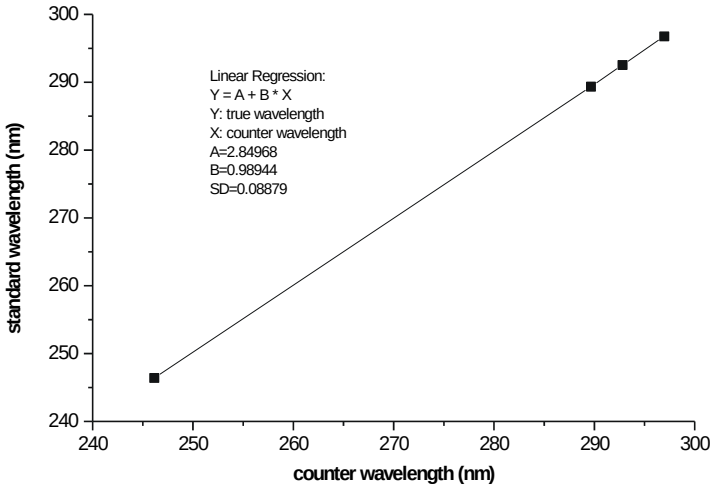

Figure 4-2: Plot of the counter wavelength vs. the measured data for the mercury lamp used for wavelength calibration, and the calibration function obtained by the linear fit.

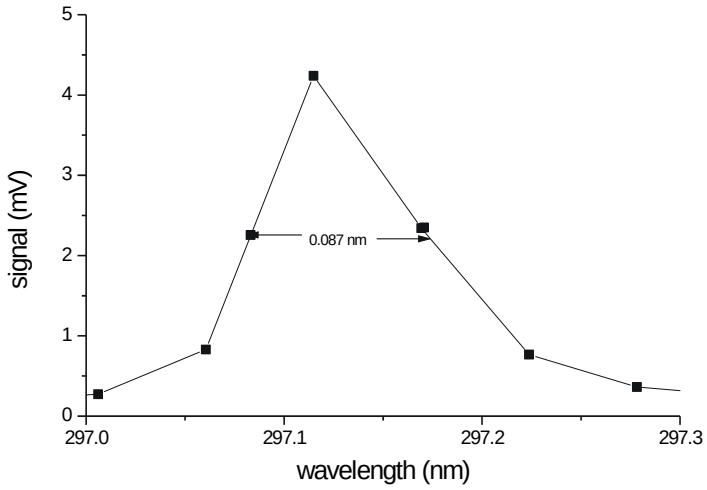

Figure 4-3: Linewidth of mercury line at 296.95 nm of 0.087 nm was obtained during the experiment.

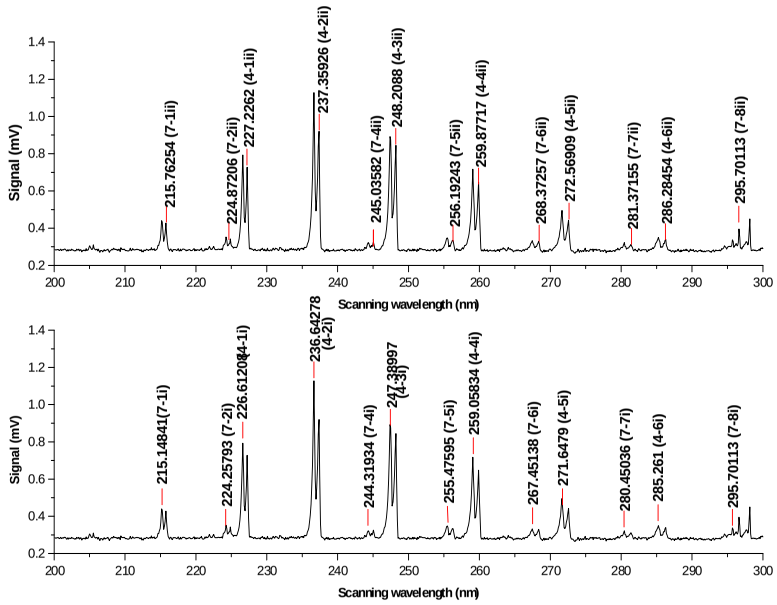

Figure 4-4: Nitrogen corona discharge spectrum in wavelength region from 200 nm to 300 nm. Two spectra are shown in order to label closely spaced lines as tabled in table 4.2 belonging to two R branches: i the stronger (below) and ii the weaker branch (top).

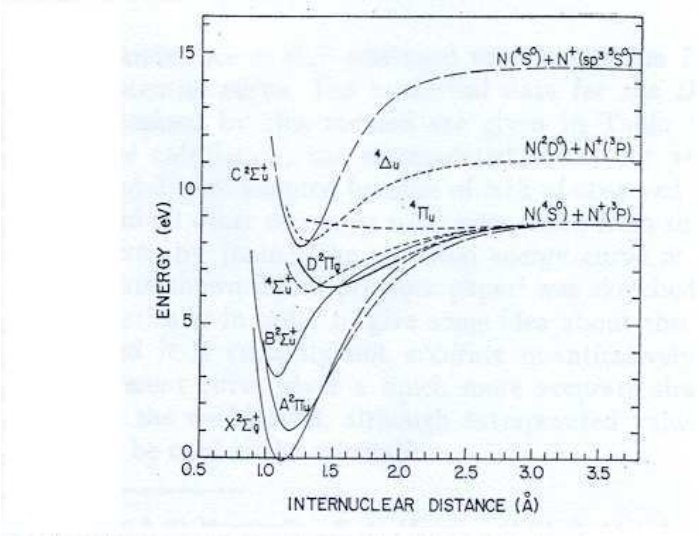

Figure 4-5: N_2^+ potential energy curves taken from the literature [7].

The transition in the nitrogen spectrum were identified as transitions belonging to transitions $D^2\Pi_g - A^2\Pi_u$ of $\left(N_2^{14}\right)^+$ that have been reported by [6] and [7] (here it is called standard spectrum). The potential energy curves of the electronic states of N_2^+ are shown in figure 4-5.

Assuming this identification, table 4.2 lists counter wavelength and standard wavelength from literature [6]. Additional peaks were identified belonging to the same sub-band, and using the corresponding vibrational constants $(\omega_e, \omega_e x_e, \omega_e y_e)$ and the electric wave numbers from literature [6] the standard wavelengths were calculated by means of equation 2.77 (neglecting rotation wave number) and equation 2.78 and were labeled with an asterisks in table 4.2. Figure 4-6 shows the calibration function in terms of the standard wavelength and counter wavelength.

In order to test this assignment, the vibrational constants of both states A and D of $\left(N_2^{14}\right)^+$ were calculated. The wave number separation $\Delta\upsilon\left(n''\right)$ of the successive lines starting at the same upper vibrational level can be used to calculate the vibrational constants of the lower electronic state. According to equation 2.78 (neglecting cubic terms), the separation of successive bands (in cm^{-1}) (equal to the separation of successive levels n'' and $n''-1$) can be obtained from:

$$\Delta\upsilon\left(n''\right) = \omega_e'' - 2\omega_e'' x_e'' - 2\omega_e'' x_e'' n''.$$

Counter wavelength (nm)	Standard wavelength (nm)	Transition ($n' - n''$)
215.14841	215.03	7-1i
215.76254	215.29	7-1ii
224.25793	223.9	7-2i
224.87206	224.19	7-2ii
226.61208	226.22061*	4-1i
227.2262	226.5168*	4-1ii
236.64278	236.05	4-2i
237.35926	236.38	4-2ii
244.31934	243.52096*	7-4i
245.03582	243.86421*	7-4ii
247.38997	246.63	4-3i
248.2088	246.97	4-3ii
255.47595	254.41	7-5i
256.19243	254.76	7-5ii
259.05834	257.94	4-4i
259.87717	258.34	4-4ii
267.45138	266.05	7-6i
268.37257	266.46	7-6ii
271.6479	270.18851*	4-5i
272.56909	270.61112*	4-5ii
280.45036	278.60621*	7-7i
281.37155	279.05564*	7-7ii
285.261	283.38694*	4-6i
286.28454	283.85192*	4-6ii
295.70113	292.15	7-8i
296.62231	292.65	7-8ii

Table 4.2: Table comparing standard wavelength with counter wavelength. It shows standard wavelengths match counter wavelength well in shorter wavelength region (wavelength shorter than 240 nm), however in longer wavelength region the counter wavelength does not match standard wavelength well because of counter wavelength shifting.

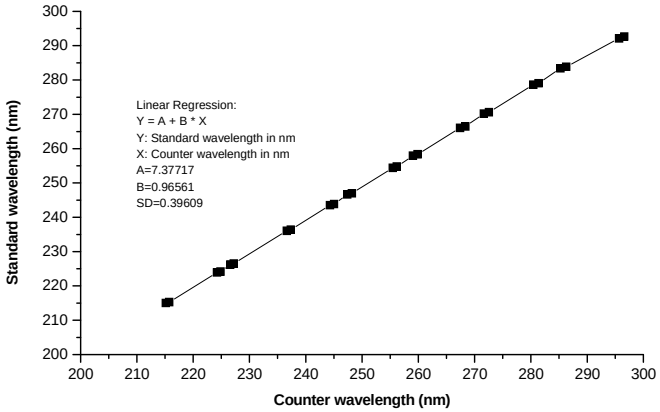

Figure 4-6: Plot of the standard wavelength vs. the counter values for the corona nitrogen discharge used for wavelength calibration and the calibration function obtained by the linear fit.

State A of $\left(N_2^{14}\right)^+$	ω_e	$\omega_e x_e$
Calibration values	1933.76	14.04
Standard values	1903.53	15.011
State D of $\left(N_2^{14}\right)^+$		
Calibration values	913.95	11.27
Standard values	911.7	12.606

Table 4.3: The vibrational constants of both states A and D of $\left(N_2^{14}\right)^+$ in units of cm^{-1}.

Using this equation, the vibrational constants of the lower state A of $\left(N_2^{14}\right)^+$ can be calculated from stronger peaks (labeled with i) in the experimental data. Average values of these constants are shown in table 4.3, and compared to standard values obtained from literature [21].

Using equation 2.80, and the results obtained for the lower electronic state the vibrational constants of the upper state D of $\left(N_2^{14}\right)^+$ were calculated, the results are also listed in table 4.3. The electronic transition wave number Δv_e used in the calibration comes from [6].

The standard values in table 4.3 correspond to the band head whereas the calibration values correspond to the rotational transition with highest intensity in the experimental spectra, explaining slight difference between the experimental data and standard data.

In the experimental spectrum, it is clearly visible that the individual bands are composed

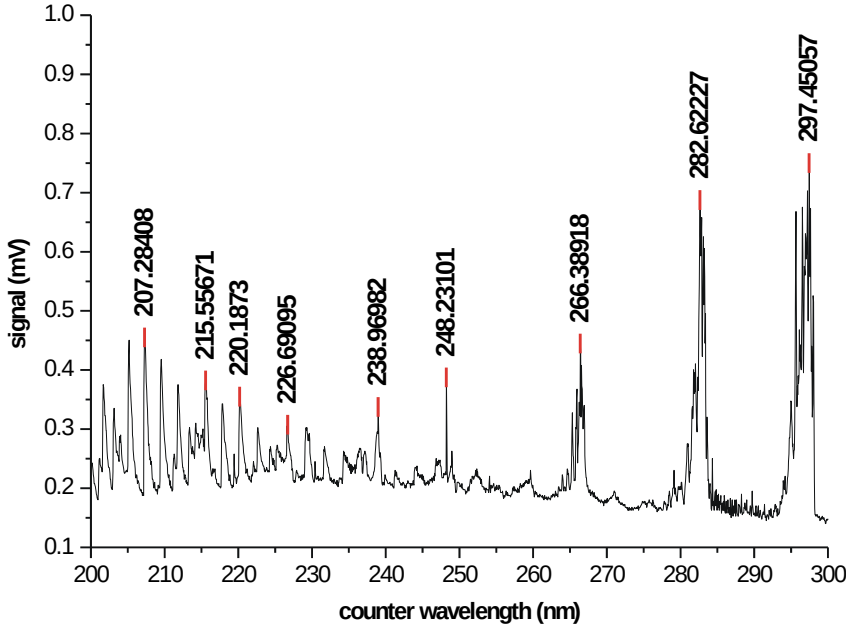

Figure 4-7: The nitrogen microwave plasma spectrum.

of two heads distinguished by i and ii in table 4.2. Both heads are formed by the R branches of sub-bands in transition of $D^2\Pi_g - A^2\Pi_u$ of $\left(N_2^{14}\right)^+$ as referred to in the literature ([6] and [7]). This phenomena was discussed in section 2.2.3. The branch ii-band head was calculated in the literature. In this experiment the highest intensity lines of this branch was recorded and differs from the calculated value of band head from the literature by approximately 40 cm^{-1}.

In this experiment the prominent appearance of the $n' = 4$ band in the spectrum generated by the corona discharge suggests that this may be due to a selective excitation as suggested in a similar case in the literature [23], or due to superposition of band systems [6].

(b) **Emission spectrum of Nitrogen in a microwave discharge**

The spectrum of the microwave excited nitrogen plasma is shown in figure 4-7 (spectrum obtained under the conditions: entrance slit and exit slit 0.01 mm; current amplifier 10^6, high voltage 1.7 kV, and wavelength scanned in the experiment from 200 nm to 300 nm). Using the wavelength from the literature [5], the N_2 bands were identified and summarized in table 4.4.

A detailed wavelength scan of selected wavelength regions showed rotational spectra of $p'(0) - a^1\pi_g(0)$ and $C^3\pi_u(2) - B^3\pi_g(0)$ (the numbers in brackets indicating the vibrational

Counter wavelength(nm)	Individual band system
207.28408	207.73 $(y^1\pi_g\,(1) - a'^1\Sigma_u^-\,(0))$
215.55671	215.36 $(y^1\pi_g\,(0) - a'^1\Sigma_u^-\,(0))$
220.1873	219.89 $(x^1\Sigma_g^-\,(1) - a'^1\Sigma_u^-\,(0))$
226.69095	226.34 $(y^1\pi_g\,(1) - w^1\Delta_u\,(0))$
238.96982	238.76 $(a^1\pi_g(9) - X^1\Sigma_g^+(20))$
248.23101	248.17 $(a^1\pi_g(14) - X^1\Sigma_g^+(25))$
266.38918	266.05 $(D^3\Sigma_u^+(0) - B^3\pi_g(4))$
282.62227	282.71 $(p'(0) - a^1\pi_g(0))$
297.45057	297.68 $(C^3\pi_u(2) - B^3\pi_g(0))$

Table 4.4: Table used to compare nitrogen microwave experimental wavelength with standard wavelength from the list.

state) as shown in figures 4-8 and 4-9 respectively. Using equation 2.77, 2.78, and 2.79, these rotational peaks were identified, and results of the identification are tabled in table 4.5 and table 4.6. The constants used in these equations were obtained from literature [1].

It is interesting to note that the emission spectrum figure 4-4 of the corona discharge is due to molecular ions of nitrogen; and the emission spectrum figure 4-7 of the microwave discharge is due to molecular nitrogen.

4.2 The VUV laser beam

Tunable narrow bandwidth lasers have been successfully used as sources of radiation in high-sensitivity high-resolution spectroscopy since the development of lasers in early 1960s. Four-wave mixing generated in two-component gaseous non-linear medium can supply narrow bandwidth (typically of the order of 0.1 cm^{-1}) tunable coherent light in VUV [17].

For a tunable laser in VUV, it is important to choose an available gaseous medium and to find the best experimental conditions to yield optimal VUV output in the required wavelength region. It has been reported in [20], [18], and [19] that sum-frequency generation in Mg vapor is an efficient source of narrow bandwidth vacuum ultra-violet radiation for high resolution excitation spectroscopy of molecules in the spectral range $140 - 160$ nm.

Counter wavelength (nm)	Rotation transition band
280.58201	$R(24)$
280.84656	$Q(28)$
281.00529	$R(21)$
281.14286	$R(20)$
281.22751	$Q(25)$
281.36508	$R(18)$
281.59788	$R(16)/P(29)$
281.68254	$R(15)/Q(21)$
281.75661	$Q(20)$
281.89418	$R(13)$
281.95767	$Q(18)$
282.03175	$Q(17)$
282.10582	$Q(16)$
282.17989	$Q(15)/P(23)$
282.24339	$P(22)$
282.37037	$R(7)$
282.42328	$R(6)$
282.50794	$P(18)$
282.55026	$R(4)/P(17)$
282.62434	$R(2)/Q(7)$

Table 4.5: Rotation spectrum of the transition of $p'(0) - a^1\pi_g(0)$ of molecular nitrogen excited in a microwave discharge.

Counter wavelength (nm)	Rotation transition band
296.38095	$R(19)$
296.73016	$Q(23)$
296.87831	$Q(21)$
296.97354	$R(12)$
297.01587	$Q(19)$
297.07937	$Q(18)$
297.13228	$Q(17)$
297.19577	$Q(16)$
297.30159	$R(7)$
297.39683	$Q(12)$
297.50265	$Q(9)$
297.67196	$P(18)$
297.77778	$P(13)$

Table 4.6: Rotation spectrum of the transition of $C^3\pi_u(2) - B^3\pi_g(0)$ of molecular nitrogen excited in a microwave discharge.

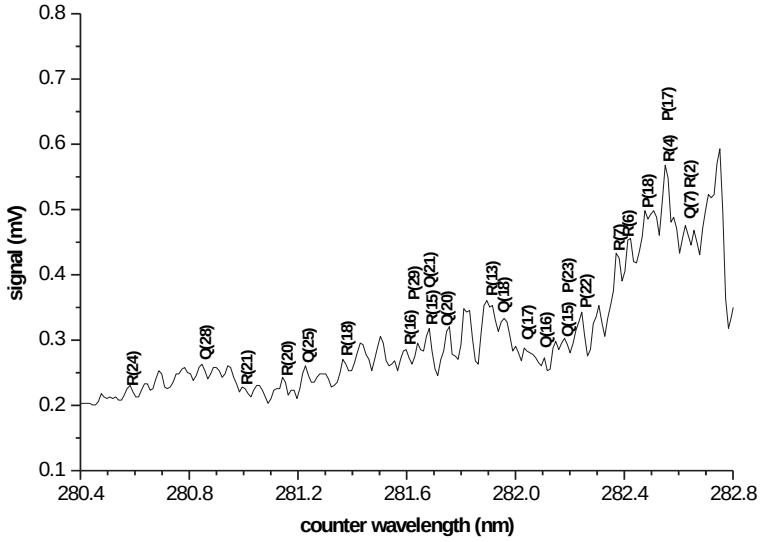

Figure 4-8: Rotational spectrum of nitrogen plasma of the transition of $p'(0) \rightarrow a'\pi_g(0)$.

4.2.1 Setting up the McPherson 218 monochromator for the visible

The experimental setup for measuring the McPherson 218 monochromator bandpass is shown in figure 4-10.

A Lambda Physik EMG 203 MSC XeCl excimer laser pumps one Lambda Physik FL 3001X dye laser (LC 4400, with Coumarine 120 dissolved in methanol 205 as dye). This dye laser tuned to 440 nm was used as monochromatic light source in this experiment, and can be assumed to be monochromatic compared to the bandpass of the monochromator. A part of beam is split off by a partial reflector towards the monochromator entrance slit center. The beam, which passes through the monochromator's optical system, is detected by a photomultiplier (R761, supplied 1.5 kV, detecting wavelength range 185 nm to 850 nm). Figure 4-11 shows a spectrum as recorded with an entrance slit of 0.07 mm and exit slit of 0.05 mm. By choosing the maximum signal height between H_1 and H_2, the FWHM of 0.06 nm was obtained. This shows the monochromator is properly set up since the theoretical bandpass for the monochromator is calculated using equation 2.108 as 0.06 nm.

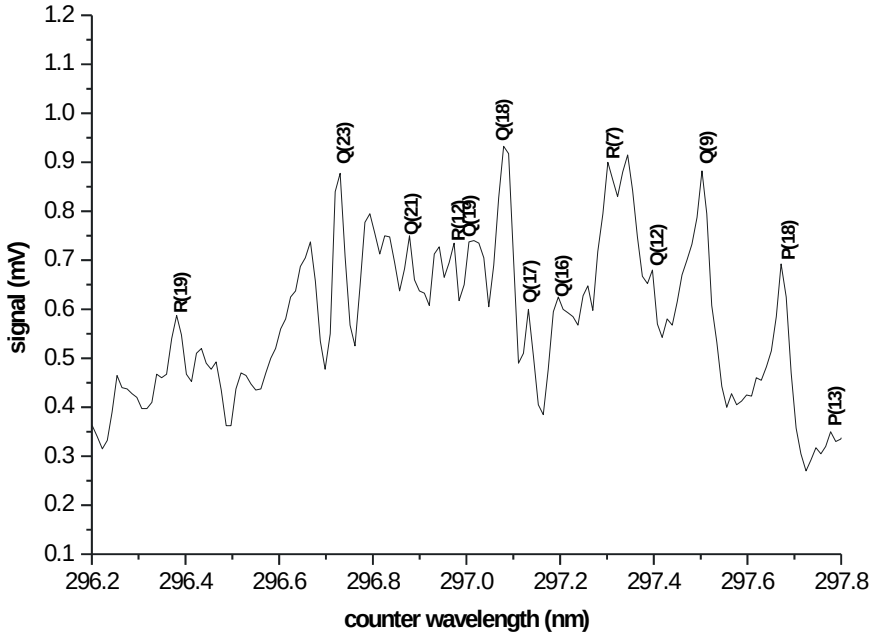

Figure 4-9: Rotation nitrogen in a microwave plasma spectrum of the transition of $C^3\pi_u\,(2) \rightarrow B^3\pi_g\,(0)$.

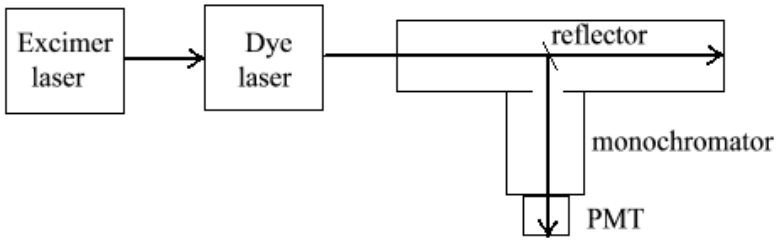

Figure 4-10: Experimental setup for McPherson 218 monochromator.

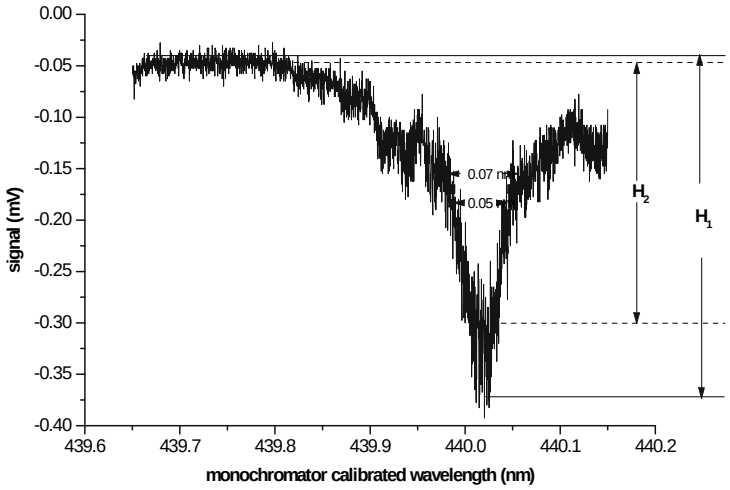

Figure 4-11: Dye laser spectrum obtained in the experiment using McPherson 218 monochromator. The linewidth of the monochromatic light from the laser at 440 nm is 0.06 nm.

4.2.2 Setting up the McPherson 218 monochromator for the VUV

Setting up the monochromator system experimentally was done by using monochromatic light of the dye laser at 440 nm. However, this monochromator slit width has to be optimized again in the VUV to obtain strong enough signal because the tunable VUV laser energy is $1,000,000$ times less than the dye laser energy used in previous section.

In order to set up the monochromator system in the VUV, third-harmonic generation in Mg was chosen as VUV source. Dye laser I, which was pumped by an excimer laser with energy 159 mJ, was tuned to the two-photo resonance of Mg at 430.88 nm giving VUV output at 143.6 nm. The Ar pressure in the vertical heat-pipe was set at 24.5 kPa providing stable temperature of 760° C inside the heat-pipe oven. The krypton pressure inside the horizontal heat-pipe was adjusted to around 24 kPa for optimized phase-matching.

During the experiment the exit slit was changed while keeping the entrance slit constant at 0.4 mm. Two experimental scans over the VUV source are shown in figure 4-12. Both were obtained with an entrance slit of 0.4 mm. The exit slit was 0.2 mm for the spectrum shown in dashed line in the figure and 0.25 mm for the spectrum shown in solid line in the figure. It is very clear from figure 4-12 that they have similar linewidth, but the signal obtained using exit slit 0.25 mm is stronger than the signal obtained using exit slit 0.2 mm. Therefore the

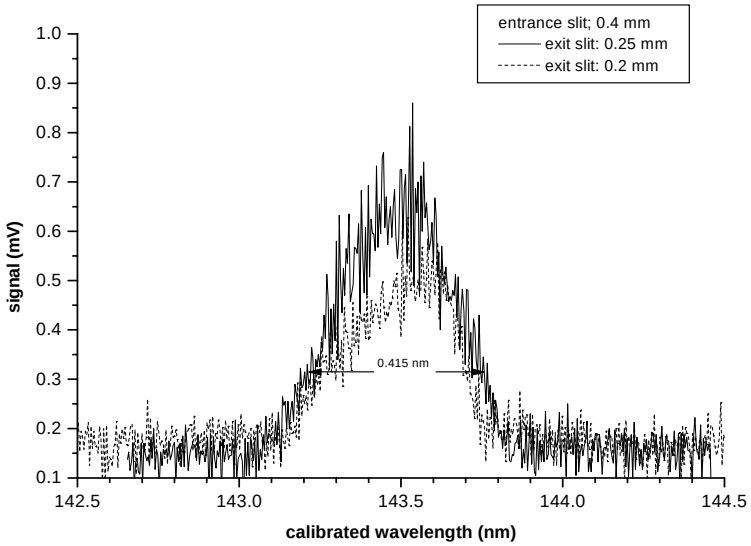

Figure 4-12: Spectra illustrating the slit width dependence of the signal strength.

monochromator slit widths for use in VUV are: entrance slit width 0.4 mm, exit slit width 0.25 mm. This recorded a linewidth of about 0.42 nm. The bandpass of this setup is approximately 0.3 nm.

4.2.3 Spectral analysis of VUV output

One of the new facilities available to the experimental setup is the fact that the monochromator can be used to evaluate the VUV generated in the heat-pipe, which was previously not possible. To illustrate the value of this additional diagnostic tool, the experiment was set up to measure the VUV generated in the heat-pipe. The conditions for the heat-pipe were: the pressure of the outer argon gas about 24.5 kPa giving a stable temperature of the sodium inside the heat-pipe oven of about 760°C; the external krypton pressure was around 25 kPa for approximate phase-matching. Excimer pump laser with energy about 160 mJ pumping dye laser I producing pulse energy 0.51 mJ and dye laser II with energy 1.4 mJ. Dye laser I wavelength was fixed on the two-photon resonance at 430.88 nm; dye laser II wavelength was tuned in region 441 nm - 443 nm, which is the wavelength region of interest for LIF spectroscopy of the $A^1\Pi\,(3) - X^1\Sigma^+$

(0) transition in CO. Three measurements were performed without adjusting the Kr pressure for phase-matching. In every measurement, dye laser II was tuned to one desired wavelength, for instance 441 nm for the first measurement, 442 nm for the second measurement, and 443 nm for the third measurement, and the monochromator was used to record the VUV output spectrum of the heat-pipe. The experimental results are shown in figure 4-13.

From figure 4-13 it is clear that the third-harmonic of dye laser I is generated in every case, and in each case sum-frequency generation can be detected. From figure 4-13 it is clear that the third-harmonic intensity is the same in all three measurements while sum-frequency generation decreases as dye laser II was tuned to longer wavelengths. The possible reason for the decreasing sum-frequency signal are: (i) Lack of proper phase-matching. No phase-matching adjustments were done when changing to different wavelengths. (ii) Dye laser II pulse energy may be decreasing, since the energy of the pulses were not recorded for each new wavelength, and, according to equation 2.54 in section 2.1.6, dye laser energy affects VUV intensity. (iii) It may be due to absorption in the Mg heat-pipe in this region.

The exact polarization of the two beams must be ideal for sum-frequency generation. The polarization of the two laser beams should ideally be linearly polarized perpendicularly, and combined to be transformed to right- and left-circular polarization by a quarter wave plate, to discriminate against the third-harmonic generation. The fact that in every case some third-harmonic is present, clearly indicates that the polarization is not perfect.

The setup was then used to characterize the tunable VUV laser output, and the influence of the following factors could be determined: the phase-matching, the laser energy, the wavelength of dye laser II and the polarization and collinear alignment of the laser beams.

4.2.4 Phase-matching

To optimize the VUV generation, proper phase-matching must be done. This was illustrated in two types of experiments. In the first experiment the tunable dye laser (dye laser II) was set at one wavelength (different from dye laser I tuned to two-photon resonance), and a spectrum was taken by scanning the monochromator over the third-harmonic and the sum frequency wavelengths for a given krypton pressure. The peak intensities were plotted versus the external krypton pressure. In the second experiment the monochromator was fixed to the sum-frequency

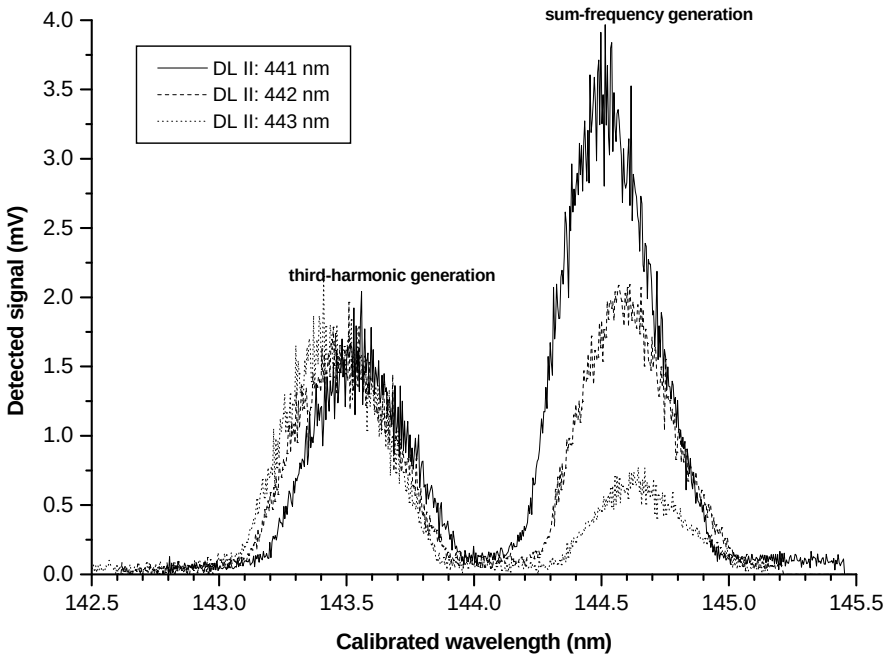

Figure 4-13: Spectrum of the typical output of the VUV source.

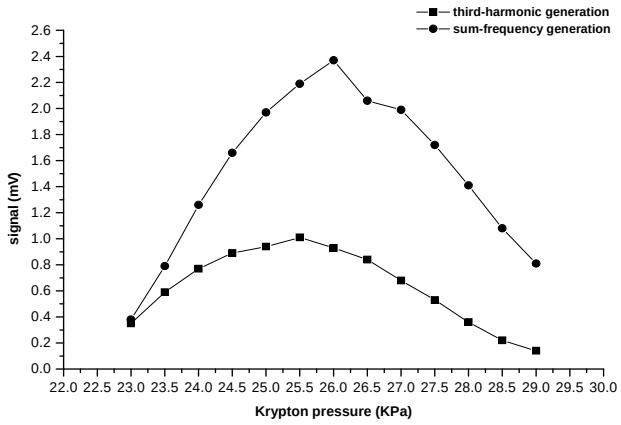

Figure 4-14: Effect of phase-matching on output signal as tunable dye laser wavelength was set on 441 nm.

wavelength, and the external krypton pressure was changed and the intensity was recorded.

The first set of experiments was done with excimer laser with energy 170 mJ running at 5 Hz repetition rate, pumping the two dye lasers. Dye laser energies were 0.8 mJ and 1.35 mJ for dye laser I and II respectively (dye laser energy was measured at wavelength 440 nm). Dye laser I wavelength was fixed at 430.88 nm, dye laser II wavelength was tuned from 441 nm to 443 nm in steps of 1 nm for the different sets of measurements. In every set, dye laser II was set on one desired wavelength (either 441 nm, or 442 nm or 443 nm for the different sets), and the external krypton pressure was changed in steps of 0.5 kPa. For every setting the monochromator was scanned over the relevant wavelength region and the peak intensities recorded. Using this method, three sets of measurements were obtained, one for each dye laser II wavelength chosen. The experimental results are shown in figures 4-14, 4-15 and 4-16. The experimental results in these figures show that phase-matching is achieved around $24 - 28$ kPa for both third-harmonic and sum-frequency generation, and the optimal pressures can clearly be identified in all cases. For this particular choice of wavelengths the sum-frequency generation is stronger than third-harmonic generation for dye laser II wavelength 441 and 442 nm, but the third-harmonic was not eliminated completely as could have been expected from the choice of polarizations. For the dye laser II wavelength set at 443 nm, the sum-frequency generation is

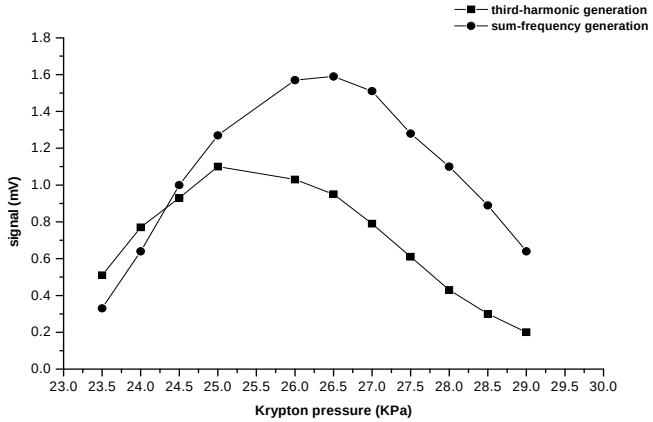

Figure 4-15: Effect of phase-matching on output signal as tunable dye laser wavelength was set on 442 nm.

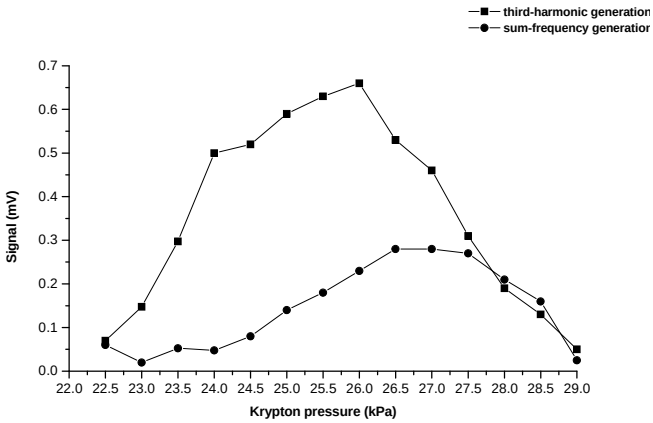

Figure 4-16: Effect of phase-matching on output signal as tunable dye laser wavelength was set on 443 nm.

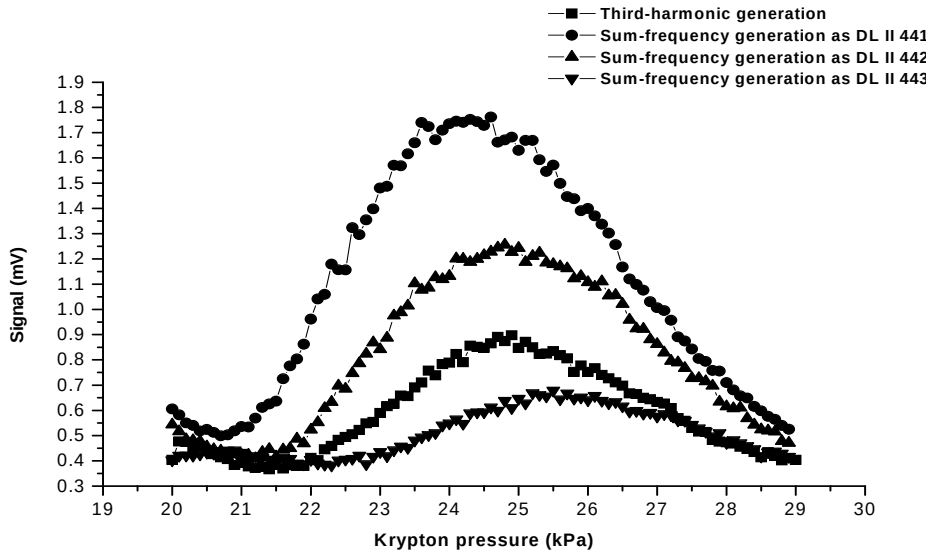

Figure 4-17: Phase-matching obtained for sum-frequency generation for different dye laser II wavelengths.

weaker than third-harmonic generation. The general trend seems to be that the sum-frequency intensity decreases with longer dye laser II wavelength in this particular wavelength region. This was also mentioned in section 4.2.3. The results described in the current section clearly show this decrease was not due to the lack of phase-matching, but due to something else.

In order to get further insight into the phase-matching a second type of experiment was done. As mentioned above, in this experiment, Dye laser I wavelength was fixed 430.88 nm; dye laser II wavelength was tuned from 441 nm to 443 nm in 1 nm steps. For every chosen wavelength the monochromator was set to the corresponding sum-frequency wavelength, and external krypton pressure was changed from 20 kPa to 29 kPa in steps of 0.1 kPa. In addition the phase-matching for the third-harmonic wavelength was also recorded. For the experiments the excimer laser energy was 170 mJ, pumping two dye lasers giving out pulse energy 0.36 mJ and 1.06 mJ for dye laser I and II respectively.

Figure 4-17 shows the experimental result. It shows that phase-matching condition for sum-frequency generation shifts to higher krypton pressure with longer tunable laser wavelength.

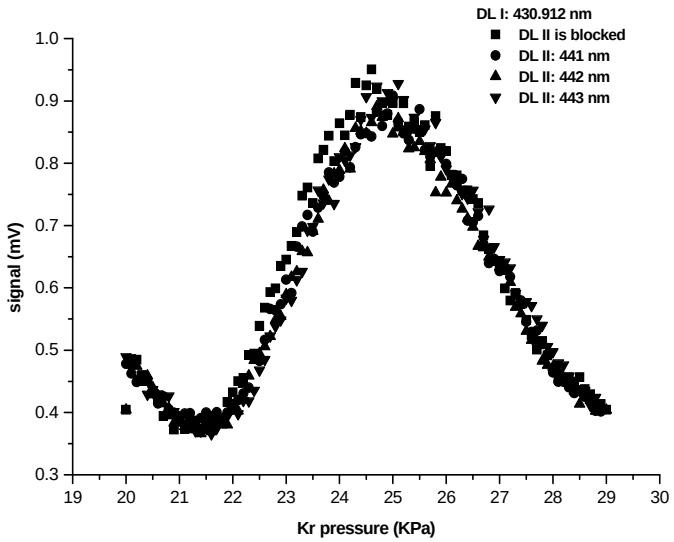

Figure 4-18: Phase-matching obtained for third-harmonic generation for different conditions.

The phase-matching is achieved over a reasonably wide pressure region, which is desirable for spectroscopy, since approximate phase-matching can be achieved without constantly (simultaneously) re-adjusting the pressure while scanning over a wavelength region. Once again the third-harmonic generation is weaker than sum-frequency generation as tunable dye laser wavelength was 441 nm and 442 nm, but stronger than sum-frequency generation for dye laser II wavelength 443 nm.

Phase-matching was also done for the third-harmonic generation with the non-resonant dye laser blocked, or unblocked and tuned to wavelength 441 nm, 442 nm, and 443 nm respectively. The result is shown in figure 4-18. From this result it is clear that the third-harmonic process is independent of the sum-frequency process as would be expected in the small signal limit.

Both methods have shown that phase-matching can be obtained for the krypton pressure in the region of 25 kPa $\pm$3 kPa. Phase-matching was therefore achieved by adjusting the krypton pressure as expected, as was discussed in section 2.1.9 (see equation 2.75).

4.2.5 Effect of laser energy attenuation

The influence of laser energy on the VUV generated was also investigated. In order to ensure alignment of the laser beams at all times, glass plates were placed in the laser beam to decrease one dye laser energy while keeping the other dye laser energy constant using the same excimer laser pump energy. By using different number of glass plates, the laser output of the dye lasers was measured.

Phase-matching was done for the sum-frequency generated for various dye laser energies. The experimental results are shown in figures 4-19, 4-20, and 4-21. In every figure, the spectra on the left were obtained by decreasing dye laser I energy while the spectra on the right were obtained by reducing dye laser II energy.

From the figures it is evident that dye laser I energy influences the tunable VUV generated non-linearly, as could be expected from theory. The energy of the generated VUV increases linearly with dye laser II energy.

4.2.6 Tuning dye laser II wavelength

To illustrate the tunability of the generated VUV laser source the sum-frequency generated was measured using one dye (with Coumarine 120) in dye laser II and tuning the laser over the range of the dye.

In the experiment dye laser II was tuned from wavelength 436 nm to 460 nm in steps of 1 nm. For every selected dye laser II wavelength the monochromator was set to record the VUV output. Dye laser with Coumarine 120 dissolved in methanol 205, pumped by excimer laser can be tuned from 423 nm to 462 nm. In the region between 423 nm and 436 nm, the sum-frequency and third-harmonic (dye laser I wavelength 430.88 nm) generation peaks are too close to be resolved using the monochromator, hence the wavelength region was omitted. For dye laser II in wavelength $460 - 462$ nm region the sum-frequency signal was too weak to be detected. For every different wavelength measurement, (i) approximate phase-matching was done by slowly adjusting external krypton pressure around 26 kPa (ii) dye laser II energy was measured. The experimental results are shown in figure 4-22, by plotting the VUV sum-frequency and third-harmonic signals versus the dye laser II wavelength. The wavelength region 441 nm to 443 nm shown by a dashed line in the figure was selected in the previous experiments

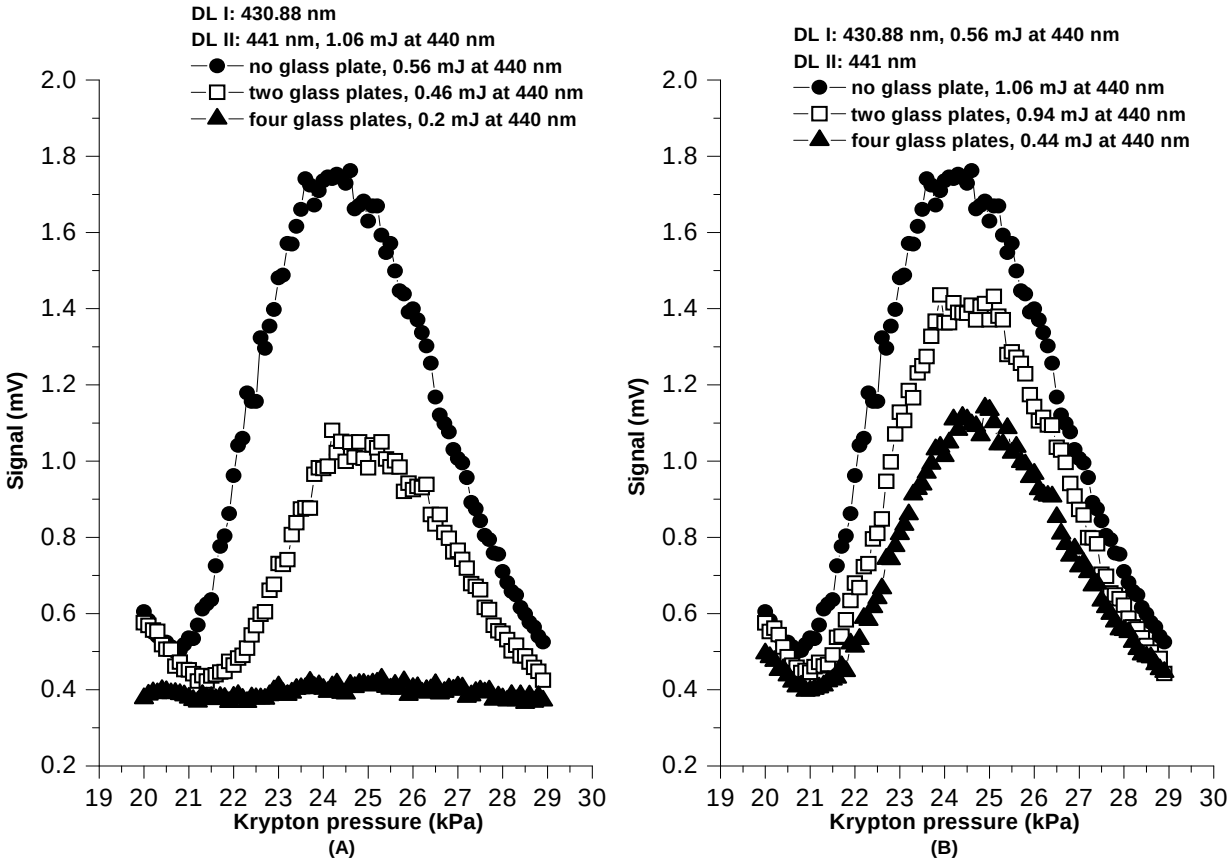

Figure 4-19: Phase-matching curves were used to illustrate the effect of laser energy on the phase-matching conditions for tunable dye laser wavelength 441 nm. (A) Spectrum was obtained for the condition that dye laser I energy was decreased while dye laser II energy was a constant, and (B) Spectrum was obtained for the condition that dye laser II energy was decreased as dye laser I energy was kept constant.

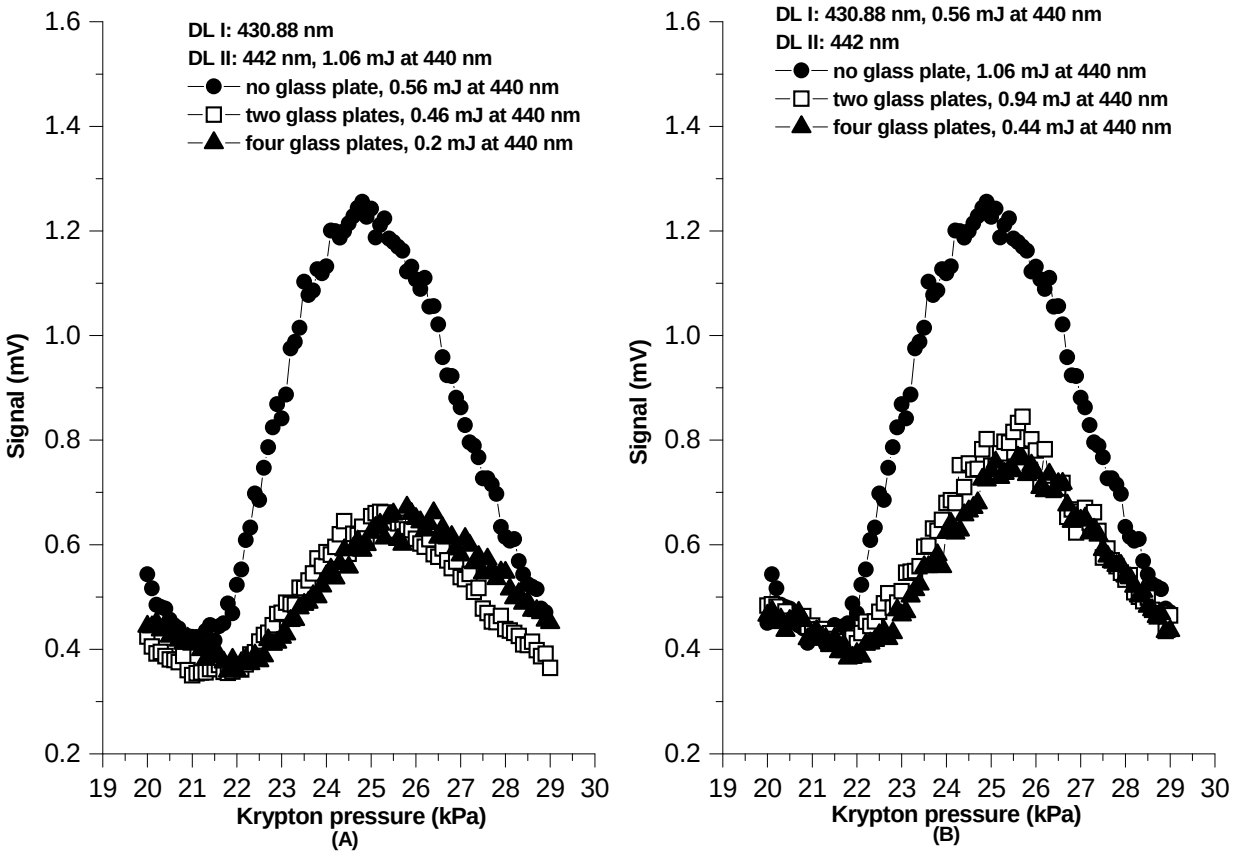

Figure 4-20: Phase-matching curves were used to illustrate the effect of laser energy on the phase-matching conditions for tunable dye laser wavelength 442 nm. (A) Spectrum was obtained for the condition that dye laser I energy was decreased while dye laser II energy was a constant, and (B) Spectrum was obtained for the condition that dye laser II energy was decreased as dye laser I energy was kept constant.

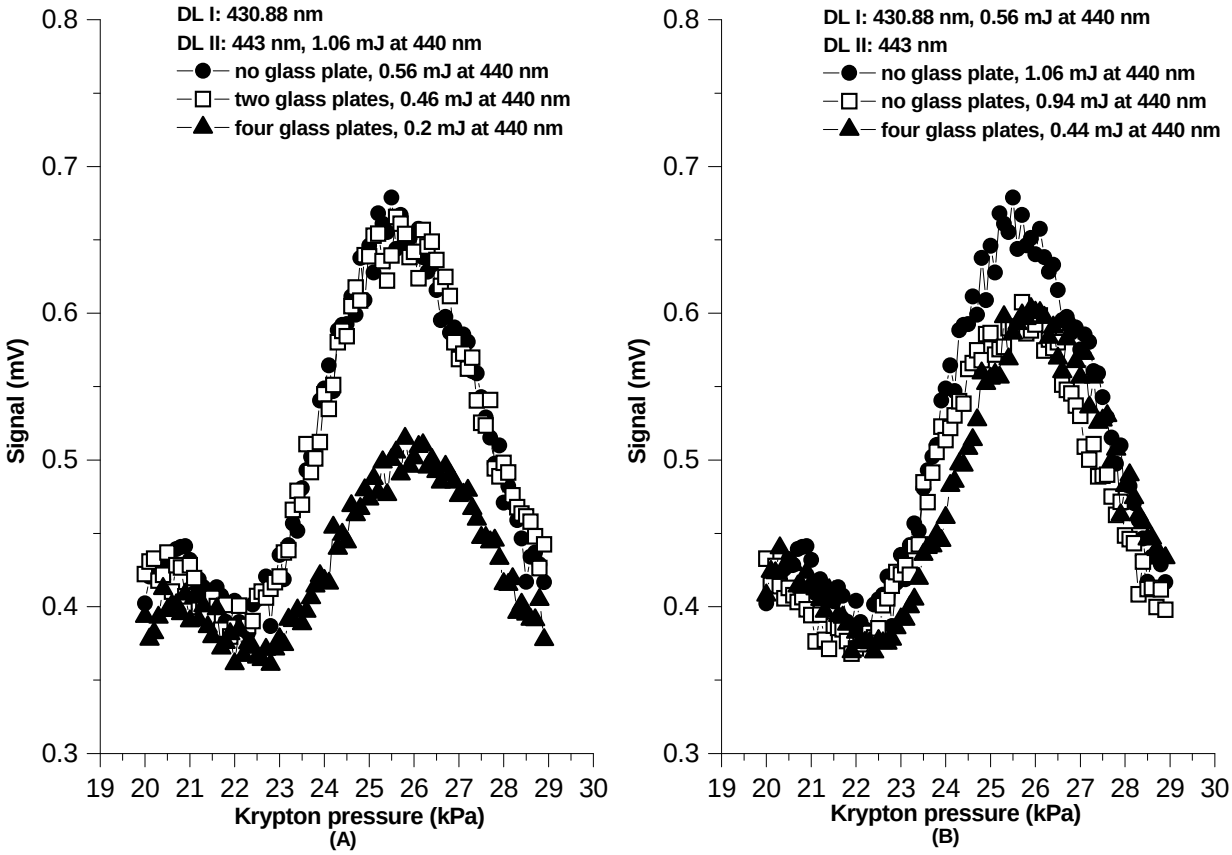

Figure 4-21: Phase-matching curves were used to illustrate the effect of laser energy on the phase-matching conditions for tunable dye laser wavelength 443 nm. (A) Spectrum was obtained for the condition that dye laser I energy was decreased while dye laser II energy was a constant, and (B) Spectrum was obtained for the condition that dye laser II energy was decreased as dye laser I energy was kept constant.

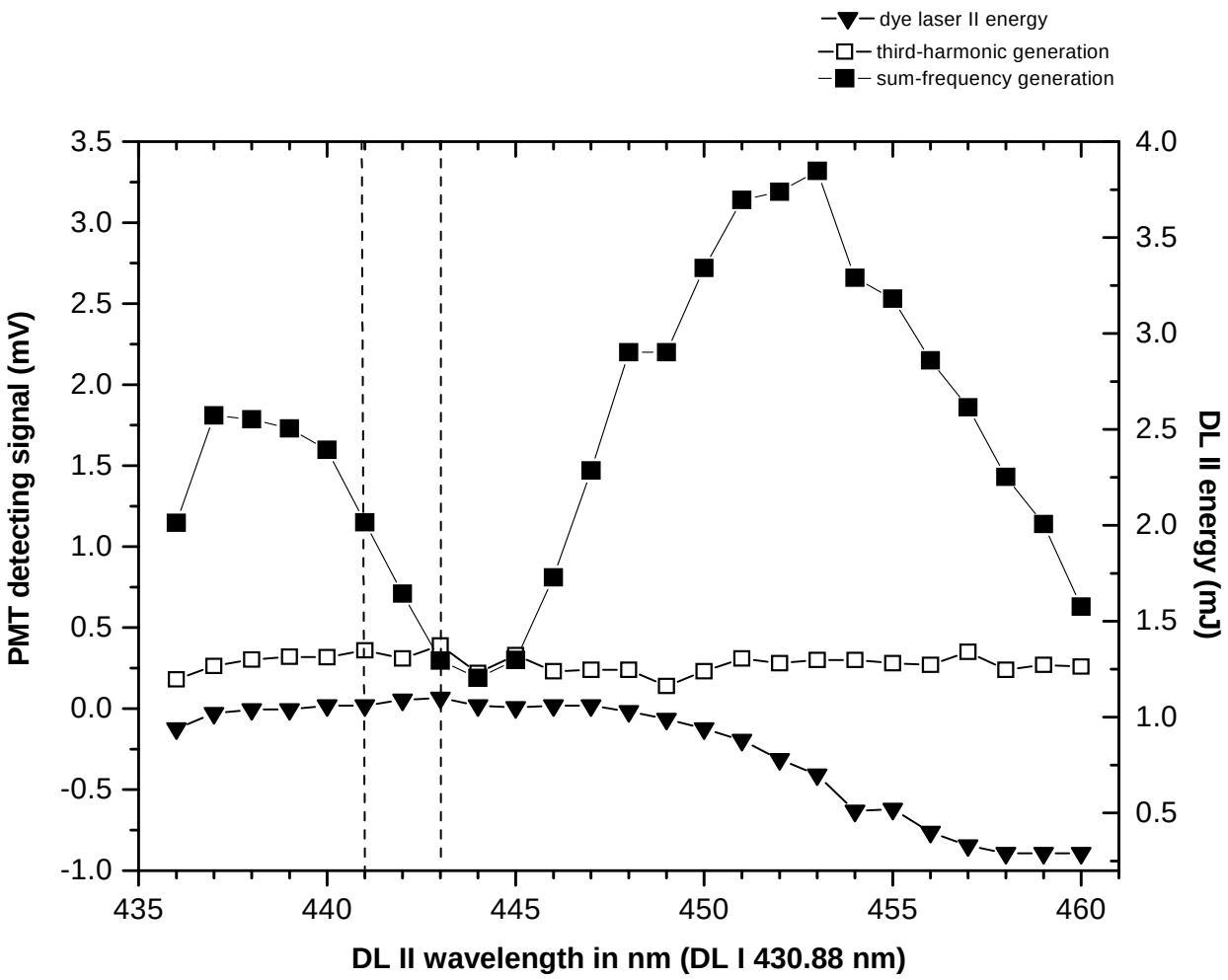

Figure 4-22: The graph shows the sum-frequency signal, the third-harmonic signal and the energy of the dye laser II as a function of dye laser II wavelength. The energy of dye laser II is also shown.

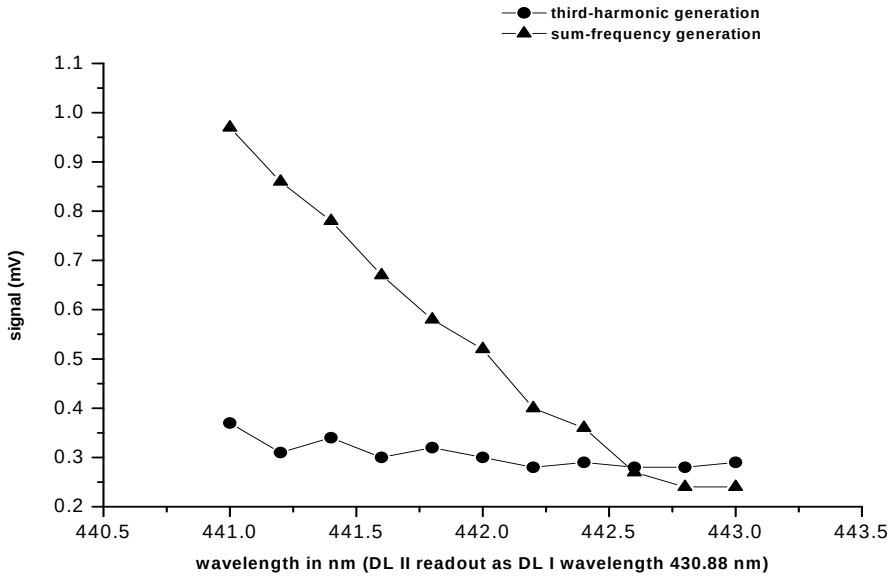

Figure 4-23: Graph shows VUV output in dye laser II wavelength region $441 - 443$ nm.

since it is a wavelength region that is of interest for LIF spectroscopy of CO. In figure 4-22 the third-harmonic generated is constant, as can be expected, but the sum-frequency generation shows a "dip" at 443 nm. This is due to an absorption line in Mg, and explains the anomalous results previously mentioned in section 4.2.3. In the wavelength region 452 nm to 460 nm the dye laser II energy decreases and as a result the VUV output decreases.

The same experiment was repeated in wavelength region 441 nm to 443 nm (the region of interest for LIF spectroscopy) by tuning dye laser II wavelength in 0.2 nm steps. The experimental result is shown in figure 4-23 and indicates that for dye laser II wavelength around 442.6 nm, sum-frequency generation is even weaker than third-harmonic generation.

4.2.7 Polarization and collinear alignment of laser beams

As mentioned in section 2.1.5 for optimal VUV output at any desired wavelength, two incident dye laser beams must be perfectly left- and right-circularly polarized respectively. In the present VUV setup, this is achieved by changing dye laser I polarization by 90° from vertical polarization to horizontal polarization using a double Fresnel prism. Dye laser I polarization was tested

by inserting a prism polarizer in the dye laser I beam. This polarizer transmits only one polarization direction (vertical) ensuring that the two incident dye laser beams have the required perpendicular plane polarization before their polarization was changed to right- and left-hand circular polarization in a single Fresnel rhombus. This experiment was done for three dye laser II wavelengths: 441 nm, 442 nm, and 443 nm with dye laser I wavelength set at 430.88 nm as usual. For every dye laser II wavelength, two spectra were measured: one spectrum obtained by inserting a prism polarizer in the dye laser I beam and the other without any additional polarizer in the beam. The experimental results are shown in figures 4-24, 4-25 and 4-26 below. From these results it is clear that the additional polarizer did not reduce the third-harmonic generated, and it is therefore concluded that the polarizer did not improve the laser polarization significantly.

To summarize:

VUV tunable laser generated by two-photon resonance four-wave mixing in two-component gaseous medium has been characterized by experiment. Using the monochromator to distinguish between the third-harmonic and sum frequency generation, it was possible to optimize phase-matching. The experiment illustrated that phase-matching for sum-frequency generation can be achieved by changing external krypton pressure.

In the experiment it is found that the resonant dye laser (dye laser I) energy affects the VUV output more than dye laser II energy, as could be expected from the theory. Tunable sum-frequency generation was achieved by scanning the dye laser II wavelength over the range of the dye used in the dye laser II.

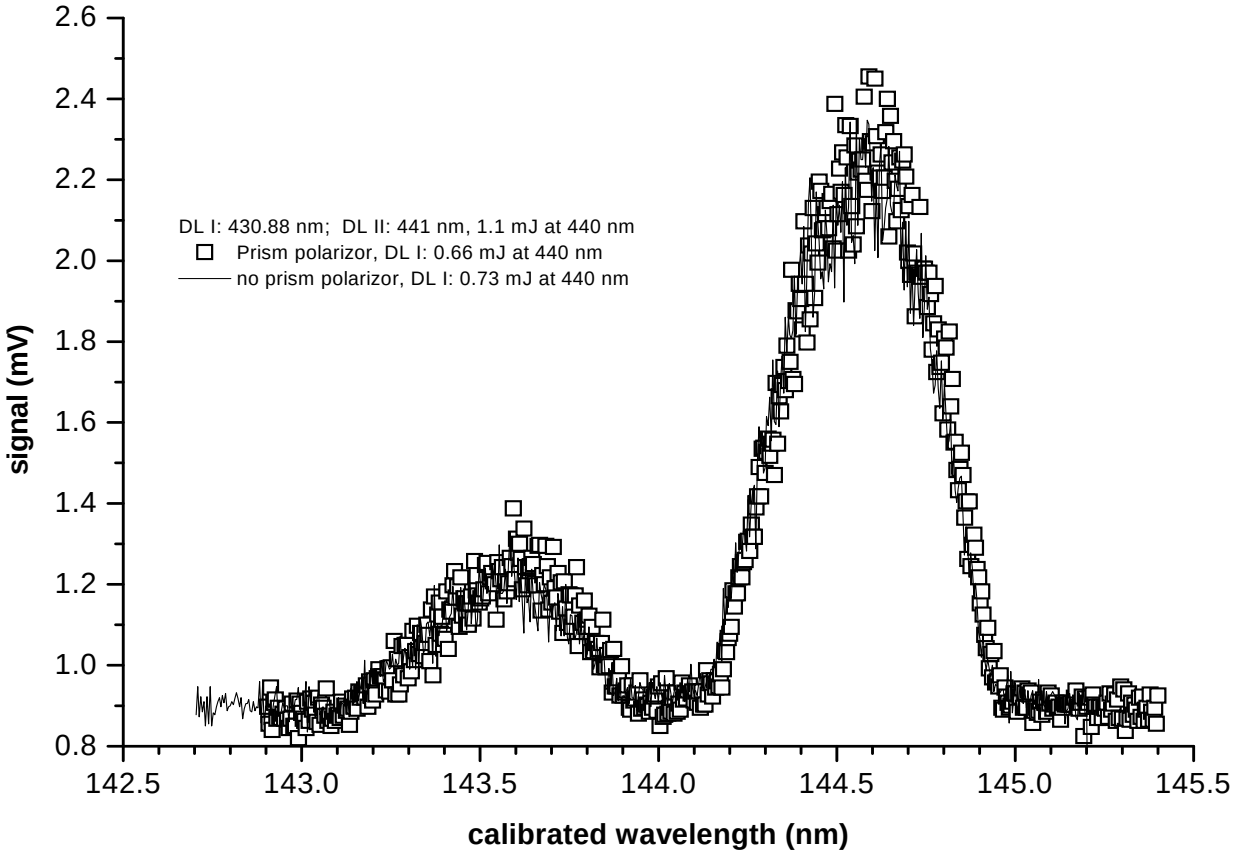

Figure 4-24: VUV spectrum obtained with and without prism polarizer in dye laser I beam, and dye laser II wavelength set at 441 nm.

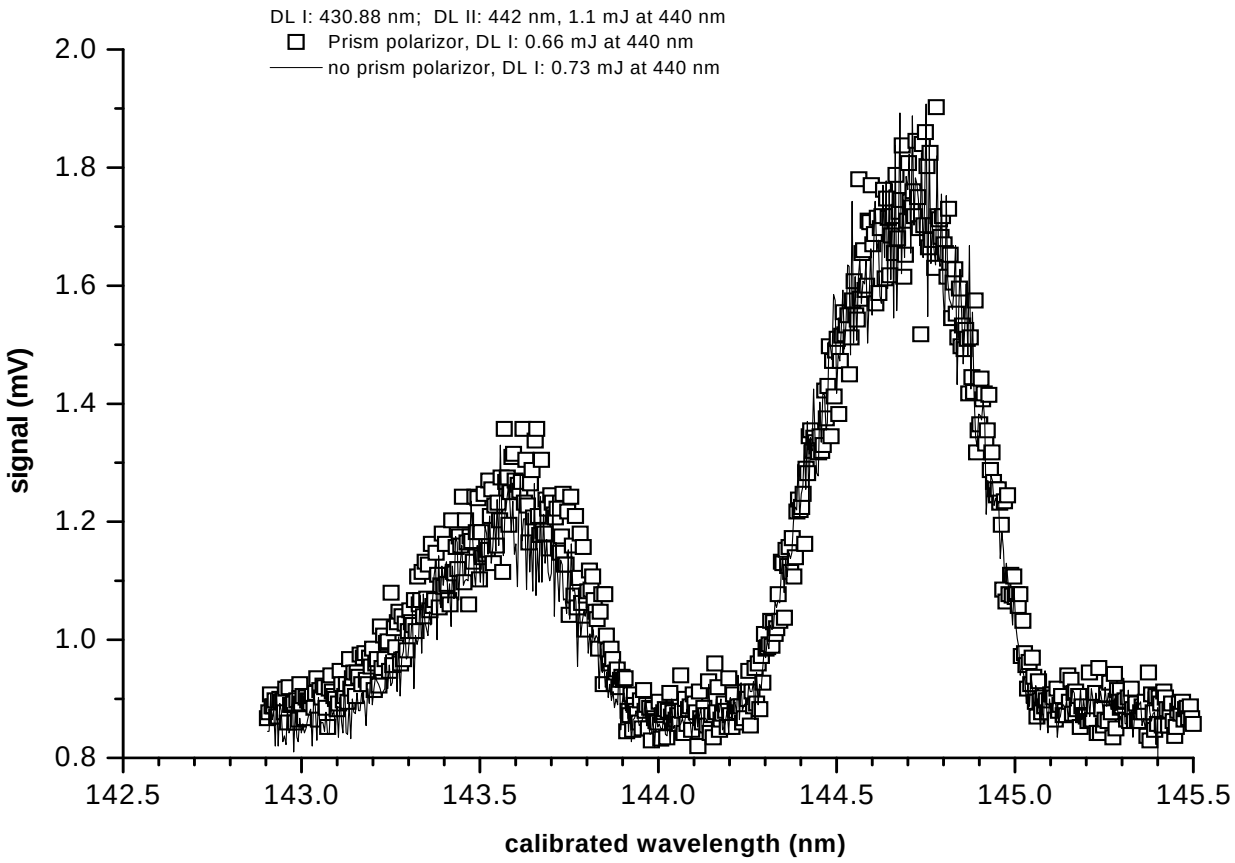

Figure 4-25: VUV spectrum obtained with and without prism polarizer in dye laser I beam, and dye laser II wavelength set at 442 nm.

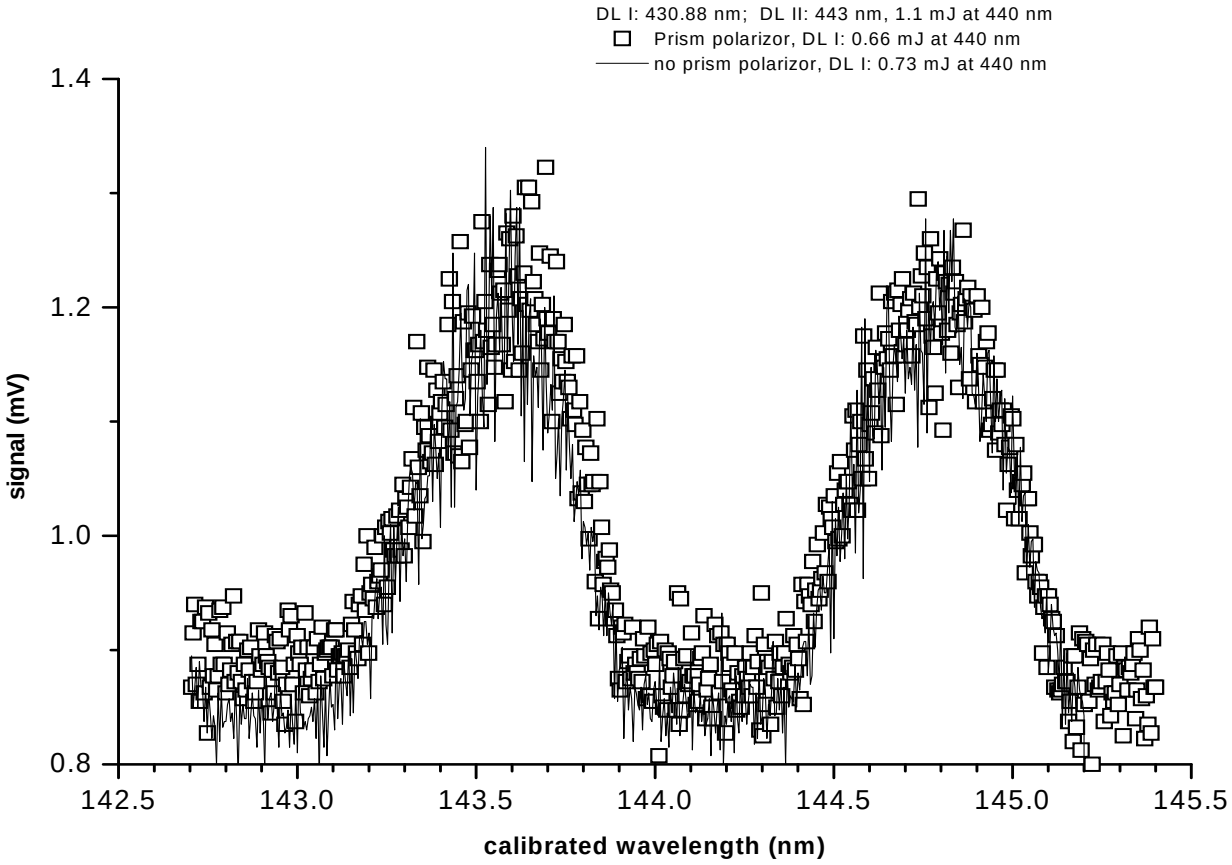

Figure 4-26: VUV spectrum obtained with and without prism polarizer in dye laser I beam, and dye laser II wavelength set at 443 nm.

Chapter 5

High resolution spectroscopy of CO

The tunable VUV laser source was used to acquire high resolution fluorescence spectra of the CO molecule in the VUV region. The potential energy curves of most of the known electronic states of $^{12}C^{16}O$ molecule are illustrated in figure 5-1, with the $A^1\Pi\,(3) - X^1\Sigma^+\,(0)$ transition investigated in our experiment indicated by an arrow. In figure 5-1 the arrow is used to show that the electronic-vibration transition is vertical. Hence the transition probability between two bands is determined by the Frank-Condon principle (refer to figure 2-9 (see section 2.2.1)). In this work four rotational transitions $R(0)$, $R(1)$, $R(2)$ and $R(3)$ of this transition ($A^1\Pi\,(3)$ $- X^1\Sigma^+\,(0)$) were investigated in the region 144.74 nm to 144.72 nm.

5.1 CO fluorescence excitation spectrum

Fluorescence excitation spectra of the $^{12}C^{16}O$ molecule were recorded. During the experiment, dye laser II wavelength was tuned from 440.88 nm to 440.99 nm, which converts to VUV wavelength region 144.721 nm to 144.733 nm. A scanning wavelength step size of 2×10^{-12} m, was chosen. A CO gas mixture of 10% CO in Ar at a pressure of 4 bar was introduced into the excitation chamber through the pulsed valve, which was synchronized with the laser excitation pulses. Vacuum pressure in the chamber was 4×10^{-6} mbar. The excitation fluorescence was monitored by PMT 2 at right angle to the VUV beam.

A typical LIF spectrum of CO molecule recorded by PMT 2 is shown in figure 5-2. In the supersonic jet expansion the CO molecule was cooled to very low temperature (only a

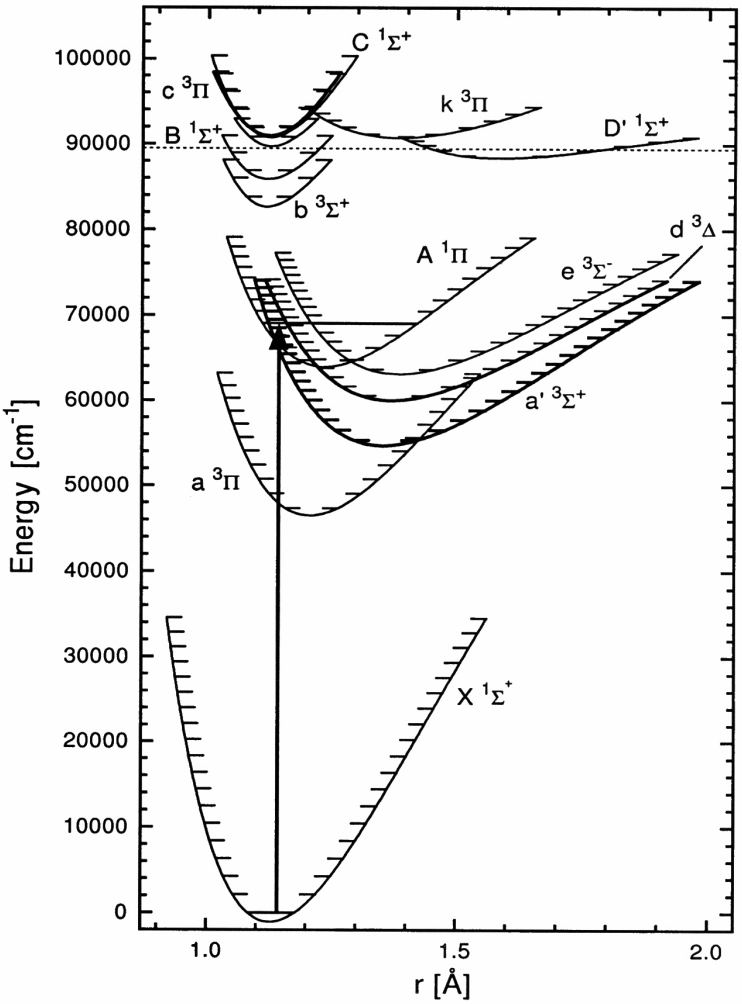

Figure 5-1: CO potential energy curves of the electronic states of $^{12}C^{16}O$ up to the dissociation limit calculated by the RKR procedure [13]. X-axis plots the internuclear C-O distance. The dotted horizontal line indicates the dissociation energy of CO. The electronic vibrational transiton investigated in our experiment is indicated by a vertical arrow.

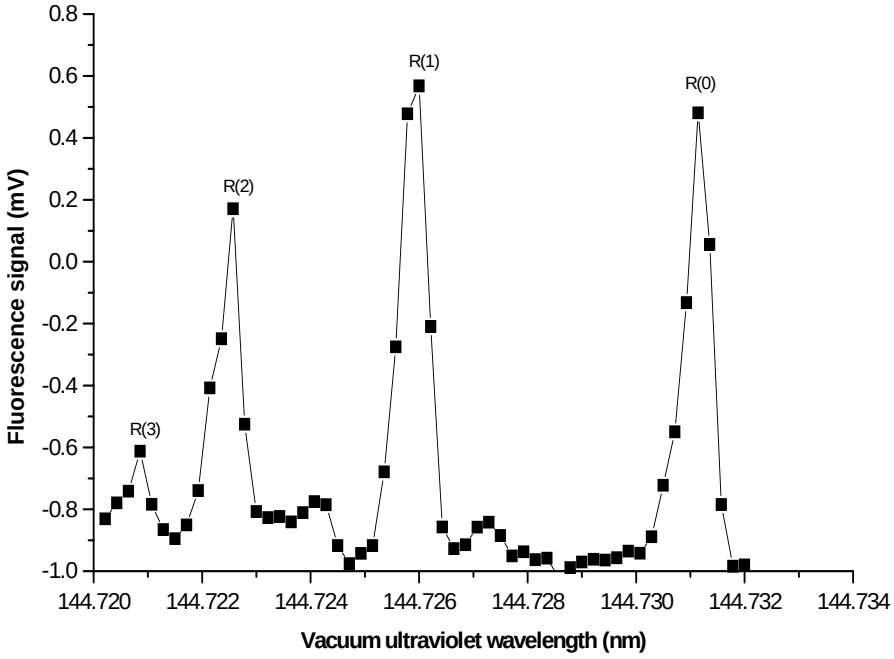

Figure 5-2: A typical LIF spectrum for the $A^1\Pi\,(3) - X^1\Sigma^+\,(0)$ transition of super cooled $^{12}C^{16}O$.

few Kelvin), and therefore most molecules were excited from the lowest rotational levels, as is evident from the fact that only the rotational peaks $R(0)$, $R(1)$, $R(2)$ and $R(3)$ were found. Higher states had significantly lower occupation.

Most CO molecules stay at the lowest rotational level because of low rotational temperature in supersonic jet, and rotational temperature in supersonic jet could be calculated considering the relative intensities of the rotational transitions according to the Boltzmann distribution.

In order to determine the rotational constants of both upper and lower states, measuring the separation $\Delta\upsilon\,(J)$ of these successive rotational lines can be used. According to equation 2.87, the relation used to determine the constants is given by:

$$\Delta\upsilon\left(J'\right) = 2B'_v + 2\left(B'_v - B''_v\right)J' \tag{5.1}$$

Using this relation, the rotational constants for this CO transition shown in figure 5-2 were

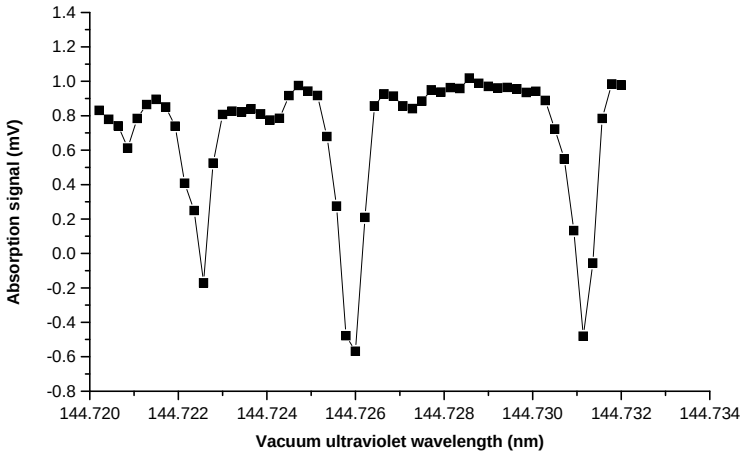

Figure 5-3: A typical absorption spectrum for the $A^1\Pi\,(3) - X^1\Sigma^+\,(0)$ transition of super cooled $^{12}C^{16}O$.

calculated: $B'_v = 1.6$ and $B''_v = 2.0$, which are comparable to the values $B'_v = 1.6116$ and $B''_v = 1.9313$ from the literature [1], confirming that the transitions were correctly identified. (The theoretical spectrum of CO molecule of the $^1\Pi - ^1\Sigma^+$ transition was discussed in section 2.2.3)

5.2 Absorption spectrum

The use of the monochromator enabled us to record absorption spectra. The monochromator was connected to the excitation chamber as illustrated in figure 3-10. The monochromator grating was set to select the excitation wavelength of the rotational peak $R(0)$ discussed in the previous paragraph, both slit widths were opened wide, so as to utilize the monochromator as a filter to separate the tunable VUV from the third-harmonic. This made it possible for the first time to record the excitation fluorescence spectrum (monitored by PMT 2) while simultaneously recording an absorption spectrum through the monochromator.

A CO absorption spectrum recorded in this way is shown in figure 5-3. All peaks in the spectrum results from the VUV laser beam being absorbed by CO molecules, and clearly this spectrum has the same features as the excitation fluorescence spectrum. The relatively low

signal to noise ratio in the recorded absorption spectra was a rather surprising result. Usually only fluorescence excitation spectra are recorded. It is unusual to record absorption spectra in pulsed laser spectroscopy (with continuous wave lasers absorption spectroscopy is often done, but not with pulsed lasers) since the signal to noise ratio is usually poor. However in the supersonic jet, CO molecule temperature is very low, most of the CO molecules are in the lowest vibrational and rotational level of the electronic ground state, only extremely few are in higher vibrational levels. As a result, all the absorption process practically only happened from the lowest vibrational level and lower rotational levels to the different vibrational levels and rotational levels of the upper electronic state. The signal to noise ratio is less than for the fluorescence, but is good enough to possibly give additional information to the simultaneously recorded fluorescence spectrum, as will be discussed in the next section.

5.3 Comparison of fluorescence and absorption spectrum

The simultaneous recording of LIF and absorption spectra of the $^{12}C^{16}O$ molecule can give additional information about the molecule. For instance it would make it possible to detect excitation transitions which do not fluoresce.

Figure 5-4 shows both absorption and LIF spectra. Every fluorescence peak is matched with an absorption peak well, which illustrates that in this case, all excited states recorded in this region of the spectrum fluoresced.

5.4 CO fluorescence spectrum

An attempt was made to record a fluorescence spectrum by using the monochromator to disperse and analyse the different spectral components of the CO fluorescence. For this the monochromator was placed as shown in figure 3-11. The same experimental conditions were used as before with the dye laser I wavelength tuned to 430.88 nm; the dye laser II wavelength was tuned to the region around 440.979 nm giving VUV output about 144.73 nm to excite $^{12}C^{16}O$ molecule from lower electronic-vibration state $X^1\Sigma^+(0)$ to higher electronic-vibration state $A^1\Pi(3)$ and in particular the relevant $R(0)$ transition . The gas mixture of CO and Ar contained 10% CO gas and had a pressure of 4 bar. Vacuum pressure in the chamber was between 4×10^{-6} mbar.

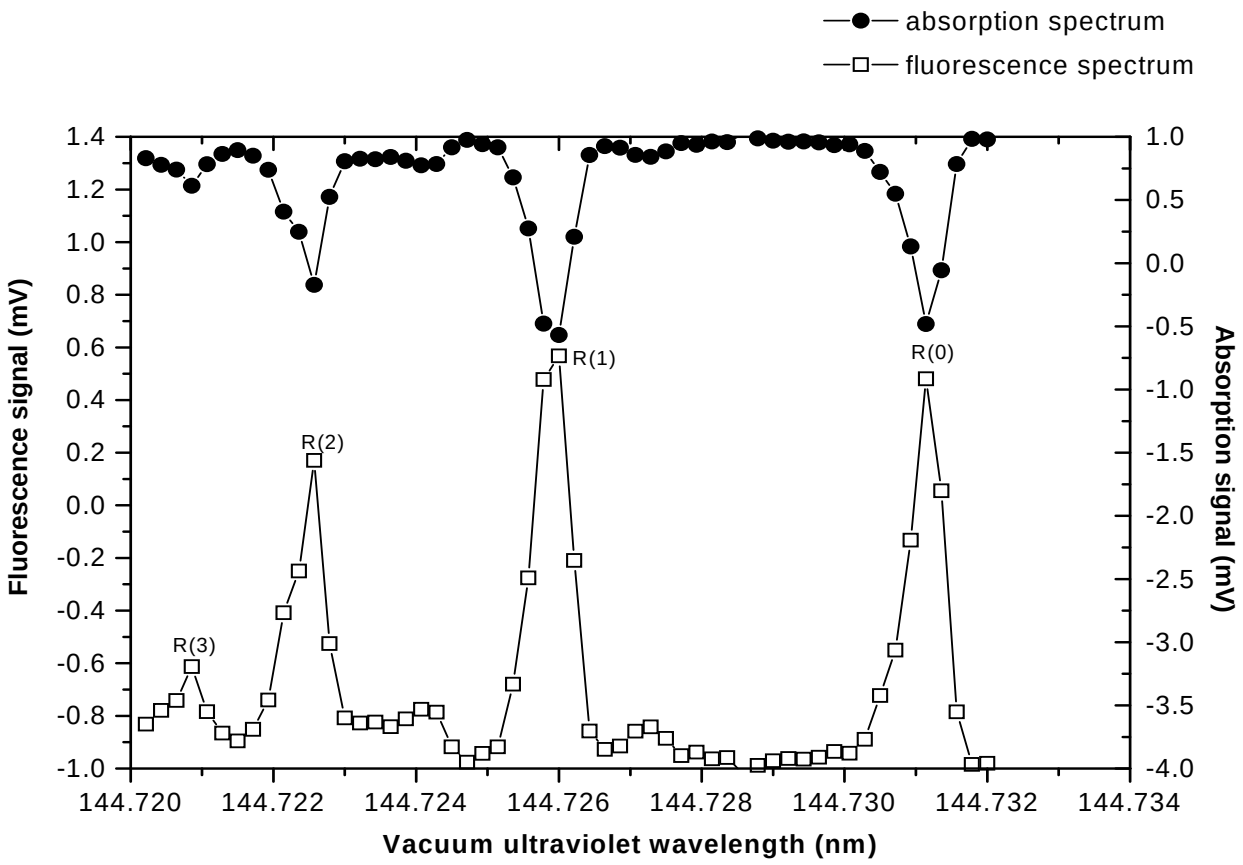

Figure 5-4: A typical LIF and absorption sepctrum for the $A^1\Pi\,(3) - X^1\Sigma^+\,(0)$ transition of super cooled $^{12}C^{16}O$.

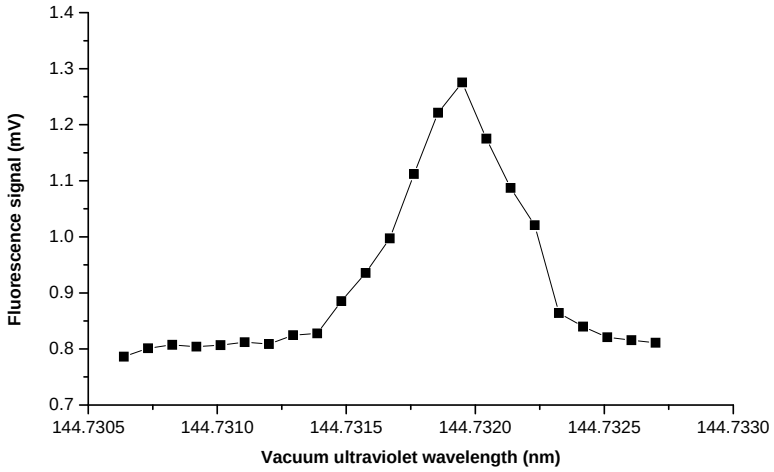

Figure 5-5: The transition $(A^1\Pi\,(3) - X^1\Sigma^+\,(0)\,)\;R\,(0)$ recorded by PMT without monochromator.

By tuning the dye laser, firstly, one of CO fluorescence peaks ($R\,(0)$ shown in figure 5-5) was directly recorded by PMT without monochromator in place to ensure that the transition was indeed excited. It is clear that the signal obtained in the spectrum has relatively high intensity, which raised the hope of the possibility to record the dispersed fluorescence spectrum of CO molecule using monochromator.

However it was not possible to record a fluorescence spectrum using the monochromator. The signal strength was simply to low to detect. This can be ascribed to the drastically reduced acceptance angle. However, for future work on molecules with stronger fluorescence signals, this new addition to the infrastructure could be valuable.

Chapter 6

Conclusions and outlook

A tunable VUV laser beam produced by four-wave frequency mixing generated in a two-component gaseous medium has been characterized in the presented work. Two dye laser beams pumped by an excimer laser interact with magnesium vapor in a crossed concentric heat-pipe oven to produce VUV radiation. Magnesium was chosen for its high non-linear susceptibility, whereas krypton gas was chosen to do phase-matching. In this work the efficiency of an existing the tunable vacuum ultra-violet (VUV) laser source was improved. This was achieved by the introduction of a monochromator to separate the tunable VUV generated by four-wave mixing from the competing third-harmonic generated. This, for the first time, made it possible to properly optimize the yield of tunable VUV. This was achieved by selecting the correct dye laser energies, and the correct phase-matching. Further optimization of sum-frequency generation and suppression of competing third-harmonic generation, could be achieved by ensuring optimal polarization of the laser beams (right- and left-hand circularly polarized) before they entered the heat-pipe oven. Previously this optimization could not be achieved in this fashion, since the third-harmonic and sum-frequency wavelengths could not be separated without the monochromator installed. The design and construction of a vacuum system required for the monochromator to be able to operate in this wavelength region was successful and the first benefit of this new facility was that it enabled us to characterize the VUV laser output generated by a four-wave frequency mixing process in a magnesium vapor heat-pipe properly, clearly improving the quality of the output of the source used for excitation spectroscopy.

The VUV source and LIF detection system was initially used in experiments concentrating

on state selective VUV excitation of molecules using total fluorescence detection. The introduction of a VUV monochromator to record the transmitted VUV after excitation of the CO in a supersonic jet enabled us to record an absorption spectrum of the molecules. The spectrum had a very good signal to noise ratio, which was an unexpected result. The fact that the absorption spectrum can be recorded simultaneously with the total fluorescence measurement, provided a very powerful new tool available to the VUV setup in the laboratory of the Laser Research Institute.

An experimental setup to detect the fluorescence spectrum was also constructed and implemented. The VUV monochromator was set up to record the fluorescence spectrum. The monochromator was calibrated and set up using continuous VUV sources, such as a novel corona nitrogen discharge, and it was shown to be functional. However, the fluorescence from the CO excited by the VUV laser source was too weak to be detected through the monochromator. The setup is however functional and should prove very useful in experiments where the fluorescence is of higher intensity.

6.1 Future work

The facility to simultaneously detect an absorption spectrum and an LIF spectrum may prove invaluable in the search for electronic excitations of CO-Ar or CO-CO van der Waals molecules, since these theoretically predicted states may be pre-dissociating. At present search for possible transitions of such van der Waals molecules were concentrating only on LIF detection. The added facility, allowing us to record an absorption spectrum simultaneously with the LIF spectrum, may enable us to detect excitation to these non-fluorescent states.

The facility has also been expanded to make it possible to record wavelength dependent fluorescence. This will be a valuable tool for future experiments where the fluoresces may be stronger than in the case of the CO transitions investigated in this work.

Bibliography

[1] G. Herzberg: "*Molecular spectra and molecular structure I. Spectra of diatomic molecules*", National Research Council of Canada, second edition.

[2] J.F. Ward, G.H.C. New: "*Optical third-harmonic generation in gases by a focused laser beam"*, Phys. Rev. **185**, 57 (1969)

[3] W.R. Brode: "*Chemical spectroscopy"*, John Wiley &Sons, Inc., New York, (1958)

[4] C.M. Steinmann: "*Development and characterization of a tunable laser source in the vacuum ultra-violet",* M.Sc (cum laude) University of Stellenbosch (1999)

[5] R.W.B. Pearse, and A.G. Gaydon: "*The identification of molecular spectra"*, John Wiley & Sons. Inc., New York (1976)

[6] Y. Tanaka, T. Namioka, and A. S. Jursa: "*New emission bands of* N_2^+, $^2\Pi_g - A^2\Pi_u$", Can. J. Phys. Vol. 39, 1138-1145 (1961)

[7] T. Namioka, K. Yoshino, and Y. Tanaka: "*Isotope bands and the vibration assignment of the* $D^2\Pi_g - A^2\Pi_u$ *system of* N_2^+", J. Chem. Phys. Vol 39, number 10, 2629-2633 (1965)

[8] S.E. Harris, R.B. Miles: "*Proposed third-harmonic generation in phase-matched metal vapors*", Appl. Phys. Lett.**19**, p 385, (1971)

[9] J.F. Young, G.C. Bjorklund, A.H. Kung, R.B. Miles, S.E. Harris: "*Third-harmonic generation in phase-matched Rb vapor*", Phys. Rev. Lett. **27**, 1551 (1971)

[10] S.E. Harris, R.B. Miles: "*Optical third-harmonic generation in alkali metal vapors*", IEEE J. QE-9, 470 (1973)

[11] B. Steffes and C.M. Steinmann: "*Manual for construction and use of the crossed concentric heat-pipe oven system",* document available in the laser laboratory of the Physics Department, University of Stellenbosch (1999)

[12] D. M. Bloom, J. T. Yardley, J. F. Young, S.E.Harris: "*Infrared up-conversion with resonantly two-photon pumped metal vapors*", Appl. Phys. Lett. **24**, 427 (1974)

[13] A. Mellinger: "*Untersuchung hochangerregter Triplettzustände des CO-Moleküls*", Ph.D. dissertation, Technische Universität München and Max Planck Institut für extraterrestrische Physik, Garching, Germany (1995)

[14] A. Ulrich, P. Privitera, R. Krücken, A. Morozov, T. Ottenthal, V. Verzi, J. Wieser: "*Air fluorescence in the laboratory using low energy electron beam excitation*"

[15] K. M. Leung, J. F. Ward, B. J. Orr: "*Two-photon resonant, optical third-harmonic generation in cesium vapor*", Phys. Rev. **A9**, 2440 (1974)

[16] E. U. Condon: "*Nuclear motions associated with electron transition in diatomic molecules",* Phys. Rev. **32**, 858 (1928)

[17] C. R. Vidal: "*Four-wave frequency mixing in gases*", In L. F. Molenauer and J. C. White (Eds.), *Topics in Applied Physics* **59** - "Tunable lasers", pp. 57-113, Springer Verlag, Heidelberg (1987).

[18] P. Klopotek and C. R. Vidal: "*Frequency selective excitation spectroscopy of the CO intercombination bands*", Can. J. Phys. **62**, 1426 (1984)

[19] P. Klopotek and C. R. Vidal: "*Two-step vacuum-ultraviolet visible excitation spectroscopy on the CO molecule*", Journal of the Optical Society of America B **2**, 869-876 (1985)

[20] A. Mellinger and C. R. Vidal: "*Laser-reduced fluorescence spectroscopy on predissociated CO triplet states*", Journal of Chemical Physics **101**, 104-110 (1994)

[21] A. Lofthus and P. H. Krupenie :"*The spectrum of molecular nitrogen*", Journal of Physical and Chemical Reference Data, Vol 6, Issue 1, pp 113-307, Jan. 1977

[22] R.T. Hodgson, P.P. Sorokin, J.J. Wynne: "*Tunable coherent vacuum-ultraviolet generation in atomic vapors*", Phys. Rev. Lett. **32**, 343 (1974)

[23] R. W. Nicholls, "*Franck-Condon factors and r-Centroids to high quantum numbers for the* $^2\Pi_g - ^2\Pi_u$ *system of* N_2^+", Can. J. Phys. **40**, 523 (1962)

[24] H. Puell and C.R. Vidal: "*Non-linear polarizations and excitations and their time dependence in discrete multilevel systems*", Phys. Rev. **A. 14**, 2225 (1976)

[25] D.C. Hanna, M.A. Yuratich, D. Cotter: "*Non-linear optics of free atoms and molecules*", Springer Ser. Opt. Sci. Vol. 17 (Springer, Berlin, Heidelberg 1979)

[26] C.R. Vidal: "*Laser spectroscopy of atoms and molecules 1*", Max-Plank-Institutür Extraterrestrische Physik. Garching, Germany (1998)

[27] C.R. Vidal: "*Coherent VUV sources for high resolution spectroscopy*", Appl. Opt. **19**, No. 23, p. 3897 (1980)

[28] H. Puell, K. Spanner, W. Falkenstein, W. Kaiser, C.R. Vidal: "*Third-harmonic generation of mode-locked Nd: glass laser pulses in phase-matched Rb-Xe mixtures*", Phys. Rev. **A 14**, 2240 (1976)

[29] P.P. Bey, J.F. Giuliani, and H. Rabin: "*Generation of a phase-matched optical third-harmonic by introduction of anomalous dispersion into a liquid medium*", Phys. Rev. Lett, 19, 819 (1967)

[30] P.P. Bey, H. Rabin: "*Coupled-wave solution of harmonic generation in an optically active medium*", Phys. Rev. **162**, 794 (1967)

[31] A.R. Edmonds: "*Angular momentum in Quantum Mechanics",* Princeton University Press, Princeton (1960)

[32] C.R. Vidal: "*Vapor cells and heat-pipes*", Experimental methods in the physical sciences **29 B**, p 67 (1996)

[33] L.F. Mollenauer and J.C. White: "*Topics in Applied Physics*", Vol. 59: Tunable lasers (1987)

[34] J.D. Jackson: "*Classical Electrodynamics",* Wiley, New York (1967)

[35] G.C. Bjorklund: "*Effects of focusing on third-order non-linear process in isotropic media*", IEEE J. QE-11, 287 (1975)

[36] J.A. Armstrong, N. Bloembergen, J. Ducuing, and P.S. Pershan: "*Interaction between light waves in a non-linear dielectric*", Phys. Rev. **127**, 1918 (1962)

[37] L. Bridwell, W.E. Maddox, L.M. Beyer, and R.C. Etherton: "*A computer controlled step-scanning vacuum ultra-violet spectrometer for beam foil spectroscopy*", Appl. Opt. 9, No 4, p 929 (1970)